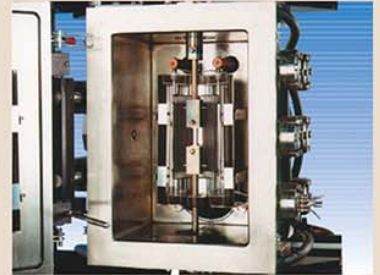




The Scientific Bulletin of Valahia University MATERIALS and MECHANICS



2017

Vol. 15 No. 12

THE INFLUENCE OF COOLING RATE ON STRUCTURE OF EN AC 5083 ALUMINUM ALLOY

Mirela POPESCU, Bela VARGA

Transilvania University of Brasov, Material Science Department, 29 Eroilor Blvd., 500036, Brasov, Romania

E-mail: mireladragoiu1@yahoo.com

Abstract: In this paper it was studied the structure of EN AC 5083 aluminum alloy depending on cooling conditions. By cooling curves recorded for different casting conditions there were calculated the cooling rate (v_r). The structural analyzes, performed by Image Pro-Plus 6.0 software, allowed both be highlighted structural particularities of various conditions for casting and establishing the correlation: $\lg d = \lg v + n$ (where d is the dendritic parameter).

Keywords: aluminum alloy, cooling rate, melt spinning, directed solidification

1. INTRODUCTION

The EN AC 5083, Table 1, is part of Al-Mg classes alloys. This is characterized by good mechanical properties and it is a hard alloy with excellent weldability and good corrosion resistance including the marine environment.

The great variety of platbands, sheets, foils, round bars, rectangular bars, different profiles, wires and pipes produced from this composition has, as a cake ingot, the round or /and rectangular ones made by semi-continuous (continuous) casting.

As it is known by structure finishing it is ensured both the improvement of exploitation properties and the reducing of metallic and nonmetallic impurities influence by their distribution on a much larger inter granular area, allowing the old metal waste recovery in processing of deformable alloys. Basically these considerations are the basis of interest in technologies that ensure to obtain a fine structures both after casting (solidification) and after alloy processing by severe plastic deformation [1-10] or by pulverization + press technology [11]. Meanwhile, quantitative structural analysis provides data and the stability of processing technologies (hardware, plastic deformation, etc.).

This paper analyzes the influence of cooling rate on structure of EN AC 5083 alloy casted-solidified at different cooling rate.

2. EXPERIMENTAL DETERMINATIONS

The alloy elaboration was performed in an electric furnace with electric resistance and a graphite crucible. Protection of the melt against oxidation was carried out by using a flow coating. This has been a temperature of 730°C.

The casting of alloy was done in forms made on different materials in order to modify cooling rate. In each form it was placed a thermocouple to register each variation of temperature versus time, Figure 1 a, b, c. In parallel was casted a directed solidified sample, fig. 1d. For the registration of cooling curve was used an ADAM type interface and K type thermocouple.

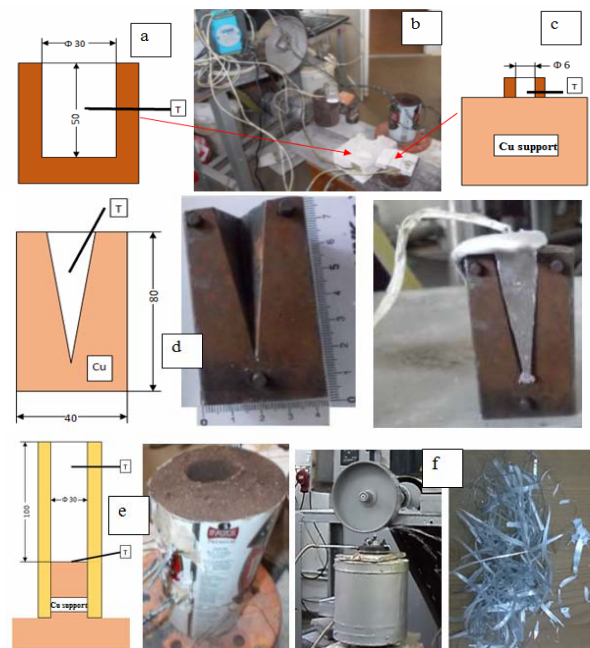


Figure 1. Forms used in casting of solidified specimens with different cooling rates:

a) the form of refractory brick; b) general view of the assembly; c) drop specimen, with copper support and refractory brick mould; d) wedge-pyramid sample mould casted; e) the mould form for directed solidification, with a copper support and a form in a foundry sand; f) melt spinning plant and the obtained tape; T-thermocouple position

Table 1. Chemical composition of EN AC 5083 alloy

Element	Si	Fe	Cu	Mn	Mg
[%]	0.4	0.4	0.15	0.4-1.0	4-4.9
	Cr	Zn	Ti	Other	Al
	0.05-0.25	0.25	0.15	0.05	Balance

In order to enlarge the observation area of cooling rate influence on structure were cast bands by melt-spinning method. Figure 1.f shows the laboratory installation used for this purpose and the tape obtained. The length of fragments reached 200-300 mm strips, widths is 1-5 mm and thick of 30-70 microns, with very good ductility. Based on previous determinations [12] it has admitted that the cooling rate in this case was $5.10^{50}C/s$.

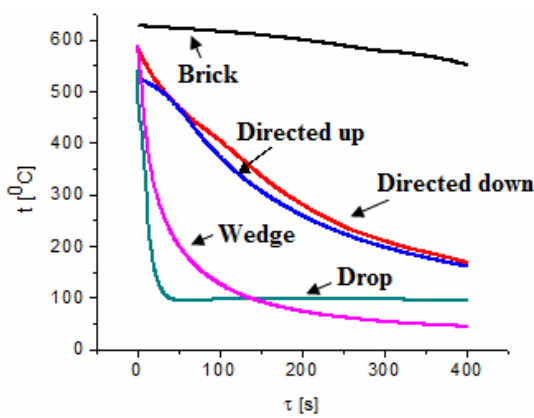


Figure 2. Recorded cooling curves

To determine the cooling rate it was resorted to derive the cooling curves (Figure 2). In Figure 3 are presented the variation curves of the cooling rates recorded for "Wedge" and "Directing-down" samples.

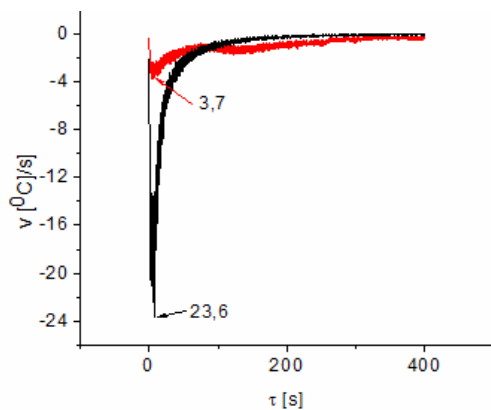


Figure 3 Cooling rates determined by cooling curves derivation

In Figure 4 there are represented the obtained significant structures for solidified samples at different cooling rates.

It is observed that the down side of wedge sample (pin) structure is composed of very different sizes dendrites.

The sizes of rough dendrites are about 35-50 microns and the fine ones are of 3-5 microns. This structure can be explained by starting of crystallization process in the ladle, with low cooling rate, and the finalization of solidification process in copper support, with high cooling rate. This observation is in agreement with maximum temperature values on cooling curve.

Through direct measurements and quantitative analysis of recorded structures, Figure 5, by Image Pro-plus 6.0 software [13-14], it was obtained the maximum, minimum and average of dendritic parameter values (d) Table 2.

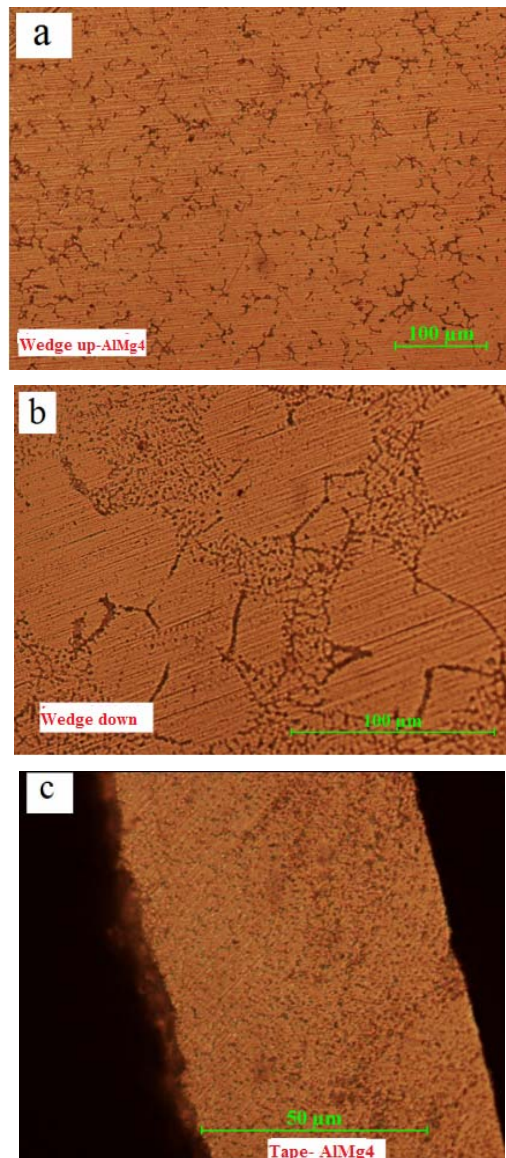


Figure 4. Microstructure of solidified samples with different cooling rates:
 a) wedge-up sample; b) wedge-down sample (pin) and c) tape cast by melt spinning method

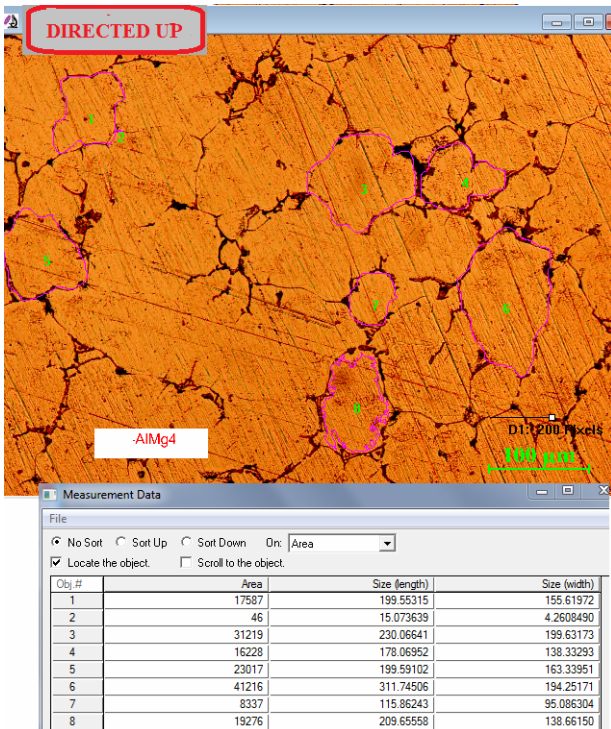


Figure 5. Quantitative analysis of structure using Image Pro-Plus 6.0 software

In Table 2 there are listed the corresponding values of maximum cooling rates recorded during the solidification.

Table 2. Data to determine the interdependence $lg d = lg v + n$

Sample	Brick	Directed solidification		Drop	Wedge-pyramid			Melt spinning
		Down	Up		Up	Down (pin)		
Parameter					Rough structure	Fine structure		
v [°C/s]	0.37	3.7	2.5	48	23.6	-	500000	
lg(v)	-0.432	0.568	0.398	1.681	1.373	-	5.69897	
d _{min} [µm]	205	42	100	65	12.9	43	2.7	
d _{max} [µm]	230	52	115	72	14.5	52	4.4	
d [µm]	217	47	107	68	12.7	48	3.5	
lg (d)	2.336	1.672	2.03	1.832	1.954	1.104	0.431364	

By constructing the diagram lg (d) depending on lg (v) Figure 6 and by mathematical processing of experimental data the equation resulted is (1):

$$lg d = -0,28.lg v + 2,02 \quad (1)$$

which describes dendritic parameter variation depending on local cooling rate for the studied alloy(EN AC 5083).

In parallel, in the previous figure it was also represented this interdependence for AlSi7Mg0.3 alloy:

$$lg d = -0,4.lg v + 2,37 \quad [9] \quad (2)$$

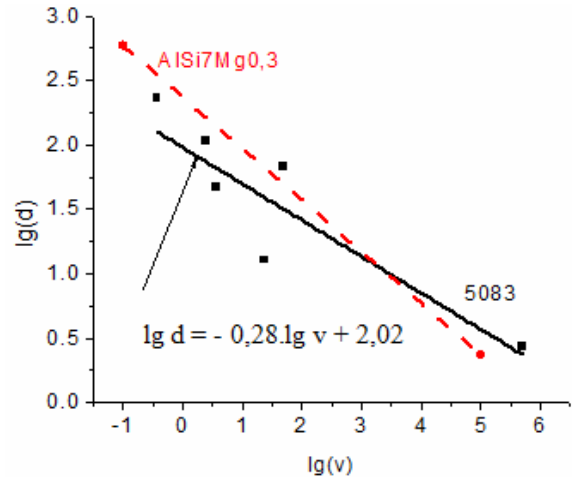


Figure 6. Representation for determining interdependence: $lg d = lg v + n$

It is worth mentioning that for aluminum-based alloys the coefficient value of ‘lgv’ term, this means that the inclination (declivity) of line varies in the range of from 0.25 to 0.39 [12].

3. CONCLUSIONS

By compliance with casting temperature it is ensured the structure homogeneity.

Related to interdependence determining “ $lg d = -0,28.lg v + 2,02$ ” for EN AC 5083 alloy can make the following findings:

- EN AC 5083 alloy, in structural terms, is less sensitive to changing cooling rate than other aluminum base alloys.
- The cooling rates offered by conventional technology conditions for processing provide structure finishing at a rate of 94%.
- Through the melt spinning technology the structure finishing is about 98%.

4. ACKNOWLEDGMENTS

We hereby acknowledge the structural funds project, (SOP HRD), ID137516 financed from the European Social Fund and by the Romanian Governmentand the structural funds project POSDRU/159/1.5/S/137516 for providing the infrastructure used in this work.

REFERENCES

Journals:

- [1] Tellkamp V.L., Lavernia E.J., Processing and mechanical properties of nanocrystalline 5083 Al alloy. Nanostructured Materials, Vol. 12, 1999, pp. 249-252

- [2] Liorca-Isern N., Luis-Perez C., Gonzales P. A., Patino D.: Analysis of structure and mechanical properties of AA 5088 aluminium alloy processed by ECAE, Rev. Adv. Sci. 10 (2005), p 473-478
- [3] Youssef K.M., Scattergood, R.O., Murty K.L., Koch C.C.: Nanocrystalline Al–Mg alloy with ultrahigh strength and good ductility, Scripta Materialia 54 (2006) 251–256
- [4] Fan G. J., Choo H., Liaw, Lavernia E. J.: Plastic deformation and fracture of ultrafine-grained Al–Mg alloys with a bimodal grain size distribution Acta Materialia 54 (2006) 1759–1766
- [5] Otarawanna S. , Casting of aluminium alloys, Fundamentals of Aluminium Metallurgy: Production, Processing and Applications, Edited by Roger Lumley in Oxford, U.K., 2012.
- [6] Popescu (Drăgoiu) M, Varga B , *Structures of Aluminum Base Alloys Solidified by Vibrations*- Advanced Material Research, vol 1128, 2015, pp 88-97;
- [7] Mohamed A.M.A, Samuel F.H., Alkahtani S. , Influence of Mg and Solution Heat Treatment on the Occurrence of Incipient Melting in Al-Si-Cu-Mg Cast Alloys. Journal of Materials Science and Engineering A 2012; A543 22-34.
- [8] Deshpande J., Makhlof M., Effect of Mold Vibration on the Performance and Casting Characteristics of Aluminum Alloys, Worcester Polytechnic Institute, US, Research Programs, 2012
- [9] Shivkumar, S., Wang, L., Apelian, D.: Molten Metal Processing of Advanced Cast Aluminium Alloys. In: JOM (1991) No. 2, p. 26.
- [10] Karpe B., Kosec B., Bizjak M. *Analyses of the melt cooling rate in the melt-spinning process*, Journal of Achievement in Materials and Manufacturing Engineering, Volum 51, 2012
- [11] Tokarski T., Wedrychowicz M.: High Strength 5083 Aluminium Alloy via Rapid Solidification and Plastic Consolidation Route, Metal, Jun 3rd - 5th 2015, Brno, Czech Republic
- [12] Varga, B., Lichioiu, I.: Method and Installation for Obtaining Metastable Structures of Aluminum Alloys Bulletin of the Transilvania University of Braşov • Series I • Vol. 4 (53) No. 1 - 2011, p.7
- [13] Geels K., Fowler D., Koop W-U, Rückert, Metallographic and Materialographic Specimen Preparation, Light Microscopy, Image Analysis and Hardness Testing, ASTM International, U.S.A., 2007, pp 184-353
- [14] ***<http://www.mediacy.com/imageproplus>

DATA SCATTERING IN STRENGTH MEASUREMENT OF STEELS AND GLASS/EPOXY COMPOSITE

Adrian CATANGIU, Dan Nicolae UNGUREANU, Veronica DESPA

Valahia University of Targoviste, Faculty of Materials Engineering and Mechanics, Department of Materials Engineering, Mechatronics and Robotics
13 Aleea Sinaia Street, Targoviste, Romania

E-mail: acatangiu@yahoo.co.uk

Abstract. The strength of materials is a complex function which involve two main components, material nature and the presence of defects. Usually glasses exhibit a fragile behavior due to a numerous flaws and the effect is a large range of data scattering in tensile strength measurement. The Weibull probability density function was applied to describe the scatter of experimental data in tensile test, which emphasize a difference between variance in case of tensile strength of three stainless steel grades and glass epoxy composite. The main goal is mathematical modeling of those distributions and finding of equations which predict the probability of failure for a sample subjected to a specific stress.

Keywords: Weibull distribution function, tensile strength data scattering, glass/epoxy composite, analysis of variance

1. INTRODUCTION

Prediction of failure probability under a specific stress level could be an interesting tool in analysis of material behavior. The variability of a material characteristic it can be described by using Weibull distribution function [1] which cover a large scale of application, such as: fatigue performance [2, 3, 4], scatter of fracture toughness [5], probabilistic characterization in different static tests up to failure (four-point bending [6] or tensile test [7]).

In this paper, in order to obtain a relationship between stress level and failure probability was used Weibull distribution. For comparison, analysis of experimental data scattering in tensile test was performed also by using normal distribution.

The standard Weibull distribution function, which is shown in equation (1) has three parameters.

$$f(x; \beta, \lambda, \delta) = \frac{\beta}{\delta} \cdot \left(\frac{x - \lambda}{\delta} \right)^{\beta-1} \cdot e^{-\left(\frac{x - \lambda}{\delta} \right)^\beta} \quad (1)$$

where

β - is the shape parameter,

δ - is the scale parameter

λ is the location parameter of the distribution.

Each parameter has a specific significance as function of analyzed application. In case of tensile strength analysis, the current variable x is σ – ultimate tensile strength, λ - location parameter is the level of stress below which no fracture occurs, δ - scale parameter is usually the average of entire data set and shape parameter β (Weibull modulus) is a measure of experimental data scattering.

If the general function (1) is customized for distribution of fracture strength, the failure probability of a specimen subjected to stress level σ is given by:

$$F(\sigma; \beta, \sigma_{lim}, \sigma_0) = 1 - e^{-\left(\frac{\sigma - \sigma_{lim}}{\sigma_0} \right)^\beta} \quad (2)$$

Usually, for brittle materials is difficult to estimate a minimum value of tensile strength σ_{lim} under the material does not break certainly and in this case, the location parameter will be set to zero.

The same presumption can be also done for other type of materials in case of lack of safety data.

The strength of materials is a complex function which involve two main components, material nature and the presence of defects.

Usually ceramics and plastic materials exhibit a fragile behavior due to a numerous flaws and the effect is a large range of data scattering in tensile strength measurement.

The number of defects is dependent on sample size (large samples could have more defects as smaller ones, short glass fibers have higher strength then longer ones, etc.).

For this reason, in case of large size fragile materials samples there is a higher scattering of experimental data in tensile strength measurement than in case of smaller samples [6, 8, 9]. This phenomena (sample volume contribution in data scattering) is shown also in case of high isotropic materials such as stainless steel (Fig.1).

Specimen size is taken into account by changing the exponent of function which describes the failure probability. If is considered the breaking probability of a specimen of the volume V_0 as described by expression (2), the probability of fracture for a specimen of the same material and the volume V , under the same stress level σ is given by the equation (3) [9]:

$$F(\sigma; V) = 1 - e^{-\left(\frac{V_0 \cdot \sigma}{V \cdot \sigma_0}\right)^\beta} \quad (3)$$

From here, it can be formulated a practical conclusion, for specimens of material with the same resistance, more voluminous specimens show a higher probability of failure. In a similar manner, in case of the same probability of failure, specimens which exhibit higher volume have a lower tensile strength.

2. MATERIALS

Analysis of experimental data scattering, was performed on four type of materials, three stainless steel grades

(noted S1- grade 430 annealed (12 samples), S2- grade 316L annealed (20 samples) and S3- grade 301HT cold rolled and untreated (26 samples)) and a glass/epoxy composite (5 samples). The steel samples were cut out from head and tail of coils with 0.1 mm thickness. In order to emphasize the effect of specimens volume on the tensile strength, from S2 grade, were tested another 8 samples with 0.3 mm thickness provided from coils in the same state of heat treatment.

Composite plate has been made by four unidirectional prepreg plies HexPly M10 (50% volume fraction – E glass fibers) with stacking sequence [0/90/90/0] and 5 samples (noted GS₀) were cut out along fibers direction from external plies.

All tensile tests, up to failure, were performed according to DIN EN ISO 6892-1/ ISO 10113/ ISO 10275 by using a 30kN Zwick Roell machine.

A brief analysis of correlation between sample volume and tensile strength is shown in Fig.1.

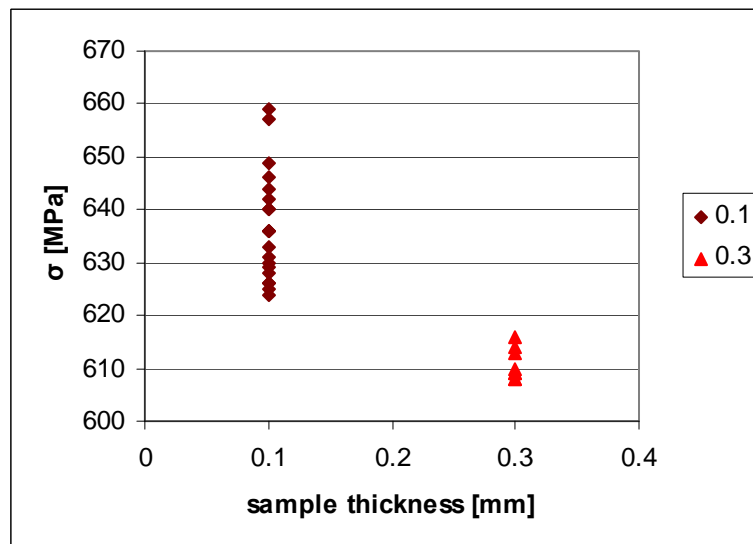


Figure 1. Ultimate tensile strength of samples with 0.1 and 0.3 thickness from grade S2

Even the difference is only 4% that it is not effect of imprecision measurement (normal scattering of experimental data due to measurement procedure or testing machine). It can be seen that even the maximum value of stress for thicker specimens is below the minimum value of thinner ones.

It should be specify clear that all the samples from grade S2 were annealed in same condition after plastic deformation. In explaining the differences, might be possible the influence of intense cold rolled hardening effect which is higher in case of thinner sheet.

The effects of cold rolling on thinner specimens may not be completely removed by annealing applied later. However in specimens with larger volume is higher the probability of defects occurrence which can reduce tensile strength. Experiments confirm the observations of researchers who have studied the influence of

specimen volume, even in relatively homogeneous and isotropic material such as stainless steel.

3. WORK PROCEDURE

3.1 Estimation of Weibull parameters

In theory, for a total number of samples $n < 100$, ranking the tensile strength test data according to the order from small to large, the cumulative failure probability is given by the Bernard formula [10]:

$$F(\sigma_i) = \frac{i - 0.3}{n + 0.4} \quad (4)$$

Starting from relation (2) and setting the parameter $\sigma_{lim} = 0$ (for brittle material there is not a limit of stress under the structure is safe - case of glass, ceramics and for steels we can make the same assumption in the absence of safety data) the Weibull distribution function becomes a two parameter function [11]:

$$F(\sigma_i; \sigma_0, \beta) = 1 - e^{-\left(\frac{\sigma_i}{\sigma_0}\right)^\beta} \quad (5)$$

If in the formula of Weibull distribution function is applied the double logarithm on both sides that is transformed into a linear relation such as equation (8).

$$1 - F(\sigma_i) = e^{-\left(\frac{\sigma_i}{\sigma_0}\right)^\beta} \quad (6)$$

$$\ln(1 - F(\sigma_i)) = -\left(\frac{\sigma_i}{\sigma_0}\right)^\beta \quad (7)$$

$$y = \ln\left(\ln\left(\frac{1}{1 - F(\sigma_i)}\right)\right) = \beta \ln(\sigma_i) - \beta \ln(\sigma_0) = \beta \cdot x + c \quad (8)$$

In order to estimate the parameters of function (β - slope of the curve and a measure of data scattering and the scale parameter σ_0) the calculus was performed according to procedure shown in Table 1, which is specific for those $n=12$ samples from S1 steel. For all tested materials has used the same procedure.

Table 1. Weibull parameters estimation (stainless steel grade S1)

Sample no. (i)	Ultimate tensile strength σ_i [MPa]	Probability of fracture $F(\sigma_i) = \frac{i - 0.3}{n + 0.4}$	$y = \ln\left(\ln\left(\frac{1}{1 - F(\sigma_i)}\right)\right)$	$x = \ln(\sigma_i)$
1	490	0.0565	-2.8455	6.1944
2	491	0.1371	-1.9142	6.1964
-	-	-	-	-
11	518	0.8629	0.6867	6.2500
12	523	0.9435	1.0558	6.2596

In Figure 1 is shown plot of the function in reciprocal double log scale on one axis (y) and a log scale on the

other for three grade of steel and a stratified bidirectional glass/epoxy composite.

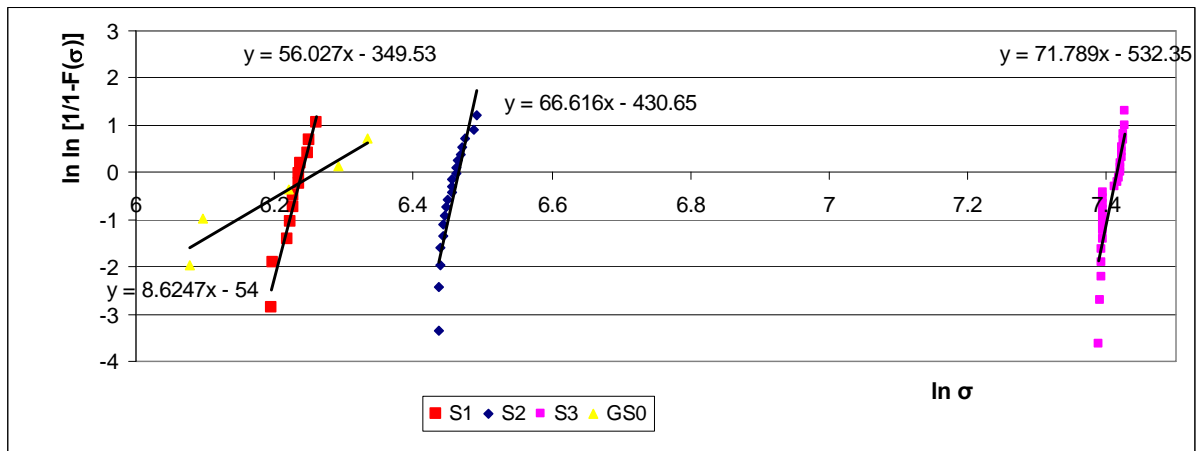


Figure 2. Weibull probability curves

Regression of experimental data has been performed and if trend line is a straight line, the material strength distribution can be described by using the two parameter Weibull distribution.

In order to compare the obtained parameter, were calculated according to normal (Gaussian) distribution the average, variance and standard deviation, results which are shown in Table 2.

It is obvious that the Weibull modulus β in case of composite (8.6247) is much lower than moduli for steels. The difference in experimental data scattering are due to composite material anisotropy, lack of homogeneity (two distinct phases: the glass

reinforcement and plastic matrix material), imperfect interfaces, presence of air voids during the resin cure.

The probability, in case of composite, to propagate and accumulate flaws that may cause breaking at stress values different from the average value is much higher than in homogeneous materials such as steels. The value of standard deviation associated with $\beta_{GS0} = 8.6247$, is $\sigma_{GS0} = 50.8$ MPa (10.2% from mean value) in comparison with values calculated for steels (e.g. $\beta_{S1} = 56.027$, $\sigma_{S1} = 9.56$ MPa, 1.88%).

The differences between the average calculated by estimating the Weibull function parameters and corresponding classical average for normal distribution are smaller than the standard deviation.

Table 2. Parameters of Weibull distribution and normal distribution

Parameter/Material	Symbol	S1	S2	S3	GS ₀	
Weibull distribution	shape parameter	β	56.027	66.616	71.789	8.6247
	constant term	c	394.53	430.65	532.35	54
	scale parameter	$\sigma_0 = e^{\frac{c}{\beta}}$	507.31	642.04	1661.51	523.78
Normal distribution	mean	μ	507.41	636.85	1648.96	497.4
	variance	σ^2	91.57	100.22	535.34	2580.64
	standard deviation	σ	9.56	10.01	23.13	50.8

3.2 Hypothesis distribution inspection

Making a first approximation we have the Weibull cumulative distribution function described in relations (9-12):

$$F_{S1}(\sigma; \sigma_0, \beta) = 1 - e^{-\left(\frac{\sigma}{507.31}\right)^{56.027}} \quad (9)$$

$$F_{S2}(\sigma; \sigma_0, \beta) = 1 - e^{-\left(\frac{\sigma}{642.04}\right)^{66.616}} \quad (10)$$

$$F_{S3}(\sigma; \sigma_0, \beta) = 1 - e^{-\left(\frac{\sigma}{1661.51}\right)^{71.789}} \quad (11)$$

$$F_{GS0}(\sigma; \sigma_0, \beta) = 1 - e^{-\left(\frac{\sigma}{523.78}\right)^{8.6247}} \quad (12)$$

In order to validate the form of function described above we must perform hypothesis distribution inspection. Generally are used nonparametric methods for comparing two set of distribution, in our case Bernard approximation and Weibull distributions (9-12).

One method of analysis is Kolmogorov-Smirnov test (the best option mainly due to its sensitivity with small sample size) in which maximum difference between the empirical distribution function of the sample (Weibull) and the cumulative distribution function of the reference distribution (Bernard) have to be lower than KS constant (for a given number of samples and a given significance level).

$$\max |F_W(\sigma_i) - F_B(\sigma_i)| < D_{(n,\alpha)} \quad (13)$$

The significance level is usually set to 0.05 which means a 95% confidence interval.

The procedure is illustrated for S1 stainless steel in Table 3.

Table 3. Kolmogorov –Smirnov test

Sample no. (i)	Ultimate tensile strength σ_i [MPa]	Probability of fracture $F_B(\sigma_i) = \frac{i-0.3}{n+0.4}$	Probability of fracture $F_W(\sigma_i) = 1 - e^{-\left(\frac{\sigma}{507.31}\right)^{56.027}}$	$D_i = F_W(\sigma_i) - F_B(\sigma_i) $
1	490	0.0565	0.133105	0.076653
2	491	0.1371	0.147959	0.010863
-	-	-	-	-
11	518	0.8629	0.959785	0.096881
12	523	0.9435	0.995932	0.052383
Max (D _i)				0.207643
Kolmogorov-Smirnov statistic $D_{(12,0.05)}$				0.375 [12]

4. RESULTS AND DISCUSSION

The test results (cumulative distribution function CDF) are also shown in Fig.3. The error bars, added to Weibull distribution function values, have fixed value equal with Kolmogorov - Smirnov statistic.

It can be seen that all the values provided by normal cumulative distribution function (according to Bernard's approximation) are inside the bars, which emphasize that relation (13) is respected.

In this condition, the tested distribution is accepted according to the KS method and is reasonable the assumption that, the tensile strength of S1 steel it can be described by using two parameter Weibull distribution.

In Table 4 are shown results of KS test applied for all steels and composite.

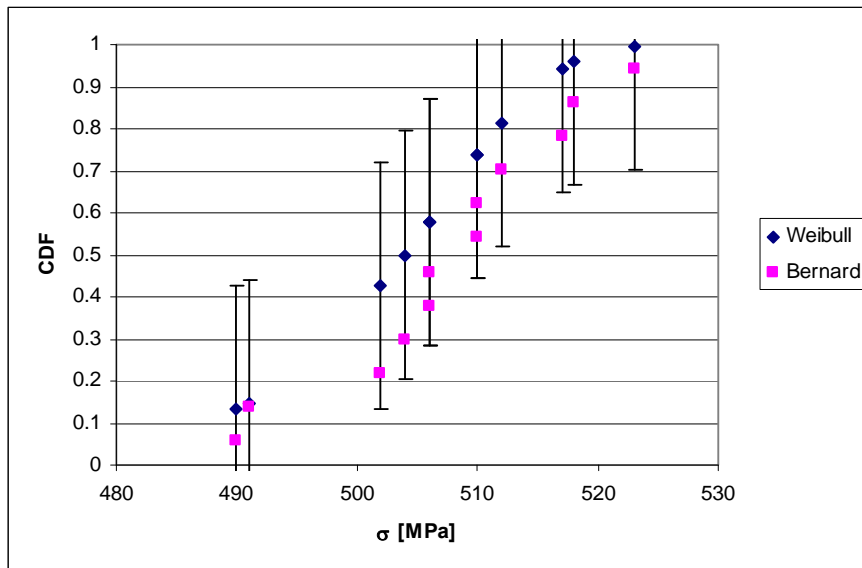


Figure 3 Hypothesis distribution inspection of empirical cumulative distribution function

Table 4. The results of Kolmogorov – Smirnov test

Material/Symbol	No. of samples	$\max F_w(\sigma_i) - F_B(\sigma_i) $	KS test (significance level $\alpha = 0.05$) [12]
Steel S1	12	0.207	$D_{(12,0.05)}=0.375$
Steel S2	20	0.104	$D_{(20,0.05)}=0.294$
Steel S3	26	0.266	$D_{(26,0.05)}=0.259$
Composite GS ₀	5	0.134	$D_{(5,0.05)}=0.563$

As can be seen in Table 4, except S3 grade, we may consider that the distribution of experimental data in case of tensile strength measurement could be estimated by a two parameters Weibull distribution.

The hypothesis distribution inspection of functions shown in relations (9), (10), (12) reveals that, for each case, the Kolmogorov – Smirnov test value is lower than

maximum difference between Weibull and Bernard cumulative distribution functions. For specimens of grade S3 (with cumulative distribution function shown in equation (11)) should be performed an extra analysis of that apparently different distributions from 'normal' distribution, because Kolmogorov – Smirnov test is not verified.

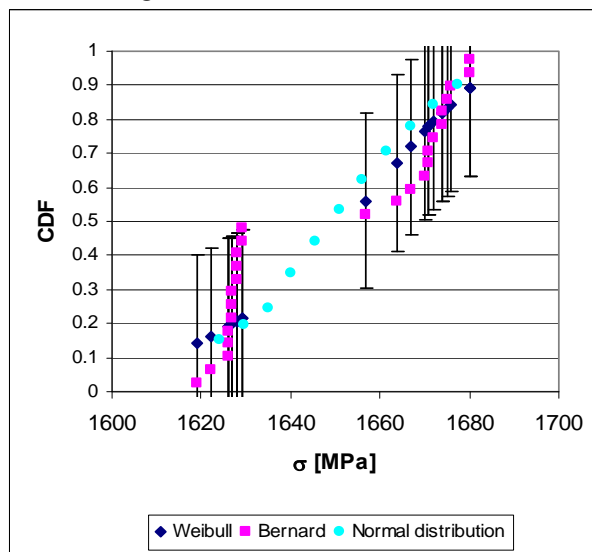


Figure 4. Weibull, real and normal cumulative distributions

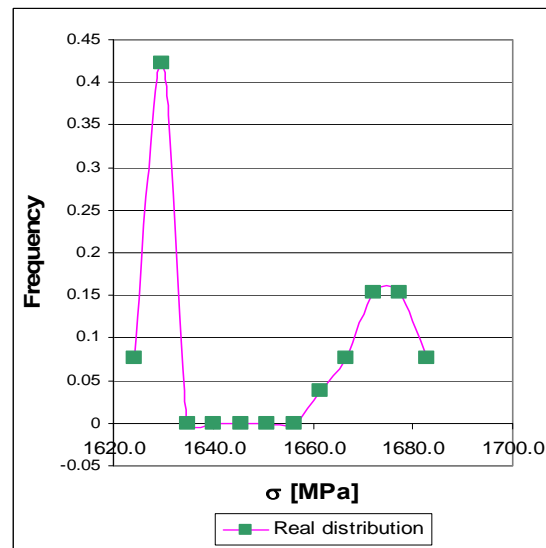


Figure 5. Real distribution

First of all, the experimental data were divided in intervals and have been calculated the frequencies for each interval according to procedure described in [13].

As shown in Fig.4, the Weibull distribution is close to normal one, but the values of cumulated frequency calculated with Bernard relation seems to be far away for some stress values situated at the beginning of the stress range. It can be seen that the real distribution in case of S3 grade steel is a bimodal distribution, shown in Fig.5.

In case of S3 grade the “abnormal” distribution has a simple origin.

This is due to sample prelevation place (these are cut out from head and tail of coils). We can consider that there is a continuous variation of tensile strength along the coil length but in our tests the values around average are missing.

The data should be a statistically random sample of the population, but in case of real cumulative distribution function curve the value 0.5 which is usually specific for average of data set, is specific for the second frequency interval (the total number of samples is 26).

We can consider that the Weibull distribution function could describe the tensile strength distribution even in case of S3 grade (equation has valability in case of an entire coil), but Kolmogorov - Smirnov test in our particular situation does not verify hypothesis distribution because the particularly values for specimens tested are just a part of a statistically random sample of entire population (specimens are characteristic just for coil extremities).

5. CONCLUSIONS

Tensile strength distribution (the scatter of experimental data) could be described by using two parameter Weibull function.

It is obvious that the Weibull modulus β in case of composite (8.6248) is much lower than moduli for steels (56, 66.6, respective 71,7).

A large β is associated with a narrow interval for experimental data scattering. The standard deviation in case of glass/epoxy composite is 50.8, in comparison with those in case of steels (9.56, 10.01 and 23.13).

The difference in experimental data scattering are due to composite material anisotropy, a lack in homogeneity (two distinct phases: the glass reinforcement and plastic matrix material), imperfect interfaces, presence of air voids during the resin cure. Fiber strenght and orientation could have also an statistical effect in composite and that will be the subject of future work.

In case of samples from steel plate, the probability of defects presence increases with thickness of plate.

The comparison between predicted value and experimental data reveals that Weibull distribution provide an accurate instrument for analysis of data variability, despite fact that for S3 grade KS test reveal an nonconformity.

Because the samples are cut out from head and tail of coils, non-normal distributions (bimodal distribution) is possible.

That is just the effect of limitation in chosing of sampling site. Between head and tail of a coil is a continuous series of tensile strength values and is reasonable to believe that the mean for entire coil is specific for samples situated in the middle of the coil.

REFERENCES:

- [1] W. Weibull, A statistical theory of the strength of materials, Proceeding of the Royal Swedish Institute of Engineering Research ,151,1 (1939).
- [2] J. Schijve, Statistical distribution functions and fatigue of structures, International Journal of Fatigue 27, 1031–1039, (2005)
- [3] S. Mohd, Y. Otsuka, Y. Miyashita, Y. Mutoh, Statistic characteristics of fatigue properties in magnesium alloy, Procedia Engineering 10, 1232, (2011)
- [4] Yan Lv, H.Cheng, Z. Ma, Procedia Engineering, Fatigue performances of glass fiber reinforced concrete in flexure ,31, 550 (2012)
- [5] T. Tagawa, M. Ohata, F. Minami, Statistical evaluation of fracture toughness with stable crack extension, Procedia Engineering 10, 827, (2011)
- [6] M. J. Lamela, A. Ramos, P. Fernández, A. Fernández-Canteli, C. Przybilla, C. Huerta, A. Pacios, Probabilistic characterization of glass under different type of Testing, Proceeding Materials Science, 3, 2111 (2014)
- [7] M. E. A. Fidelis, T.V.C. Pereira, O. F.,M. Gomes, F.A. Silva, R.,D.T.Filho, The effect of fiber morphology on the tensile strength of natural fibers, Journal of Materials Research and Technology, 2(2), 149, (2013)
- [8] X Hu, L.Liang, S.Yang, Weibull-strength size effect and common problems with size effect models, Proceedings of the 8th International Conference on Fracture Mechanics of Concrete and Concrete Structures,FraMCoS-8 https://www.researchgate.net/publication/268152093_weibull-strength_size_effect_and_common_problems_with_size_effect_model, (2013)
- [9] R. Asthana, A. Kumar, N. Dahotre, Materials Science in manufacturing, Academic Press, Elsevier Inc., (2006)
- [10] C. Przybilla,A. Fernández-Cantelia, E. Castillo, An iterative method to obtain the specimen-independent three parameter Weibull distribution of strength from bending, Procedia Engineering, 10, 1414, (2011)
- [11] G. Peiying, D. Chang, T. Lei, Determination of local damage probability in concrete structure, Procedia Engineering, 28, 489, (2012)
- [12] L. Sachs, Angewandte Statistik, Springer, 427 – 431, (1997)
- [13] I. Ciuca, S. Dimitriu, Modeling and optimization of plastic deformation and heat treatment metallurgical processes (in romanian), Modelarea si optimizarea proceselor metalurgice de deformare plastica si tratamente termice, Ed. Didactica si Pedagogica Bucharest, (1998)

STRUCTURAL TRANSFORMATIONS DURING TEMPERING IN THE STEELS WITH HIGH CONTENT OF MO AND CO

Florina Violeta ANGHELINA, Dan Nicolae UNGUREANU

Valahia University of Targoviste, Faculty of Materials Engineering and Mechanics,
Department of Materials Engineering, Mechatronics and Robotics
13 Aleea Sinaia Street, Targoviste, Romania

E-mail: vianghelina@yahoo.com

Abstract. *The structural transformations occurring at tempering for some high-speed steels are a subject of research for which have been dedicated numerous studies. More complex compositions of the high-speed steels were direct consequence of the complexity of structural transformations which occur during heat treatment. On the other hand, current tendency in energy requires maximum efficiency and rational use of heating sources used in industry. Thus, only a precise knowledge of the kinetics of transformations occurring at tempering can be a basis for optimizing this treatment. Although cobalt is used for a long time as an alloying element, though relatively recently it was considered important to the properties of rapid steel. These circumstances, combined with the lack of quantitative information on the kinetics transformation at tempering operation treatment for some steel has led to this paper. The thickness of the studied samples is 5 mm and was taken from the annealed steel bars. These samples were subjected to hardening and tempering treatment in salts bath. Heating for hardening was performed in two steps, at 5500C and 8300C. Austenitizing was done at 12000C, during 120 seconds. The cooling was done up to 5300C in salts bath, with a keeping of 15 seconds, and then air cooling was done. On these samples were carried out, HRC Rockwell hardness measurements, and X-ray diffraction analysis.*

Keywords: *high-speed steels, heat treatment, tempering operation, hardness measurements*

1. INTRODUCTION

Alloying elements such as cobalt, molybdenum, wolfram, chrome and others have considerable influence on the properties of high-speed steels. These circumstances, combined with the lack of quantitative information on the kinetics transformation at tempering treatment for some steels has led to this paper. High-speed steels of tools (STAS 7382-80) are rich alloy steels (up to 25%) with W, Cr, Mo, V, Co, with a 0.7- 1 % carbon content. High-speed steels are steels that unlike carbon steel and alloy steels of tools possess the most appropriate assembly for cutting properties (wear resistance and heat stability).

These steels are intended for manufacturing cutting tools who process at high speeds (40-50 m/min) hard materials (HB 280), lathe tools, milling cutters, drills, threading tools, etc. The most high-speed steels are steels with W (Rp3) with Co (Rp1, Rp2) and with Mo (Rp5, Rp10). Mechanical properties of hardened and tempered alloy steel, differ greatly from the mechanical properties of a carbon steel of the same carbon content, hardened and tempered at the same temperature. Alloy steel will present strength and toughness superior to carbon steel. Tempering temperature influences the mechanical properties of alloy steels, according to the literature [1-8] can be illustrated by diagrams of variation a mechanical properties with tempering temperature

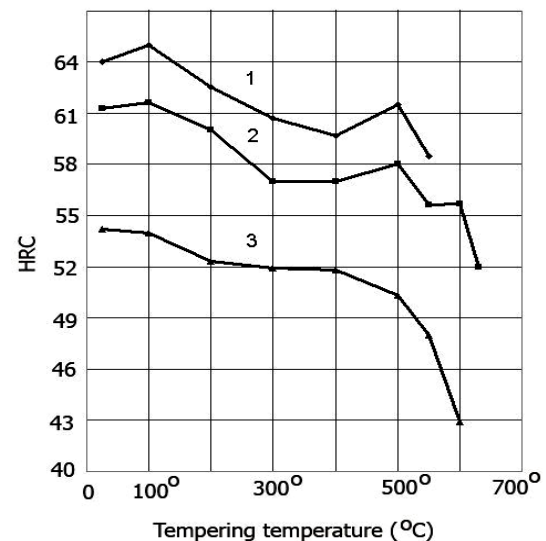


Figure 1. Tempering temperature influence on the hardness of high-speed steel, tempered at different temperatures [8]

Variation of hardness of high-speed steel in tempered state depends on temperature.

Hardness variation and the proportion of residual austenite on the tempering at 5600 C are shown in the images below (figure 1 and figure 2):

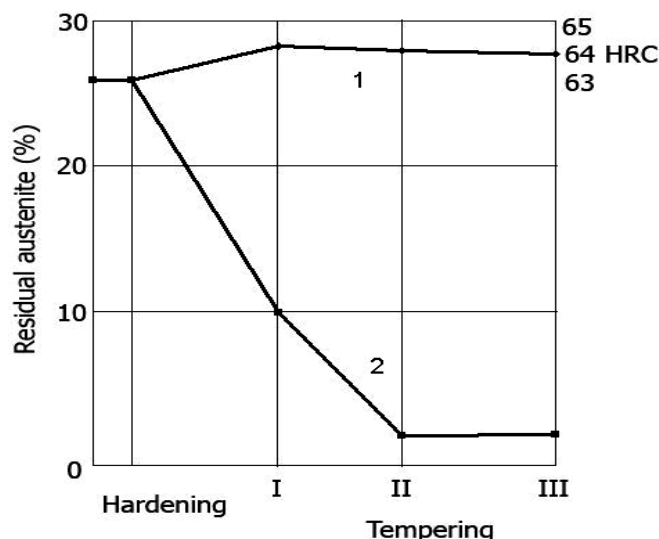


Figure 2. Variation of hardness and the amount of residual austenite on the tempering at 560^o C [8]

2. EXPERIMENTAL TECHNIQUE

Table 1. Chemical composition of sample

Elements	C	Mn	Si	S	P	Cr	Ni	Cu	Mo	Co	W	V
Concentration(%)	1.03	0.27	0.09	0.09	0.26	3.78	0.16	0.17	9.56	8.63	2.03	1.23

For this study we used the annealed steel bars at $\Phi = 30$, from which were cut samples, in the form of a disc. By mechanics machining all samples were brought to the 5 mm same thicknesses. Samples thus prepared were hardened and tempered in salts bath. Heating for hardening was done in 2 stages at 550^oC and 830^oC. Austenitization was executed at 1200^oC for 150 seconds. Cooling has been done up to 530^oC in salts bath, for 15 seconds, and then, in the air. The conditions of tempering have been preset in order to obtain the information necessary for drawing kinetic curves.

For these samples thus treated were made -HRC Rockwell hardness measurements, and also the X-ray diffraction measurements. After each treatment stage, by machining, the surface layer was removed having about 0.2-0.3 mm thickness. After this stage was carried out chemical corrosion to remove damaged layer because

3. EXPERIMENTAL RESULTS

Preliminary determinations have been preliminary tempering treatments at a temperature of 100-3000 C for 1h, for thermal stabilization of austenite. Based on preliminary determinations, according to the tempering

mechanical processing. After this processing were carried all measurements. For hardness measurements were carried out a minimum 6 hardness tests at a device type PH-C-01/02, with a maximum load of 150kgf. The X-ray diffraction analyzes was carried out on a Phillips PW 1130/90 diffractometer equipped with a vertical goniometer PW 1050/70 type.

Registration of diffracted radiation was done with a proportional counter and for the monochromatic radiation has been used curved crystal graphite mounted in diffracted beam. Depending on the aimed purpose has been used radiation of copper, cobalt and iron. To determine the lattice constant for martensite is best to use the maximum (211).

This maximum occurs in iron radiation at $2\theta = 110.50^{\circ}$ angle and does not overlap with other peaks obtained for other structural constituents present in the sample.

temperature, in the conditions recommended by current standards, was obtained hardness variation with tempering temperature for 3 tempering operation of 60 minutes each. The result is shown in Figure3:

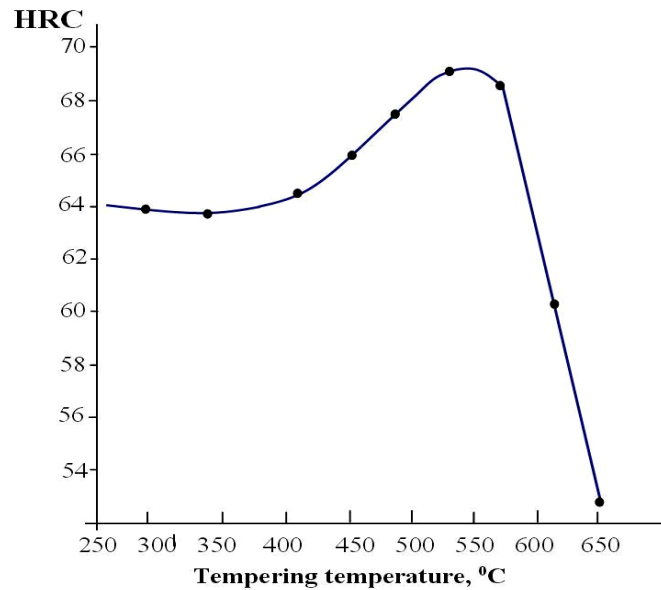


Figure 3. Hardness variation with tempering temperature

From this curve resulted that the temperature for obtain a maximum hardness is situated in the range 540°C - 560°C and therefore she was chosen as tempering temperature the temperature of 550°C . In the hardening state steel structure consisted of: martensite, residual austenite and M_6C , MC and M_{23}C_6 carbides. The largest share of carbides in the tempered state had a M_6C . The other types of carbides were found in much smaller amount

but they gave diffraction peaks clear enough to be identified without doubt. During tempering treatment of steel, in the initial stage, initial austenite is transformed to martensite. The amount of residual austenite decreases after at least 2 tempering treatments attaining minimum values ($< 15\%$) with beneficial effects on physical and mechanical characteristics of steels. In figure 4 is shown kinetics curve for transformation of residual austenite.

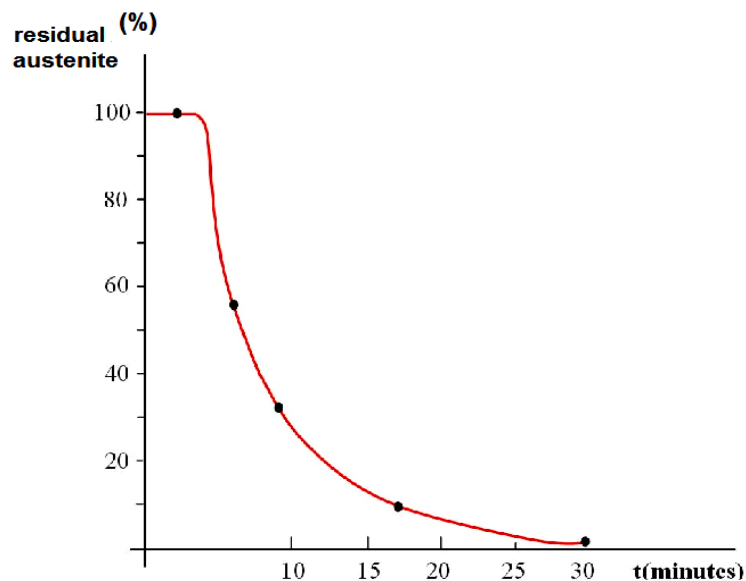


Figure 4. Kinetics curve for transformation of residual austenite

From figure 4 we see that after isothermal maintaining approx. 4 minutes the transformation starts. Just two minutes after the start the transformation residual austenite amount reaches half of the initial (in figure 4 represented by ordinate axis the amount of austenite in relative units, considering initial amount that corresponds at division 100). With further increasing the duration of maintenance, transforming speed begins to

decrease. It will be seen that after a 30 minute maintaining at 550°C , the amount of residual austenite reaches the limit of detection obtainable by X-ray diffraction (1.5%), a value below which no practical influence material properties. During of the tempering operation the martensite lattice parameter varies with time as shown in figure 5.

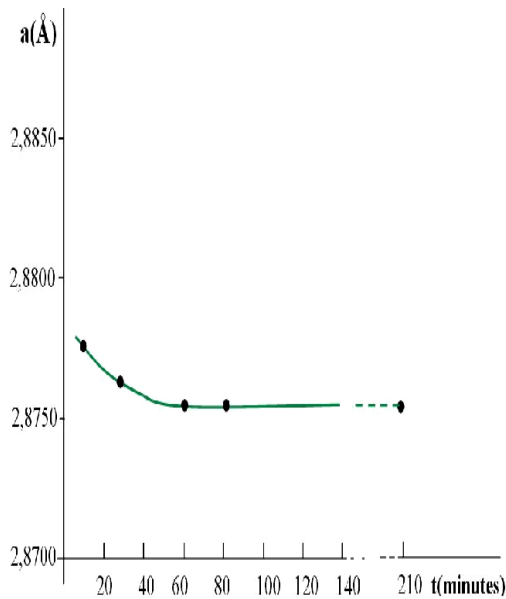


Figure 5. The martensite lattice parameter variation according to the time of tempering

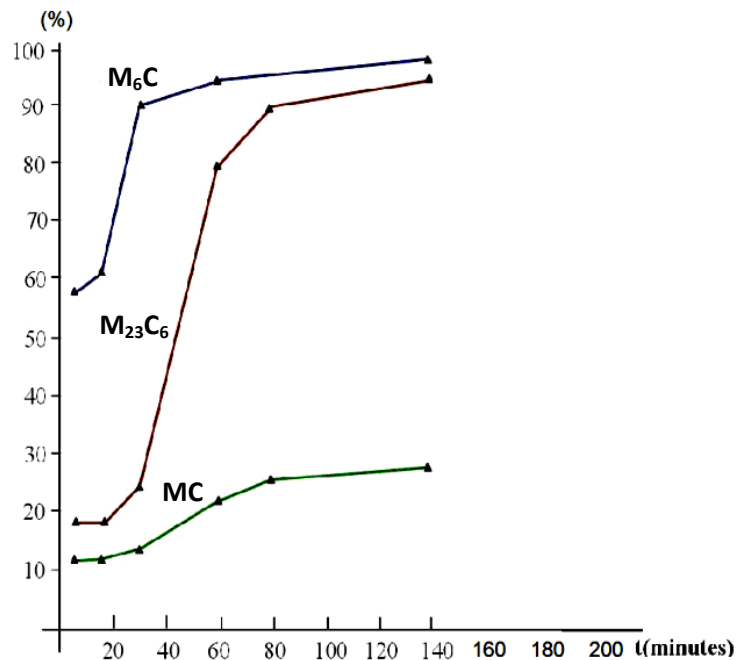


Figure 6. The curves depicting the kinetics of precipitated carbides

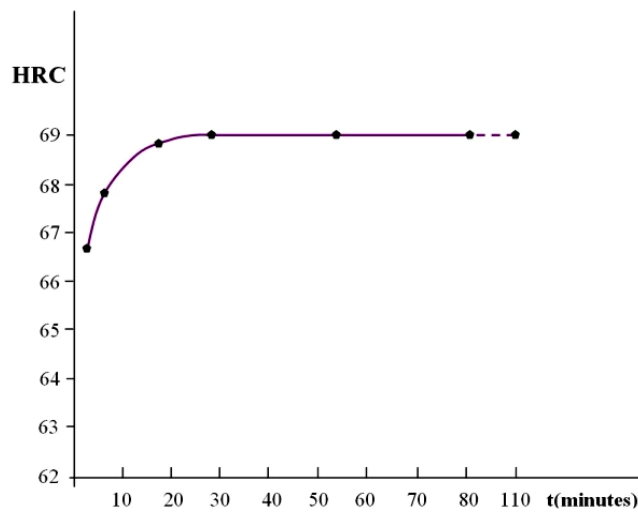


Figure 7. The maximum hardness of investigated steel

Figure 6 shows, in relative units, the curves depicting the kinetics of precipitated carbides, the maximum value being reached precipitates after a period of 80 minutes. In consensus with the other transformations has been observed as well as compounds such as the carbides, reach the maximum amount after about 80 minutes of isothermal maintaining.

4. DISCUSSION

For high-speed steels, the tempering must lead, first of all, to a high value of secondary hardness and also this treatment must eliminate the annealing tensions in order to improve the resistance of tools. High-speed steels after quenching have a significant amount of residual

austenite (20% -30%). Therefore is need to execute tempering treatment for increasing resistance at plastic strain for tools and it is necessary as to obtain a total transformation of residual austenite [9]. For this purpose we recommend multiple tempering operations.

For the studied steel these requirements are made for shorter heat treatment durations in comparison with the recommended standards for high-speed steels [10÷16]. Thus, as shown in figure 7, the maximum hardness is obtained at 550°C after a maintaining interval of 30 minutes (figure 7). Analysis figure 3-7 allow us to conclude that the tempering operation is completed after a total duration of 80 minutes when the martensite lattice parameter attain a constant value (see figure 5) and the amount of precipitated carbides attain a the

maximum value. Further increasing the duration of treatment, leaves practically unmodified the constant lattice. There are, however, other changes in the diffraction image, that changes the shape and width of the lines, both the matrix and the carbides. But because these changes are closely related the fine structure and the existing defects in phases, this problem will be the subject of another paper.

Determined measurements, i.e. hardness, lattice constant and precipitated carbides behave additive compared to isothermal maintaining time. Therefore, the final tempering treatment may be achieved by three tempering with of shorter duration. Of course, depending on the use of steel should have different properties so cannot establish a definitive treatment without knowing the properties that result from tempering operation.

The experimental results presented in this paper are intended to create a database relating to optimizing the applications of tempering treatments on high-rapid steels. This fact is to reduce the number of tempering treatments applied to steels and correlation of these with the amount of martensite at the expense of the amount of residual austenite, and implicitly to increase hardness and resistance to plastic strain at tools. Thus, the total final time of heat treatment is low and has positive effects on reducing production costs. Hot hardness test was conducted on a number of three samples subjected to three tempering of 30 minutes each at a temperature of 550 °C. After being held for four hours at 640°C hot hardness for the three samples was respectively 60.5 HRC, 61 HRC and 60.8 HRC. All these values is higher than the permissible limits of the standards for high-speed steel, value is 58 HRC.

5. CONCLUSIONS

The analysis of data presented in the paper result as follows:

- a) The tempering operation of the studied steel processes practically ends after approx. 80 minutes to isothermal maintaining at 550°C.
- b) The hardness, lattice constant, the amount of precipitated carbides are determinations that behaves as well as the additive size in relation to isothermal maintaining time at 550°C, which shows that the same results can be obtained by repeated tempering, but shorter.
- c) Variation a lattice constant with to isothermal maintenance time highlights the diffusive nature of the transformation occurring into martensite during tempering operation.
- d) The process of tempering achieved by multiple tempering operations is much shortened compared to the recommended standards. From the data of this papers may be recommended to make a tempering operation in three consecutive tempering to 550°C with duration of 25-30 minutes each.

REFERENCES

- [1] D. Liedtke, Über das Härten und Anlassen von Schnellarbeitsstahl in Theorie und Praxis. HTM Härtereitechn. Mitt. 32 (1977) 2, S. 49.
- [2] D. Liedtke, Zum Verschleißverhalten nitrocarburiertes Stähle, HTM Härtereitechn. Mitt. 42 (1987) 4, S. 197.
- [3] B. Fredriksson, Optimization of the Tempering Time for High Speed Steels.- Bull. Cercle metaux, 1975, num.spec., p.351-362.
- [4] B. Fredriksson, Optimizing Tempering Time for High Speed Steels.- Metal Prog., 1977, vol.112, Nr.3.
- [5] Waldenstrom M. An experimental study of carbide-austenite equilibria in iron-base alloy with Mo, Cr, Ni and Mn. -Met. Trans., 1977, A8, Nr.12.
- [6] Yu. A. Geller, Tool Steels [in Russian], Metallurgiya (1975).
- [7] A. N. Popandopulo, L. T. Zhukova, Transformation in high-speed steels during cold treatment, Metal Science and Heat Treatment, October 1980, Volume 22, Issue 10, pp 708-710.
- [8] Information by sheet OTCM-OS-G/1983/pg.10-14.
- [9] Yu. A. Geller, Instrumental'nie Stali, Moskva, Metallurgiya, 1975.
- [10] F.V. Anghelina, D.N. Ungureanu, V. Bratu, I.N Popescu, C.O. Rusanescu, Fine structure analysis of biocompatible ceramic materials based hydroxyapatite and metallic biomaterials 316L, Applied Surface Science 285 A, 65-71.
- [11] B.A. Olei, I. Ștefan, N. Popescu, The Influence of the Sintering Temperature on the Wear Testing for Some Steels Samples Obtained by Powder Metallurgy, Solid State Phenomena 216, 216-221.
- [12] I.N. Popescu, D. Bojin, I. Carceanu, G. Novac, F.V. Anghelina, Morphological and structural aspects using electronic microscopy and image analysis of iron powders obtained by water atomization process, Journal of Science and Arts 12, Year 10, No. 1(12), pp. 125-134, 2010.
- [13] Mario Rosso, Ildiko Peter, Federico Simone Gobber, Overview of heat treatment and surface engineering, influences of surface finishing on hot work tool steel, International Journal of Microstructure and Materials Properties, Special Issue on: "Industrial Tools and Material Processing Technologies part 1", in press.
- [14] Olimpia Ghermec, Cristian Ghermec, Iulian Stefan, Research Regarding the Wear of Ecological Steels Obtained Through the Carburizing of Iron Metal Powders, Hidraulica, 4(2013) 52-57.
- [15] Lucica Grigora Toma, Rodica Mariana Ion, Radu Claudiu Fierascu, Nelu Ion, Ileana Nicoleta Popescu, Energy Dispersive X-Ray Fluorescence (EDXRF) Analysis of Steels, Journal of Science and Arts 13 (2), 385-390.
- [16] Carmen Otilia Rusanescu, Marin Rusanescu, The stress-strain curves determined for microalloy steel with determined on the torsion tests, Metalurgia , 59 (1) (2007), 38-44.

STUDY ON HYDRATION AND STRENGTHENING OF HIGH ALUMINA CEMENTS

Nicolae ANGELESCU¹, Cristina STANCU², Sofiane AMZIANE³,
Vasile BRATU¹, Elena Valentina STOIAN¹

¹Valahia University of Targoviste, Faculty of Materials Engineering and Mechanics,
Department of Materials Engineering, Mechatronics and Robotics
13 Aleea Sinaia Steet, Targoviste, Romania

²Ceprocim S.A. Bucharest

³University Blaise Pascal Clermont II Clermont-Ferrand, France

E-mail: angelescu@yahoo.com

Abstract. Refractory concretes based on aluminous cements are used with great success in areas where high temperatures are required. The mineralogical composition of the high alumina cement is the main factor which gives the physical and mechanical properties at high temperatures of refractory monolithic materials.

It is therefore desirable to use high alumina cements based on mineralogical compounds with high refractoriness, because in the end those beneficial properties can be found in the final product - refractory concrete.

The aim of this paper is to design, realize and characterize different compositions of high alumina cements based on mineralogical compounds with the highest refractory from the CaO-Al₂O₃ binary system (i.e. CA, CA₂, and CA₆), and to find ways of hydraulic activation of calcium hexa aluminate, also.

Keywords: calcium monoaluminate, calcium dialuminate, calcium hexa aluminate, activated hydration, mechanical strength, additive, highly refractory compound.

1. INTRODUCTION

The main mineralogical constituents of high alumina cement that have hydraulic activity and which are important for the manufacture of refractory concretes are: monocalcium monoaluminate (CA) and monocalcium dialuminate (CA₂) which, by hydration, develop mechanical strength.

To achieve a refractory concrete that can be used at very high temperature, it must be use high refractory hydraulic binders such as high alumina cement with a content of alumina $\geq 70\%$. An alternative technological option that can have the same result, and which it is showed in this paper, is to design a binder matrix whose value of molar ratio Al₂O₃/CaO is higher than the one corresponding to monocalcium dialuminate [1, 2].

The types of binder matrix (high alumina cements) used in this papers are base on CA₆ and CA₂, on CA₂, CA and closer to stoichiometric CA₂ (an industrial Alcoa cement).

But once the value of molar ratio Al₂O₃/CaO is increasing the interaction with water of the mineralogical compounds is decreasing together with it the mechanical strength decreasing, too. But in the calcium aluminates series, the refractoriness increases with the basicity decrease and enrichment in alumina as follows: C12A7 < CA < CA₂ < CA₆. The mineralogical compound with the highest refractoriness from the calcium aluminates series is CA₆, whose Al₂O₃/CaO molar ratio is 6:1. However, due to the fact that with the enrichment

in alumina of the mineralogical compound the hydraulic activity decreases dramatically, the presence of CA₆ was avoided [2]. To counteract this deficiency it can be use some additives with activation of hydration properties for CA₆. From the great variety of high alumina cement activation of hydration must be chose the one that improve the physical and mechanical properties at room temperature and which do not affect refractoriness. One such activation of hydration is calcium sulfoaluminate. The data from literature indicates that it presence can enable interaction with water of high alumina cement, especially of the high refractory mineralogical compounds: CA₂ and CA₆ [3, 4].

2. MATERIALS

The raw materials used to made high alumina cements on CA₆ and CA₂ and, respectively, based on CA₂, were reactive alumina (Al₂O₃ content = 99.50%) and calcium carbonate (CaCO₃ content = 99.70%).

The raw materials used to made calcium sulphoaluminate, the activator of interaction with water for CA₆ and CA₂, were reactive alumina (Al₂O₃ content = 99.50%), calcium carbonate (CaCO₃ content = 99.70%) and dehydrate calcium sulphate (CaSO₄·2H₂O content = 99.98%).

In order to achieve the high alumina clinkers, which by grinding were obtained cements based on CA₂ and CA₆ and respectively based only on CA₂, we used the CaO-

Al₂O₃ binary system to choose the composition of mixtures of raw materials and heat treatment temperatures.

For increasing the molar ratio Al₂O₃/CaO from high alumina cement based on CA and CA₂ was used reactive alumina.

The high alumina cements based on high refractory compound were characterized in parallel with the additivated samples and with the increasing Al₂O₃/CaO molar ratio samples. The percent in which the additive (calcium sulphoaluminate - C₄A₃S̄) was added to the cement is 5%. The Al₂O₃/CaO molar ratio was 4.0 for the high alumina cement based on the usual cement with molar ratio Al₂O₃/CaO = 2.5 with addition of alumina (see Table 1).

Table 1. Oxide composition of high alumina cements

Cement type	Al ₂ O ₃ (%)	CaO (%)	SiO ₂ (%)	Fe ₂ O ₃ (%)	Alkalies (%)	SO ₃ (%)	MgO (%)	CaO free (%)
CA6+CA2	85.33	14.24	0.15	0.12	0.0	0.00	0.13	0.00
CA2	77.60	22.20	0.10	0.09	0.0	0.00	0.08	0.00
CA+C A2	70.91	27.89	0.22	0.20	0.2	0.30	0.27	0.00

3. EXPERIMENTAL CONDITIONS

Before starting to characterize these types of cements, they must to be identified in the CaO-Al₂O₃ binary system characteristic to the super aluminous cement, shown in Figure 1.

The point shown in Figure 1 by C1 corresponds to the mineralogical composition of super aluminous cement based on CA₂ and CA₆ and C₂ point corresponds to the mineralogical composition of super aluminous cement based on CA₂. Regarding the location of industrially super aluminous cement composition, it is known only the fact that it can be located in CA - CA₂ subsystem.

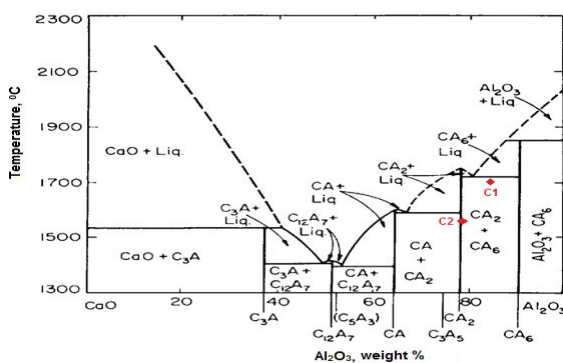


Figure 1. Phase diagram of CaO-Al₂O₃ system

It can be seen from Table 1 that all three cements have an alumina content exceeding 70%, threshold limit value considered for an aluminous cement to be use in making refractory's used in applications that can be use

at very high temperatures.

In the Figures 2 to 4 are presented the X-ray diffraction spectrum of cements used in the experiments presented here in order to show that the composition corresponds to the chosen propose.

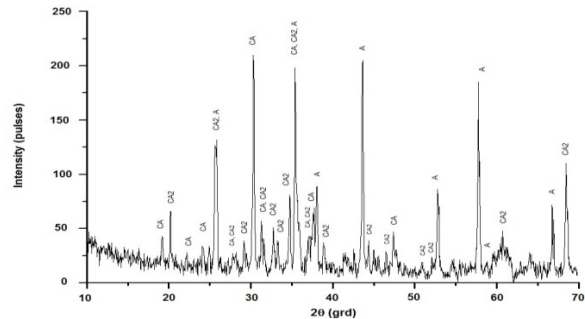


Figure 2. X-ray diffraction spectrum of super aluminous cement based on CA and CA₂

Analyzing the peak intensity of ordinary super aluminous cement, the following mineralogical compounds were identified: CA (2.9625Å, 4.6672Å, 2.5132Å) and CA₂ (3.5000, 2.5990Å, 4.4400Å), together with A (2.0650Å, 2.5230Å, 1.5900Å).

Well defined peaks of alumina presence from the composition of ordinary super aluminous cements is explained by the fact that usually the one obtained in industrially have the composition corrected by adding alumina, thus explaining the high alumina content obtained by chemical analysis which does not correspond to the place in CaO-Al₂O₃ binary system.

Analyzing the shape and intensity of the peaks corresponding X-ray diffraction spectrum of the experimental super aluminous cements presented in Figures 3 and 4, it can be seen that in the analyzed samples were formed the mineralogical compounds wanted: CA₆ (2.4780Å, 2.6230Å, 2.1090Å) and/or CA₂ (3.5000, 2.5990Å, 4.4400Å), corresponding to the composite selected from CaO-Al₂O₃ phase diagram for these cements. Along with these compounds was also found unreacted alumina (2.0650Å, 2.5230Å, 1.5900Å) from the raw mix.

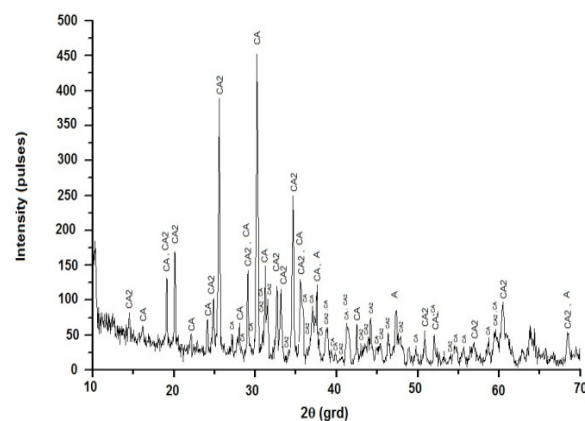


Figure 3. X-ray diffraction spectrum of super

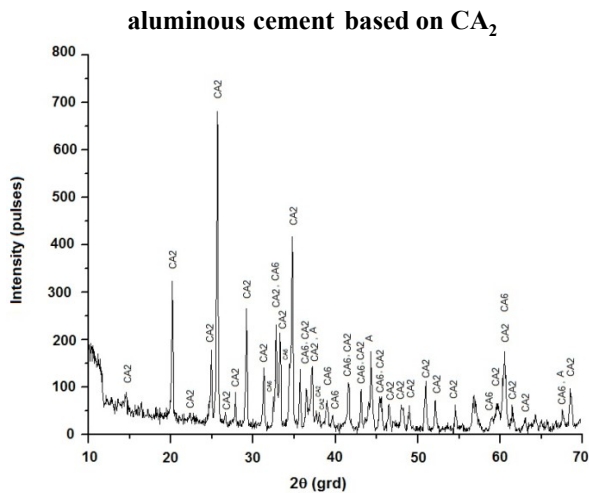


Figure 4. X ray diffraction spectrum of super aluminous cement based CA₆ and CA₂

4. RESULTS AND DISCUSSIONS

For a better understanding of the properties of the new high alumina cements, the results obtained after the physical and mechanical characterisation will be presented versus the ones obtained on the same cements but with 5% additive and with the one with addition of alumina, see Table 2 for characterisation at normal conditions and Table 3 for characterisation after exposure at high temperature.

Regarding the water content for standard consistency for the high alumina cements types studied in this paper is correlated with specific surface area and complies with the recommended values (see [5, 6, 7]).

Setting time of high alumina cements is related with the mineralogical composition. As it was anticipated from the moment of choosing the compositions of sintered alumina cement based on CA₂ and CA₆, the initial setting time and final setting time are much longer than those of high alumina cement based on CA₂ that has a higher basicity.

With the addition of 5% C₄A₃Š the initial and final setting times of high alumina cement were significantly shortened, Table 2. The initial setting time was reduced by approx. 63% - 64% and final setting time was reduced by approx. 80 - 84% for both high alumina cements with additive versus the samples without additives.

The values of compressive strength obtained for high alumina cement based on CA₂ and CA with molar ratio Al₂O₃/CaO = 2.5 are high, even at low hydration time. This was expected because in the composition of this cement are found mineralogical compounds with high reactivity towards water.

The presence of reactive alumina lead to a very low improving of the compressive strength is attributed, probably, to the increased of workability and/or to the surface activity of the particles of alumina with positive consequence in the strength structures.

Table 2. Physical and mechanical properties of high alumina cements at 20⁰C

Cement type	Blaine specific surface area (cm ² /g)	Water content for standard consist (%)	Setting time		Compressive strength			
			initial (min)	final (min)	Terms of hydration			
					1 day (MPa)	3 days (MPa)	7 days (MPa)	28 days (MPa)
CA ₂ +CA ₆	3490	28.0	415	1200	2	11	35	75
(CA ₂ +CA ₆)+5% C ₄ A ₃ Š	*	28.0	150	240	3	22	49	80
CA ₂	3210	28.0	320	960	38	59	72	76
CA ₂ +5% C ₄ A ₃ Š	*	28.0	120	150	41	67	81	88
CA + CA ₂ with Al ₂ O ₃ /C	4370	36.0	135	210	75	94	103	107
CA + CA ₂ with Al ₂ O ₃ /C	*	36.0	135	210	76	96	114	115

* It assumes to be the same as the cement of whose composition we try to improve.

The compressive strength values of high alumina cements (Table 3) showed a strong influence to the temperature treatment at which they were exposed.

Table 3. Mechanical properties of high alumina cements after exposure at high temperature

Cement type	Compressive strength (MPa)						
	110°C	600 °C	800 °C	1000 °C	1200 °C	1400 °C	1600 °C
CA ₂ +CA ₆	75	74	71	67	65	121	130
(CA ₂ +CA ₆)+5% C ₄ A ₃ Š	80	70	67	65	62	103	111
CA ₂	76	70	68	64	63	91	98
CA ₂ +5% C ₄ A ₃ Š	87	69	65	60	59	84	90
CA + CA ₂ with molar ratio Al ₂ O ₃ /CaO = 2.5	107	80	65	57	63	100	73
CA + CA ₂ with molar ratio Al ₂ O ₃ /CaO = 4,0	115	86	83	76	80	113	102

All high alumina cements showed a decrease in compressive strength in the temperature range 110°C - (1000°C) 1200°C, due to structural reorganization that occurs in the critical temperature range. Instead in the range 1000°C (1200°C) - 1600°C, the values of compressive strength are improved than those recorded in the critical temperature range, this being due to the formation of ceramic binding between mineralogical

compounds present at high temperature.

The decrease in compressive strength was higher for samples with additive, comparing to the one without additive, explained by the stronger hydration of the samples with additive. In the case on high alumina cement based CA and CA₂ with molar ratio Al₂O₃/CaO = 4.0, the increase of compressive strength was higher than that reported to the strength values of cement without addition of alumina. Those increased values of compressive strength were explained by XRD and SEM.

The XRD helped to identify the mineralogical compounds presented in cement samples exposed to high temperatures, thus explaining the good behavior of the samples. After the exposure at 1600°C representative samples from all cements were exposure at XRD. The characteristic mineralogical components of every cement samples are presented in Table 4.

Table 4. Diffraction lines of specific mineralogical components from high alumina cements after exposure at 1600 °C

Cement type	Calcium alumina			
	CA ₆	CA ₂	CA	A
CA ₂ +CA ₆	+++	+++	+	-
(CA ₂ +CA ₆)+5% C ₄ A ₃ S̄	+++	+++	+	-
CA ₂	-	+++	+	-
CA ₂ +5% C ₄ A ₃ S̄	-	+++	+	-
CA + CA ₂ with molar ratio Al ₂ O ₃ /CaO = 2.5	-	+++	++	-
CA + CA ₂ with molar ratio Al ₂ O ₃ /CaO = 4,0	+	+++	++	-

The XRD of the samples highlight the presence of CA₂ in all high alumina cements, very well crystallized and the presence of CA₆ only in cements based on CA₂ and CA₆ and, at the same time - in a smaller amount in the sample in which the molar ratio Al₂O₃/CaO was increased. This fact is due to the movement of the composition from the CA-CA₂ subsystem to the CA₂-CA₆ subsystem for the cement with increase molar ratio Al₂O₃/CaO. The crystallization of CA₆, although is not very good, was favoured by high temperature and oxide composition of the sample, thus explaining the good mechanical behaviour of this sample at high temperature.

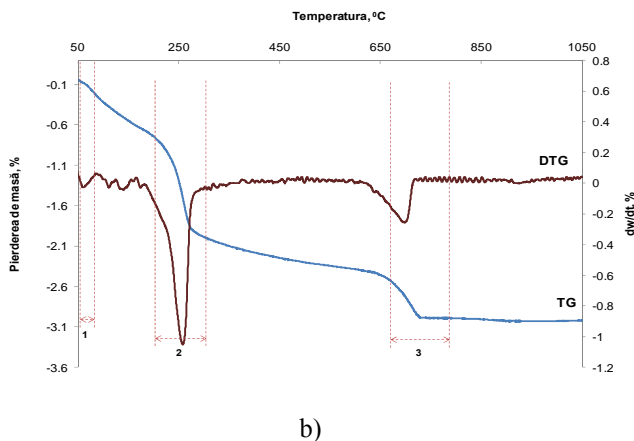
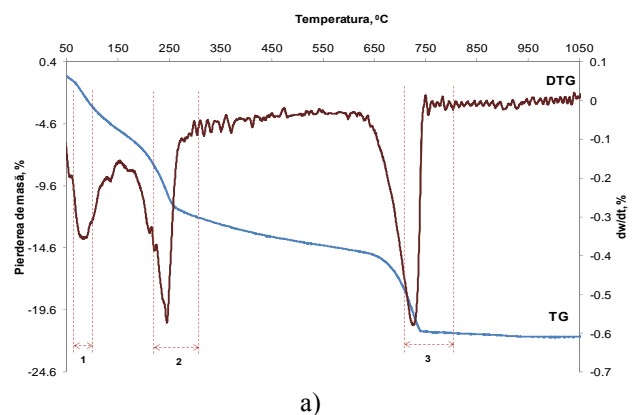
The presence of additive was not detected after heat treatment at 1600°C, due to its low stability at temperatures higher than 1450°C.

The samples under investigation by thermogravimetric analysis are samples of super aluminous cements

hydrated for 3 days. Hydrated cement samples for 3 days were dried before tests achievement for 3 hours in desiccator on calcium chloride, because traces of water that could be in samples to not influence the tests.

Figure 5 presents the results of thermogravimetric investigations up to 1100°C obtained for super aluminous cements. Looking at Figure 5 we can see that with increasing temperature the mass loss is higher. These effects can be highlighted by DTG curve. It can be seen that first effect occurs around 70°C. This mass loss can be attributed to the existence of the water physical bound and of hydrated metastable compounds (C₂AH₈ – in the case of all cements or CAH₁₀ - in the case of ordinary super aluminous cement) transformations in stable hydrated compounds (C₃AH₆).

The intensity of this effect is higher for super aluminous cements based on CA and CA₂ and for the one based on CA₂. This because these cements presents more reactive mineralogical compounds in higher amounts than the one based on CA₂ and CA₆, because in this cement only one compound shows reactivity towards water. This does not mean that it does not present mass lose, but as it intensity is lower.



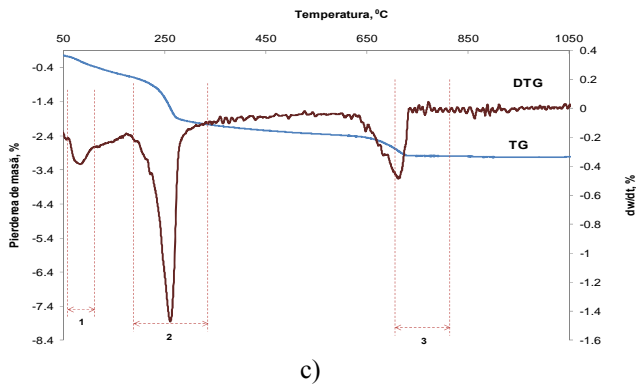
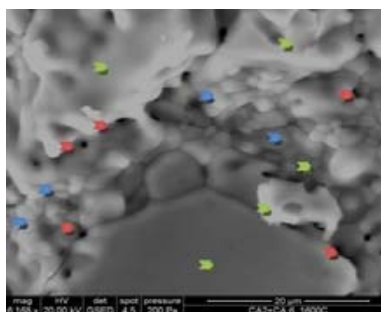


Figure 5. Thermogravimetric analysis of super aluminous cements: a) CA și CA₂; b) CA₂ și CA₆; c) CA₂

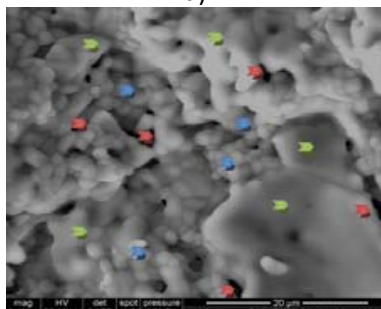
The second area of mass loss occurs in the temperature range 180 - 280°C, where take place the partial dehydration of C₂AH₈, C₃AH₆ and AH₃. Data from the literature indicate that in this temperature range the dehydration of C₃AH₆ goes to C₃AH_{1.5}, of C₂AH₈ to C₂AH₄ and of AH₃ to A [2, 8, 9, 10, 11], thus explained the mass loss and the high peak intensity from the curve DTG.

Regarding the third temperature range in which take place significant mass loss, this is included in the temperature range 600 - 730°C. This temperature range corresponds to complete dehydration of the hydration products, with the formation of C₁₂A₇ and CA, followed at 1000°C only CA and CA₂ to be meet.

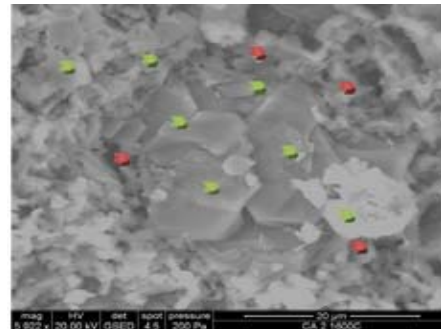
In Figure 6 are presented the electron micrographs of the high alumina cements after the exposure at 1600°C. The SEM performed on samples exposed to 1600°C comes to support both compressive strength values of cement samples and mineralogical compounds identified by XRD.



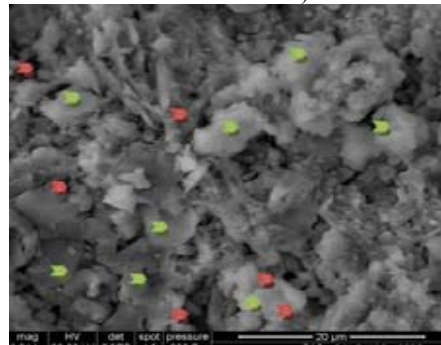
a)



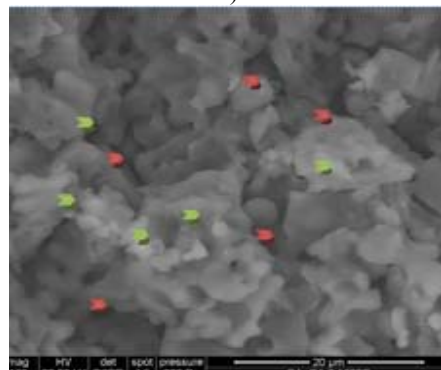
b)



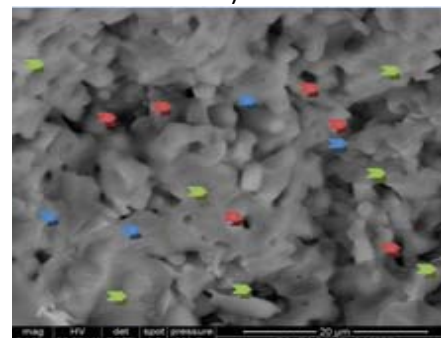
c)



d)



e)



f)

Legend: CA₂ crystals; CA₆ crystals; Pores

Figure 6. Electron micrographs of the high alumina cements based on: a) CA₂ and CA₆, without additive; b) CA₂ and CA₆, with 5% C₄A₃S additive; c) CA₂, without additive; d) CA₂, with 5% C₄A₃S additive; e) CA and CA₂ with molar ratio Al₂O₃/CaO = 2.5; f) CA and CA₂ with molar ratio Al₂O₃/CaO = 4.0 after the exposure at 1600°C

It can be seen from Figure 6 that high alumina cement samples without additives shows better defined crystals ranging from 1 μm up to 40 μm for the sample base on

CA₂ and CA₆ [Fig. 6 a)], and from 1 μm up to 20 μm for the sample base on CA₂ [Fig. 1 c)], lower porosity than the samples without additives [Fig. 6 b) and c)], this is due to the fact that this additive is not stable at high temperatures, although its presence at normal temperature (during hydration) was favorable.

The electronic micrograph of high alumina cement with molar ratio Al₂O₃/CaO = 4.0 [Fig. 6 f)] revealed a structure composed of small crystals, between 1 μm and 10 μm belonging to CA, CA₂ and maybe CA₆, well defined, forming a well-densified ceramic body.

Regarding the porosity of the sample, it is composed of a number of pores not very high and pore sizes go up to max. 5 μm. Compared with the structure of high alumina cement with molar ratio Al₂O₃/CaO = 2.5 without alumina [Fig. 6 e)], the structure of high alumina cement with molar ratio Al₂O₃/CaO = 4.0 is more compact and well crystallized due to mineralogical composition.

5. CONCLUSIONS

After the different investigations made on the high alumina cement based on high refractory calcium aluminous compounds we draw the following conclusions:

1. Using a hydration activator lead to improved structural and mechanical behavior of high alumina cements based on highly refractory mineralogical compounds at room temperature while maintaining the good behavior at high temperature of the base cements.

2. The high alumina cements based on high refractory mineralogical compounds such as CA₂ and CA₆ presented a very good structural and mechanical behavior after heat treatment at high temperature, if the normal hydration has been activated.

3. Once the molar ratio Al₂O₃/CaO of the high alumina cement was increase the value of compressive strength after the exposure at high temperature were increased because in the sample was found CA₂ and CA₆, formed by recrystallization.

4. The presence of C₄A₃S̄ was favorable at normal temperature, especially for the cements with low interaction with water, thus obtaining an increase of mechanical strengths. After heat treatment at 1600°C, due to its low stability was not detected anymore.

REFERENCES:

- [1] Angelescu, N., Ionita C. - Calcium hexa aluminate as possible mineralogical compound in alumina cements. Metallurgy and New Materials Researches, Februarys 2011, vol. 19, Special BRAMAT No, p. 11-13.
- [2] Teoreanu, I., Ciocea, N. - Lianți, mase și betoane refractare. Ed. Tehnica, Bucharest, 1977.
- [3] Munteanu, M., Ionescu, A., Ropota, I., Munteanu, O. - Hydration of calcium aluminates in the presence of yeelenite, Calcium Aluminate Cements. Proceeding of the Centenary Conference, Breperss, 2008, p. 429-434.
- [4] Ionita C. - Sisteme liante complexe folosite la obținerea betoanelor de înaltă performanță în contextul utilizării

cimentului cu compuși mineralogici înalt refractari. Doctorate Thesis, Valahia University Targoviste, 2013.

- [5] Hewlett, P. - Lea's Chemistry of Cement and Concrete, 4th edition. Publisher: Elsevier Science & Technology Books, 2002, p 1057.
- [6] Ionita, C., Angelescu, N., Muntean, M. - The influence of mineralogical composition of high alumina cement on its physical - mechanical properties. Proceedings of the Centenary Conference, Avignon, France, 19 May – 21 May 2014. HIS BRE Press, 2014.
- [7] Ionita C., Angelescu, N., Amziane, S. – Characterization of super aluminous cements using thermogravimetry analysis and X-ray diffraction. Metalurgia International vol 17 (2012), no. 6, pp. 174-177.
- [8] Das, S. K., Dasgopdar, P.K. - Dehydration kinetics of hydrated calcium dialuminate. Thermochemica Acta no 293, Elsevier Scientific Publishing Company, pp 125-128, 1997.
- [9] Taylor, H. F. W. - Cement chemistry, 2nd edition. Publisher: Thomas Telford Publishing, 1997.
- [10] Ionita, C., Angelescu, N., Abdelgader, H. S., Bratu, V., Stanciu, D., Ion, I. - The influence of hydration on the mechanical strength of the high aluminous cement. Proceedings of The International Conference on Advances in Cement and Concrete in Africa, ACCTA 2013, Johannesburg, South Africa, 2013, pp. 961 – 968.
- [11] Kumar, S., Bandopadhyay, A., Alex, T.C., Kumar, R. - Influence of mechanical activation on the synthesis and hydraulic activity of calcium dialuminate. Ceramics International, no 32, pp. 555–560, 2006.

THE MATHEMATICAL MODEL APPLIED TO SOLIDIFY AND SEGREGATION OF LEDEBURITE TOOL STEEL INGOTS

Vasile BRATU, Ileana Nicoleta POPESCU

Valahia University of Targoviste, Faculty of Materials Engineering and Mechanics,
13 Aleea Sinaia Street, Targoviste, Romania

E-mail: v_bratu22@yahoo.com

Abstract. In order to determine the optimum geometry of the ingot mold format (the format of ingot mold with a diameter per height ratio $H/D < 3$ and the conicity of minimum 7%) was analyzed by mathematical modeling of solidification and segregation of the carbon and sulfur in it.

It was considered 205Cr115 steel type (according with , STAS 3611 - Romanian standardization) and known also as X210Cr12 steel type (according with European standard). It has been considered an element of volume of coordinates x, y, z in the solidifying ingot and have made the following assumptions: (i) the equilibrium distribution ratio K , is applied to the solid-liquid interface; (ii) solid diffusion is negligible during solidification; and (iii) the solid density is constant during solidification. In carrying out the simulation of segregation mechanisms are resolved heat transfer equation, that simulating the solidification process and are solved the interdendritic fluid equation of motion.

Keywords: X210Cr12, solidification mathematical model, ledeburite tool steel ingots

1. INTRODUCTION

Tool steels quality is evaluated by how the tool behaves under conditions of use. Tool steel should have those technical characteristics that assure maximum reliability, even if their production causes some difficulties in manufacturing technology. The main characteristics that determine the behavior of the service tool are hardness and toughness, both related to the chemical composition, size and distribution of carbides, depends also of grain size and degree of purity [1-4]. The steel purity is assured by the way of elaboration process (oxidation, deoxidation), steel evacuation and casting of steel. The quality of the carbides is based, first of all, on the chemical composition of steel and of a number of technological factors, such as: (a) the conditions of casting and solidification, (b) plastic deformation and (c) heat treatment, which more or less influence the homogeneity. In the segregation process it has an important role the physico-chemical characteristics of policomponent system (the alloy tool steel). Each steel grade having its own solidification characteristics and even in the same type of steel are differences depending on the carbon content [1, 2].

Thus, at the solidification process appear at a time the α , H, phases, carbides, the areas of occurrence of each phase and their coexistence with the liquid being very different.

Taking into account the starting pouring temperature and the early change starting solidification temperature (separation of carbides and the extent of different temperature areas on the different phases) resulting

importance of respecting the conditions of casting, for the quality of carbides: the temperature and speed casting, the characteristics of the mold, the cooling conditions.

It is known that the casting temperature is increasing influence on the re-melting and, consequently, the removal, and the degree of segregation and the size of the primary carbides. In the following table (Table 1) shows the dimensional characteristics of steel ingot mould used for casting of ledeburite tool steel ingots:

Table 1. Dimensional characteristics of ingot mould

Steel Grade	Product Diameter	Ingot Type	Dimensional characteristics of ingot mould			
			Side [mm]	Height [mm]	H/D	Wall Thickness [mm]
Ledeburite tool steel	< 80 mm	254 mm 30 kg	310/ 225	710	2.52	65/72
	< 150 mm	356 mm 1050 kg	425/ 314	1258	3.40	90/96

The size of the ingot has a great influence on the size of the network of carbides, in particular with respect to its homogeneity of the ingot section, as shown in Fig. 1.

Studies on ingot less than 300 kg, used in ledeburite steel casting have shown that the best results on the ingot axial capacity is obtained when using ingots with $H/D < 3$ and conicity less than 7% [1].

Ingot mold wall thickness is also a much-discussed parameter. Reducing mold wall thickness and degree of homogeneity favorable influence the structural homogeneity degree due segregation carbides.

An ingot mold with thick walls provide intense cooling during the crust formation the ingot, after that, begins to constitute an impediment to the heat flow outward, reducing cooling intensity.

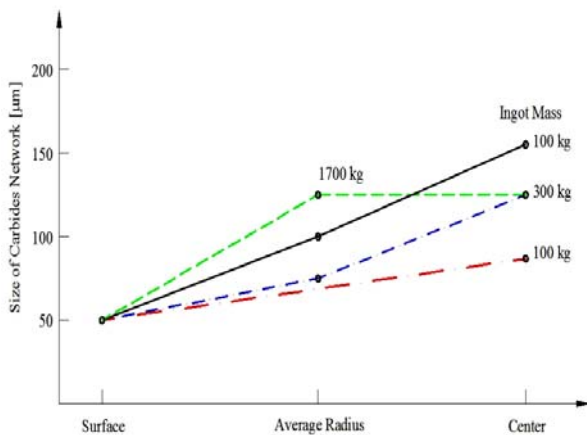


Figure 1. The size of the network of carbides, in correlation with ingot section

2. MATHEMATICAL MODEL FOR SOLIDIFICATION AND SEGREGATION OF SOLID STEEL INGOTS

Improvement of the existing ingot formats in operating process, is a part of the general issue on reducing material consumption. In literature was developed different models of solidification of metals [5-9] taking into account the heat exchange by conduction and convection heat exchange, but with insufficient evaluation of the influence of convective heat transfer on the evolution of the solidification front.

In order to determine the optimum geometry of the ingot mold consisting of G10 m type, was analyzed, by mathematical modeling, the solidification process and the carbon and sulfur segregation, and also, in parallel, the same calculations were performed for the format G10 used in Electric Steelworks Department of the former Special Steel Plant (COS Târgoviște Company). It was considered the 205Cr115 steel grade.

The mechanism of solidification and segregation of solid steel ingot can be treated by modeling hydrodynamic behavior of the interdendritic fluid due (i) to shrinkage forces occurring during solidification and due (ii) the forces of gravity caused by differences in density of the fluid.

Liquid bicomponent phases region is considered as a porous medium, where the porosity coefficient and the

pores' size depends on the size of the solidification pits fraction and solid fraction. The liquid bicomponent phases region is changing during solidification.

We consider a volume element of x, y, z coordinations in the solidifying ingot and the following simplifying assumptions are made:

- Equilibrium distribution ratio K is applied to solid-liquid interface;
- Solid diffusion is negligible during solidification;
- Density of the solid is constant during solidification.

Under these conditions, the equation describing the local redistribution of the solution is:

$$\frac{\partial g_L}{\partial C_L} = \frac{1-\beta}{1-K} \cdot \left(1 + \frac{\bar{v} \cdot v \cdot T}{\varepsilon} \right) \cdot \frac{g_L}{C_L} \quad (1)$$

where: $\frac{\partial g_L}{\partial C_L}$ is the differential variation of the volume fraction of liquid g_L with the concentration in the liquid C_L , considered relative to the volume element;

β is the solidification shrinkage coefficient that is considered as a function of temperature;

K is the equilibrium distribution coefficient which is a function of temperature;

ε is change rate of the temperature in the volume element (degrees ° C / S)

\bar{V} is the interdendritic fluid velocity in comparison to the solid (cm / s).

Through the integration of equation (1), and setting boundary conditions C_0 and C_L is obtained:

$$C_L = C_0 \cdot g_L^{-1} / \left(\frac{1-\beta}{1-K} \right) \cdot \left(1 + \frac{\bar{v} \cdot v \cdot T}{\varepsilon} \right) \quad (2)$$

Where C_0 is the initial concentration

So, the distribution of the liquid phase concentration values in ingot it depends, at any time, of time.

In the course of the simulation of the mechanism of segregation are solved the following equation:

A. The heat transfer equation, is the equation that simulating the solidification process:

$$\frac{\partial T}{\partial \tau} = - \frac{\lambda}{C_p \cdot \rho} \cdot \bar{v} \cdot v \cdot T \quad (3)$$

where: T - temperature, ° C;

τ - time, s;

λ - thermal conductivity, cal / cm-s- ° C;

C_p Specific heat; cal / g- ° C;

ρ -density, g / cm³

B. The equation of the liquid fraction is:

$$f_L = \frac{g_L \cdot (1-\beta)}{1-\beta \cdot g_L} \quad (4)$$

where G_L is the liquid fraction by weight.

C. The equation of motion of the interdendritic fluid:

$$v = -\frac{K}{\mu \cdot g_L} (\bar{v}_p + g_L \cdot \bar{g}_n) \quad (5)$$

where:

μ - interdendritic viscosity; $\mu = f(T) \text{ g/cm}^{-s}$;
 K - fluid permeability of the structure considered as
 $K = f(g_L) \text{ cm}^2$;

\bar{g}_n - The acceleration vector of gravity, cm/s^2 ;

\bar{V}_p - pressure, kgf/cm^2 .

Solving the equation of heat transfer and interdendritic fluid movement is done using the finite element method.

This method analyzes the studied field in the following three steps:

- dividing the field into a finite number of small discrete elements and interrelated by a finite number of nodes;
- analysis of the properties of each element to suit the phasic area in which it replaces; calculate the "stiffness" of each element using the principle of minimizing the potential energy of the system;
- analysis of the distribution elements and reassembly of the physical variables of the contour determined by the condition data (specified).

By solving the heat transfer equation is determined, at each time, until solidification:

- gradient temperature distribution in the ingot;
- distribution of the temperature change rates in ingot

Knowing the temperature distribution in the ingot, we can calculate the values of physical parameters of mathematical model: the thermal conductivity; the density; viscosity; permeability; electrical constants.

Thermodynamic and thermophysical quantities that are dependent on temperature, to solidification steel can be determined using the relationship [8-12]:

$$\rho_{(T)} = 7840 \frac{1}{1 + \alpha(T) \cdot (T - T_0)} \quad (6)$$

where:

$$\alpha_{(T)} \cdot 10^6 = 10,7 + 0,6 \left(\frac{T - 273,16}{100} \right) - \frac{2,9}{\text{ch} \left[0,76 \left(\frac{T - T_0}{100} \right)^2 \right]}$$

$$T_0 = 1178,16 \text{K}$$

For $T < 1041 \text{K}$, $C_p(T)$ is calculated with the equation

$$C_p(T) = 1000 \left[0,4814 + 0,1997 \left(\frac{T - 273,16}{100} \right) + 0,812 \cdot e^{-0,0099(1041-T)} \right] \quad (7)$$

For $T > 1041 \text{K}$, $C_p(T)$ is calculated with the equation:

$$C_p(T) = 1000 \left[0,4814 + 0,1997 \left(\frac{T - 273,16}{100} \right) + 0,812 \cdot e^{-0,0261(1041-T)} \right] \quad (8)$$

For $T \leq 1173 \text{K}$, $\lambda(T)$ is calculated by the formula::

$$\lambda(T) = 26,74 + \frac{(\lambda_0 - 26,74)(1173,16 - T)}{1173} \quad (9)$$

where:

$$\lambda_0 = 74,42 - 16,28[\%C] - 34,88[\%Si] - 23,36[\%Mn] \quad (10)$$

For $T > 1173 \text{K}$,

$\lambda(T)$ is calculated by the formula:

$$\lambda(T) = 0,01164 \cdot T + 13,08628 \quad (11)$$

For the calculation of thermophysical quantities that vary with temperature and are input data, you can use the following relations:

$$C_p = (23,57 + 9,75T \cdot 10^{-3}) 4,826 \quad (12)$$

$$\rho_l = [10,678 - 13,17 \cdot 10^{-4}(T_l - T_s)] \cdot 10^3 \quad (13)$$

where :

- C_p is the heat capacity ;
- ρ_l is the density of the liquid;
- ρ_s is the solid density;
- λ the thermal diffusivity of the alloy in solid form;
- λ_0 the initial thermal conductivity;
- T_l the liquid alloy temperature;
- T_s the temperature of solidification;

By solving the motion equation of interdendritic fluid is determined, in every time, the biphasic zone:

- Distribution of the fluid movements in the biphasic zone on the all three directions;
- Stress distribution in the biphasic dendritic structure;
- Interdendritic fluid velocity distribution.

We take into account two formats of the ingot moulds: G10 used in COS – Targoviste SA (Electric Steelworks Department of the former Special Steel Plant, COS Târgoviste Company) and G10M with the following parameters and features:

Table 2. Ingot format moulds used at COST S.A.

G10M Ingot format mold	Mass [Kg]	Dimensions [mm]				
		D_{sup}	D_{inf}	D_{med}	H_{mas}	H_{tot}
	980	420	320	370	200	1310
	Mass [Kg]	Volume [dm ³]			Conicity [%]	
		V_1	V_2	V_{mass}		
	980	123.5	19.0	13.3	9.9	

where

D_{sup} - the upper diameter of ingot mould;

D_{inf} - the lower diameter of ingot mould;

D_{med} - average diameter of ingot mould;

H_{mas} - height of the ingot crop end (shrinking head);

H_{tot} - total height (the ingot crop end /shrinking head+ ingot mould);

V_1 - volume of ingot mould;

V_2 - volume of the ingot crop end (shrinking head).

3. CONCLUSIONS

The test results using the mathematical model are following:

(i) the axial biphasic area that solidifies the last in ingot and where the solidification shrinkage gap('pipe') in ingot is formed, it is positioned all in the ingot crop end (shrinking head) for the 205Cr115 steel type;

(ii) The maximum amount of carbon segregation, express by the maximum segregation coefficient, it's less for the G10 format in comparison with G10 m format.

(iii) the maximum content of carbon in the area with maximum segregation match in the required field of composition for this steel grade.

In conclusion, the format ingot proposed is G10m that was dimensioned according with indications from the literature, that ensures appropriate quality of the ingots. The obtained segregation value of C is in less than similar value of ingot G10 type.

REFERENCES

Journals:

- [2] B.Yordanov, Heat Treatment of Tool Steel X210CR12 After Modification With Nanodispersed Si3N4 , Journal of the University of Chemical Technology and Metallurgy, 46, 4 (2011), 423-426.
- [3] FV Anghelina, V Bratu, IN Popescu, Estimating the stacking faults of high alloyed steels, The Scientific Bulletin of Valahia University 8(11) (2013), 7-11.
- [4] I.N. Popescu, D Bojin, I. Carceanu, G. Novac, F.V. Anghelina, Morphological And Structural Aspects Using Electronic Microscopy And Image Analysis Of Iron Powders Obtained By Water Atomization Process, Journal of Science and Arts, 1(12)(2010) 125-134.
- [5] V. Bratu, I.N Popescu, E.V. Stoian, , D.N Ungureanu, C.O. Rusanescu, L.G. Toma, A-C Voicu, Casting and Homogenization of AlCu33Mg1.5Mn Alloy for Aircraft Industry. Advanced Materials Research, 1128 (2015), 44-50.
- [6] V. Bratu, IN Popescu, FV Anghelina, M-C Enescu , , D.N Ungureanu, Determination Of Solidification Front' Position by Using Tungsten at Continuous Casting of Lead-Based Non-Ferrous Semi-Products Metalurgia International 16(4) (2011) , 81-84 .
- [7] A. Kemna, Better steel quality thanks to the solidification model, Metals & Mining International News, May 2001.
- [8] V. Bratu, C Mortici, C Oros, N Ghiban , Mathematical model of solidification process in steel continuous casting taking into account the convective heat transfer at liquid-solid interface, Computational Materials Science 94 (2014), 2-7.
- [9] Ya Meng and Brian G. Thomas, Heat Transfer and Solidification Model of Continuous Slab Casting : Con1D, Metallurgical and Materials Transactions B, 34B (5) (2003), 685-705.

Books:

- [1] V.A. Efimov, Casting and Crystallization of Steels, Technical Publishing House, Bucharest, 1980.
- [10] Adrian Bejan, Convection Heat Transfer, John Wiley & Sons, 2013.
- [11] F.V. Anghelina, V. Bratu, I. N. Popescu, Transfer de masă si căldură. Indrumar de laborator/ Heat & Mass Transfer Laboratory Manual , Valahia University Press ISBN 978-606-603-129 -5, 2014
- [12] A. Leca, I. Prisecaru, Thermophysical and Thermodynamic Properties, Technical Publishing House, Bucharest, 1994.

ON THE ASSESSMENT MODE OF SOME SAFETY COEFFICIENTS USING BREAKING POLYNOMIAL CRITERIA

Radu IATAN¹, Pavel FLORESCU¹, Carmen POPA², Gheorghița TOMESCU³

¹University POLITEHNICA of Bucharest; ²University VALAHIA of Târgoviște;

³S.C. UPET S.A. Târgoviște

E-mail: r_iatan@yahoo.com

Abstract: Starting of the characteristic expressions of some breaking polynomial criteria, known and used in practice, it is highlighted how to assess the safety coefficients used in some practical cases. It is obvious that the decision belongs to the user given the experience in the adequate technical domain. In this regard it must not neglect the fact in that the breakage is produced most often in unpredictable moments, conditioned by multiple factors, dependent on material, on manufacturing technologies of finished products, respective the operating conditions.

Keywords: Safety coefficients, breaking criteria

1. INTRODUCTION

The industrial practice has shown many times that some deterioration of the mechanical equipments, in general, and those under pressure, from the process industries, in particular, occur in unwanted moments, sometimes becoming real material and human disasters. No matter how evolved the theoretical knowledge and the experimental procedures, there are still mysteries in many practical cases. It is necessary, therefore, to capitalize the obtained results in practical concretizations, on materials tested under operational conditions, obviously more aggressive than the common. The presence of some safety coefficients (or, otherwise expressed, like uncertainty in some industrial states) are useful both for the experimental models and the more for the methods of design, implementation and concrete use.

The need for these measures is the more important for the anisotropic materials, such as composites, but also for metallic materials much better known in response in usual conditions.

2. Polynomial/tensor criteria

The mathematical expression of these types of criteria tries to overcome the shortcomings of other quadratic criteria, which do not distinguish the stretching and compression solicitations.

According to [1-3], **Gol'denblat I. I. și Kopnov V. A.** (see the paper published in *Mehanika Polimerov*, vol. 1, 1965, p. 70-78, for composite of plastic material armed

with fiberglass) proposed the first polynomial criterion, written as a general form:

($i, j, k = 1, 2, \dots, 6$):

$$f(\sigma_{ij}) = \sum_{i=1}^6 (F_i \cdot \sigma_i)^\alpha + \sum_{j=1}^6 \sum_{i=1}^6 (F_{ij} \cdot \sigma_i \cdot \sigma_j)^\beta + \sum_{i=1}^6 \sum_{j=1}^6 \sum_{k=1}^6 (F_{ijk} \cdot \sigma_i \cdot \sigma_j \cdot \sigma_k)^\gamma + \dots \quad (1)$$

where the $\alpha, \beta, \gamma, \dots$ exponents are experimentally determined values (constants of material).

A simpler expression (with $\alpha = \beta = \gamma = 1, 0$), retaining only the first three terms of the (1) equality, according to the papers [4 - 6], is presented under the form (*Tennyson R. C* - [7]):

$$f(\sigma_{ij}) = \sum_{i=1}^6 F_i \cdot \sigma_i + \sum_{j=1}^6 \sum_{i=1}^6 F_{ij} \cdot \sigma_i \cdot \sigma_j + \sum_{i=1}^6 \sum_{j=1}^6 \sum_{k=1}^6 F_{ijk} \cdot \sigma_i \cdot \sigma_j \cdot \sigma_k, \quad (2)$$

with $i, j, k = 1, 2, \dots, 6$.

Usually the influence of the F_{ijk} size, compared to the other terms is neglected, so that the equality which is turned account for practical applications is presented under the form [2, 3, 5, 8, 9, 10]:

$$f(\sigma_{ij}) = \sum_{i=1}^6 F_i \cdot \sigma_i + \sum_{j=1}^6 \sum_{i=1}^6 F_{ij} \cdot \sigma_i \cdot \sigma_j, \quad (3)$$

considering the notations: $\sigma_1, \sigma_2, \sigma_3$ – normal stresses, respectively:

$$\sigma_4 = \tau_{23}; \sigma_5 = \tau_{31}; \sigma_6 = \tau_{12}.$$

The breaking corresponds to the $f(\sigma_{ij}) > 1$ condition [3], while the operating safety is ensured if $f(\sigma_{ij}) \leq 1$.

It is allowed that $F_4 = F_5 = F_6 = 0$ and $F_{14} = F_{15} = F_{16} = F_{24} = F_{25} = F_{26} = F_{34} = F_{35} = F_{36} = F_{45} = F_{56} = F_{64} = 0$,

like simplifications resulting from the fact that in the main axis system of the material, the shear resistance is independent of sign. However, it is considered that the F_i and F_{ij} factors are symmetrical tensors [8].

For an **orthotropic material** the (3) equality is converted to [5, 6, 8, 9, 11]:

$$\begin{aligned} f(\sigma_{ij}) = & F_1 \cdot \sigma_1 + F_2 \cdot \sigma_2 + F_3 \cdot \sigma_3 + F_{11} \cdot \sigma_1^2 + \\ & + F_{22} \cdot \sigma_2^2 + F_{33} \cdot \sigma_3^2 + F_{44} \cdot \sigma_4^2 + F_{55} \cdot \sigma_5^2 + \\ & + F_{66} \cdot \sigma_6^2 + 2 \cdot F_{12} \cdot \sigma_1 \cdot \sigma_2 + 2 \cdot F_{13} \cdot \sigma_1 \cdot \sigma_3 + \\ & + 2 \cdot F_{23} \cdot \sigma_2 \cdot \sigma_3. \end{aligned} \quad (4)$$

The F_i, F_{ij} ($i, j = 1, 2, \dots, 6$) sizes can be determined by the stresses at limit/breaking, through **unidirectional tests**.

For the **plane state of stresses** ($\sigma_3 = \sigma_4 = \sigma_5 = 0$), the (3) equality becomes [6]:

$$\begin{aligned} f(\sigma_{ij}) = & F_1 \cdot \sigma_1 + F_2 \cdot \sigma_2 + F_6 \cdot \sigma_6 + \\ & + F_{11} \cdot \sigma_1^2 + F_{22} \cdot \sigma_2^2 + F_{66} \cdot \sigma_6^2 + \\ & + 2 \cdot F_{12} \cdot \sigma_1 \cdot \sigma_2 + 2 \cdot F_{16} \cdot \sigma_1 \cdot \sigma_6 + \\ & + 2 \cdot F_{26} \cdot \sigma_2 \cdot \sigma_6. \end{aligned} \quad (5)$$

In the [6] paper, for the case of a **transversal isotropic material** - special case of the orthotropy, with the 2 – 3 plan of symmetry, is specified that: $F_2 = F_3$; $F_{12} = F_{13}$; $F_{22} = F_{33}$;

$F_{55} = F_{66}$, and from the shear condition $F_{44} = 2 \cdot (F_{22} - F_{23})$, so that the (4) equality becomes:

$$\begin{aligned} f(\sigma_{ij}) = & F_1 \cdot \sigma_1 + (F_2 + 2 \cdot F_{12} \cdot \sigma_1) \cdot (\sigma_2 + \sigma_3) + \\ & + F_{11} \cdot \sigma_1^2 + F_{22} \cdot (\sigma_2^2 + \sigma_3^2) + 2 \cdot F_{23} \cdot \sigma_2 \cdot \sigma_3 + \\ & + 2 \cdot (F_{22} - F_{23}) \cdot \sigma_4^2 + F_{55} \cdot (\sigma_5^2 + \sigma_6^2) \leq 1. \end{aligned} \quad (6)$$

In the [8, 9] papers the method of determining the F_1, F_{11} factors is shown, considering $\sigma_1 \neq 0$ and all the others stresses $\sigma_i = 0$, in the case of uniaxial solicitation of **stretching** or **compression**. It is deduced that [8]:

$$F_1 \cdot X_T + F_{11} \cdot X_T^2 = 1 \quad \text{- for stretching;}$$

$$F_1 \cdot X_C + F_{11} \cdot X_C^2 = 1 \quad \text{- for compression,}$$

after that the corresponding tensors result [5, 8, 9]:

$$F_1 = 1/X_T + 1/X_C; F_{11} = -1/(X_T \cdot X_C). \quad (7)$$

Similarly, with the others non-null stresses, the expressions are established [5, 8, 9, 12]:

$$\begin{aligned} F_2 = 1/Y_T + 1/Y_C; F_{22} = -1/(Y_T \cdot Y_C); \\ F_3 = 1/Z_T + 1/Z_C; \end{aligned} \quad (8)$$

$$\begin{aligned} F_{33} = -1/(Z_T \cdot Z_C); F_{44} = -1/Q^2; \\ F_{55} = -1/R^2; F_{66} = -1/S^2. \end{aligned} \quad (9)$$

The F_{12}, F_{13} and F_{23} factors, called **interaction constants**, too [8], can be determined from three independent trials, where $\sigma_1 = \sigma_2, \sigma_1 = \sigma_3, \sigma_2 = \sigma_3$, the others stresses being null. If it is accepted that $\sigma_1 = \sigma_2 = \sigma$, the others stresses being null, the tensor criterion predicts the breaking (at limit) when [61]:

$$\begin{aligned} f(\sigma_{ij}) = (F_1 + F_2) \cdot \sigma + \\ + (F_{11} + F_{22} + F_{12}) \cdot \sigma^2 = 1. \end{aligned} \quad (10)$$

In this equality considering successive that the stress values are X_T, X_C, Y_T, Y_C and σ and replacing the F_1, F_2, F_{11}, F_{22} sizes with the (7) and (8) corresponding expressions we reach to [8, 9]:

$$F_{12} = \frac{1}{2} \cdot \left[\frac{1}{\sigma^2} - \frac{1}{\sigma} \cdot \left(\frac{1}{X_T} + \frac{1}{X_C} + \frac{1}{Y_T} + \frac{1}{Y_C} \right) + \frac{1}{X_T \cdot X_C} + \frac{1}{Y_T \cdot Y_C} \right] \quad (11)$$

For a **plane state of stresses**, where $F_{12} = 0$, the (5) equality becomes [8, 12]:

$$f(\sigma_{ij}) = F_1 \cdot \sigma_1 + F_2 \cdot \sigma_2 + F_{11} \cdot \sigma_1^2 + F_{22} \cdot \sigma_2^2 + F_{66} \cdot \sigma_6^2 \quad (12)$$

When $F_{12} \neq 0$, the (5) equality, at limit, takes the form [8]:

$$f(\sigma_{ij}) = F_1 \cdot \sigma_1 + F_2 \cdot \sigma_2 + F_{11} \cdot \sigma_1^2 + F_{22} \cdot \sigma_2^2 + F_{66} \cdot \sigma_6^2 + 2 \cdot F_{12} \cdot \sigma_1 \cdot \sigma_2 = 1, \quad (13)$$

where following some adequate calculations the equality is established [8-10, 13]:

$$F_{12} = -0,5 \cdot \sqrt{F_{11} \cdot F_{22}}, \quad (14)$$

the other sizes being the (7) expressions.



The paper [2] introduces the idea of the presence of a c_s safety coefficient, having the same value both the normal stresses and for the shear stresses, **of mechanical nature**, so that the (13) equality becomes:

$$A_1 \cdot c_s^2 + A_2 \cdot c_s - 1 = 0, \quad (15)$$

where:

$$A_1 = F_{11} \cdot \sigma_1^2 + F_{22} \cdot \sigma_2^2 + F_{66} \cdot \tau_{12}^2 + 2 \cdot F_{12} \cdot \sigma_1 \cdot \sigma_2; \quad (16)$$

$$A_2 = F_1 \cdot \sigma_1 + F_2 \cdot \sigma_2.$$

Solving the (15) equation the adoption of the positive value for the safety coefficient is permitted:

$$c_{s1} = \left(-A_2 + \sqrt{A_2^2 + 4 \cdot A_1} \right) / (2 \cdot A_1), \quad (17)$$

respectively:

$$c_{s2} = \left| \left(-A_2 - \sqrt{A_2^2 + 4 \cdot A_1} \right) / (2 \cdot A_1) \right|. \quad (18)$$

How $|c_{s2}| > |c_{s1}|$, the user will decide which of the two values is accepted.

Developing the previous problem in the case of simultaneous of **the thermal stresses** and/or **stresses caused by humidity**, alongside those mechanical, too, the (15) equality adjusts the form:

$$A_1^* \cdot (c_s^*)^2 + A_2^* \cdot (c_s^*) - 1 = 0, \quad (19)$$

with the corresponding notations:

$$A_1^* = F_{11} \cdot \left[\begin{aligned} &\sigma_1^2 + k_T^2 \cdot \sigma_{1T}^2 + k_H^2 \cdot \sigma_{1H}^2 + \\ &+ 2 \cdot \left(k_T \cdot \sigma_1 \cdot \sigma_{1T} + k_H \cdot \sigma_1 \cdot \sigma_{1H} + \right. \\ &\quad \left. + k_T \cdot k_H \cdot \sigma_{1T} \cdot \sigma_{1H} \right) \end{aligned} \right] +$$

$$+ F_{22} \cdot \left[\begin{aligned} &\sigma_2^2 + k_T^2 \cdot \sigma_{2T}^2 + k_H^2 \cdot \sigma_{2H}^2 + \\ &+ 2 \cdot \left(k_T \cdot \sigma_2 \cdot \sigma_{2T} + k_H \cdot \sigma_2 \cdot \sigma_{2H} + \right. \\ &\quad \left. + k_T \cdot k_H \cdot \sigma_{2T} \cdot \sigma_{2H} \right) \end{aligned} \right] +$$

$$+ F_{66} \cdot \left[\begin{aligned} &\tau_{12}^2 + k_T^2 \cdot \tau_{12T}^2 + k_H^2 \cdot \tau_{12H}^2 + \\ &+ 2 \cdot \left(k_T \cdot \tau_{12} \cdot \tau_{12T} + k_H \cdot \tau_{12} \cdot \tau_{12H} + \right. \\ &\quad \left. + k_T \cdot k_H \cdot \tau_{12T} \cdot \tau_{12H} \right) \end{aligned} \right] +$$

$$+ 2 \cdot F_{12} \cdot \left[\begin{aligned} &\sigma_1 \cdot \sigma_2 + k_T \cdot \sigma_1 \cdot \sigma_{2T} + k_H \cdot \sigma_1 \cdot \sigma_{2H} + \\ &\quad + k_T \cdot \sigma_2 \cdot \sigma_{1T} + k_T^2 \cdot \sigma_{1T} \cdot \sigma_{2T} + \\ &\quad + k_T \cdot k_H \cdot \sigma_{1T} \cdot \sigma_{2T} + k_H \cdot \sigma_2 \cdot \sigma_{1H} + \\ &\quad + k_T \cdot k_H \cdot \sigma_{2T} \cdot \sigma_{1H} + k_T \cdot k_H \cdot \sigma_{1H} \cdot \sigma_{2H} \end{aligned} \right]; \quad (20)$$

$$A_2^* = F_1 \cdot (\sigma_1 + k_T \cdot \sigma_{1T} + k_H \cdot \sigma_{1H}) + F_2 \cdot (\sigma_2 + k_T \cdot \sigma_{2T} + k_H \cdot \sigma_{2H}). \quad (21)$$

The solutions of the (19) equation takes the form:

$$c_{s1}^* = \left| \left(-A_2^* + \sqrt{A_2^{*2} + 4 \cdot A_1^*} \right) / (2 \cdot A_1^*) \right|; \quad (22)$$

$$c_{s2}^* = \left| \left(-A_2^* - \sqrt{A_2^{*2} + 4 \cdot A_1^*} \right) / (2 \cdot A_1^*) \right|. \quad (23)$$

In this case, too, the user will choose the convenient variant of the safety coefficient value.

In the case of the previous expressions the following notations have been used: σ_{1T}, σ_{2T} – thermal normal stresses; σ_{1H}, σ_{2H} – normal stresses due to humidity; τ_{12T}, τ_{12H} – shear stresses due to the thermal effect, respective that developed of the humidity; k_T, k_H – selection factors, with unitary values when the presence of the stresses is accepted, respectively with null values, as appropriate, when the respective effect is not taken into consideration.



Criterion Karkkainen L. R. – Sankar V. B. – Tzeng T. J. (2007)

In the paper [1002], accepting the (8.85)₃ formulation is proceeded to the utilization of the effect of the developed

loads in the transversal sections under the external actions (Karkkainen L. R., Sankar V. B., Tzeng T. J – Journal of Composite Materials, vol. 41, nr. 16, 2007, p. 1917 – 1937), so that the safety condition at the structure deterioration appear (at limit):

$$F_{11} \cdot (N_x + N_y) + F_{11} \cdot (N_x^2 + N_y^2) + F_{12} \cdot N_x \cdot N_y + F_{33} \cdot N_{xy}^2 + F_{44} \cdot (M_x^2 + M_y^2) + F_{66} \cdot M_{xy}^2 = 1, \quad (24)$$

where the N_x , N_y normal unitary forces and the N_{xy} shear unitary force, respective the M_x , M_y unitary bending moments, and the M_{xy} torsion unitary moment are present. As a rule the conditions can be used [14]:

$$F_{11} = 1/F_{1t} - 1/F_{1c}; \quad F_{11} = 1/(F_{1t} \cdot F_{1c});$$

$$F_{33} = 1/F_3^2; \quad (25)$$

$$F_{44} = F_{55} = 1/F_4^2; \quad F_{66} = 1/F_6^2, \quad (26)$$

where F_3 , F_4 , F_6 are determined experimentally loads for solicitations to stretch/compression, shear or bending and torsion [14].



Note: For the composites with carbon or glass fibers, S. Liu K. S., Tsai W.S. (Composite Science and Technology, vol. 58, nr. 7, 1998, p. 1023 – 1032) recommends [14]: $-0,9 \cdot \sqrt{F_{11} \cdot F_{22}} < F_{12} < 0$ or, in general, $F_{12} = -0,5 \cdot \sqrt{F_{11} \cdot F_{22}}$.



The security conditions at deterioration, written compact, have the forms [14]:

$$F_{11} \cdot (N_x + N_y) + F_{11} \cdot (N_x^2 + N_y^2) + F_{12} \cdot N_x \cdot N_y + F_{33} \cdot N_{xy}^2 < 1; \quad (27)$$

$$F_{44} \cdot \max \{ M_x^2, M_y^2 \} + F_{66} \cdot M_{xy}^2 < 1; \quad (28)$$

$$\max \{ N_x / F_x; N_y / F_y \} + \max \{ |M_x|, |M_y| \} / F_4 < 1, \quad (29)$$

where the helpful expressions was used [14]:

$$F_x = \left[1 / (2 \cdot F_{11}) \right] \cdot \left[\begin{array}{l} - (F_{11} + F_{12} \cdot N_x) \pm \\ \sqrt{(F_{11} + F_{12} \cdot N_x)^2 -} \\ - 4 \cdot F_{11} \cdot \left(\begin{array}{l} F_{11} \cdot N_y + \\ + F_{11} \cdot N_y^2 + \\ + F_{33} \cdot N_{xy}^2 - 1 \end{array} \right) \end{array} \right]; \quad (30)$$

$$F_y = \left[1 / (2 \cdot F_{11}) \right] \cdot \left[\begin{array}{l} - (F_{11} + F_{12} \cdot N_x) \pm \\ \sqrt{(F_{11} + F_{12} \cdot N_x)^2 -} \\ - 4 \cdot F_{11} \cdot \left(\begin{array}{l} F_{11} \cdot N_x + \\ + F_{11} \cdot N_x^2 + \\ + F_{33} \cdot N_{xy}^2 - 1 \end{array} \right) \end{array} \right]. \quad (31)$$



Considering a unique safety coefficient both for normal unitary forces and for the shear forces, the (27) expression becomes:

$$A_{1N} \cdot c_{sN}^2 + A_{2N} \cdot c_{sN} - 1 = 0, \quad (32)$$

with the corresponding notations:

$$A_{1N} = F_{11} \cdot (N_x^2 + N_y^2) + F_{12} \cdot N_x \cdot N_y + F_{33} \cdot N_{xy}^2;$$

$$A_{2N} = N_x + N_y, \quad (33)$$

where the effective loads created under the action of the external loads, without producing of some bending unitary or torsion moments are presented. By solving the (32) equation the solutions are obtained:

$$(c_{sN})_1 = \left| \left(-A_{2N} + \sqrt{A_{2N}^2 + 4 \cdot A_{1N}} \right) / (2 \cdot A_{1N}) \right|; \quad (34)$$

$$(c_{sN})_2 = \left| \left(-A_{2N} - \sqrt{A_{2N}^2 + 4 \cdot A_{1N}} \right) / (2 \cdot A_{1N}) \right|, \quad (35)$$

recommending the choice of the convenient value:

$$c_{sN} = \max \{ (c_{sN})_1; (c_{sN})_2 \}. \quad (36)$$

In the case of the accepting and the presence of the rotations of the transversal sections of the plate, with the condition of one safety coefficient, the previous expressions adequately correct:

$$A_{1N}^* = F_{11} \cdot (N_x^2 + N_y^2) + F_{12} \cdot N_x \cdot N_y + F_{33} \cdot N_{xy}^2 + F_{44} \cdot (M_x^2 + M_y^2) + F_{66} \cdot M_{xy}^2; \quad (37)$$

respectively:

$$(c_{sN})_1^* = \left| \left(-A_{2N} + \sqrt{A_{2N}^2 + 4 \cdot A_{1N}^*} \right) / \left(2 \cdot A_{1N}^* \right) \right|; \quad (38)$$

$$(c_{sN})_2^* = \left| \left(-A_{2N} - \sqrt{A_{2N}^2 + 4 \cdot A_{1N}^*} \right) / \left(2 \cdot A_{1N}^* \right) \right|; \quad (39)$$

$$c_{sN}^* = \max \left\{ (c_{sN})_1^*; (c_{sN})_2^* \right\}. \quad (40)$$

CONCLUSIONS

This paper presents the general problem of the breaking polynomial criteria, respective the characteristic mathematical expression, adapted by different authors based on the nature of the tested anisotropic materials and the obtained result by adequate experimental research. Given the used criteria for exemplifying the content of the paper, the authors specify the expressions of some safety coefficient, whose values can be accepted by users. It is recommended, considering an ample bibliography, specific to the domain, direct research for the anisotropic materials, metal or composite, so the concrete practical data enable the certificated decisions.

REFERENCES

- [1]. Tripp E. D., Hemann H. J., Gyekenyesi P. J., A review of failure state of anisotropy models for unidirectional ceramic matrix composites under monotonic loads (34th International Gas Turbine and Aeroengine Congress and exposition sponsored by the American Society of Mechanical Engineers, Toronto, Canada, June 4 – 8, 1989) - https://www.google.ro/search?q=A+review+of+failure+state+of+anisotropy&ie=utf-8&oe=utf-8&gws_rd=cr&ei=a5xNVrz9FMjSU7rCvpAE - accesat la 19.11.15)
- [2]. Daniel M. I., Ishai O., Engineering mechanics of composite materials, Oxford University Press Inc., New York, 1994.
- [3]. Herakovich T. C., Mechanics of fibrous composites, University of Virginia, John Wiley and Sons, Inc., New York, 1998.
- [4]. ***Aerospatiale – Composite stress manual, MTS 006 Iss.B, 1999.
- [5]. Camanho P. P., Failure criteria for fibre – reinforced polymer composites, Departamento de Engenharia Mecânica e Gestão Industrial, Universidade do Porto, Portugal, 2002
- [6]. Christensen M. R., The comparison and evaluation of three fiber composite failure criteria, UCRL – CONF – 209972, February 2005, SEM Annual Conference and Exposition on Experimental and Applied Mechanics, Portland, OR, Unites States, June 7 – 9, 2005
(https://web.fe.up.pt/~stpinho/teaching/feup/y0506/fcriteri_a.pdf - accesat la 02.10.15).
- [7]. ***[http://www.resist.pub.ro/Cursuri_master/SMC/CAP.2.D_OC\(Materiale compozite stratificate și armate cu fibre\)](http://www.resist.pub.ro/Cursuri_master/SMC/CAP.2.D_OC(Materiale_compozite_stratificate_si_armate_cu_fibre)) (accesat la 17.12.13); http://www.resist.pub.ro/Cursuri_master/SMC/CAP.3.DO_C - accesat la 06.02.15.
- [8]. Alămoreanu Elena, Conastantinescu D. M. , Proiectarea plăcilor compozite laminate, Editura Academiei Române, București, 2005.
- [9]. ***Criteri di resistenza per materiali compositi con rinforzo a fibre continue, Politecnico di Milano
(http://www.aero.polimi.it/~sala/.../Modalita_Rottura_e_Criteri_Resistenza.pdf - accesat la 12.02.15);
Criteri di rottura per materiali ortotropi ([http://www.ingaero.uniroma1.it/attachments/647_Criteri di rottura per materiali compositi.pdf](http://www.ingaero.uniroma1.it/attachments/647_Criteri_di_rottura_per_materiali_compositi.pdf) - accesat la 28.02.15.
- [10]. Aicher S., Klöck W., Linear versus quadratic failure criteria for inplane loaded wood based panels, Otto-Graf-Journal, vol. 12, 2001, p. 187 – 200.
- [11]. Bhavya S., Kumar R. P., Kalam A. S d., Failure analysis of a composite cylinder, IOSR Journal of Mechanical and Civil Engineering (IOSR – JMCE), vol. 3, nr. 3, 2012, p. 1- 7.
- [12]. Lambert D. M., Investigation of design and static behavior of cylindrical tubular composite adhesive joints utilizing the finite element method and stress – based failure theories, Thesis – Utah state University, USA, 2011- <http://digitalcommons.usu.edu/cgi/viewcontent.cgi?article=2044&context=etd> - accesat la 19.08.13).
- [13]. ***Matériaux composites
(materiaux2005.free.fr/MT8MAT/partie3.pdf - accesat la 02.02.15).
- [14]. Mallikarachchi C. Y. M. H., Pellegrino S., Failure criterion for two – ply plain – weave CFRP laminates (preprint submitted to Journal of Composite Materials, 2012).

STUDIES REGARDING THE REACTION METHOD TO WEAR BRAKING MECHANISM

Ivona PETRE, Aurora Anca POINESCU, Adrian CATANGIU, Simona MIHAI

Valahia University of Targoviste, Faculty of Materials Engineering and Mechanics, Department of Materials Engineering, Mechatronics and Robotics
13 Aleea Sinaia Street, Targoviste, Romania

E-mail: poinescua@yahoo.com

Abstract. *With the development of industry have made efforts to improve the performance of braking systems of motor vehicles on public roads. The choice of materials used for coupling brake system involved the development of new materials that meet safety requirements in circulation. During braking of any vehicle, due to the friction created between the disk and pad, temperature rise occurs with negative effects on the process of slowing down the vehicle. Mechanical and thermal stress being put on the brakes is very high. Due to overheating, brake discs and pads may warp or crack, and the material they are made may change its structure. These defects give rise to vibrations and noise during braking, to reduce the coefficient of friction, reduce the effectiveness of the braking mechanism. This paper proposes a study regarding the thermal stresses effects of brake mechanism on the disc material of a car Dacia Logan. It proposes a theoretical model to calculate the temperature that occurred during the operation of the braking system and experimental analysis on the influence of temperature on the brake disc material.*

Keywords: *disc brake, temperature, hardness, operating conditions*

1. INTRODUCTION

The disc brake is a car body that is part of a complex mechanical brake system of a road vehicle. In the case of brake disc from the Logan braking system, subject of this study, braking occurs under the action of the master cylinder which increases the fluid pressure (brake fluid / glycol ether) inside of receptor cylinder. Pressure acting on the piston outward toward pushing to the brake pad and disc. Brake pads are machine parts that come in direct contact with the disc brake and by friction execute the braking (reduced travel speed or immobilization of the vehicle) [1]. Because the disc brake is a crucial component from the viewpoint of safety, materials used in brake system should be stable, abrasion resistant and have properties very good to wear under varying conditions of load, speed, temperature, environmental and durability [2,3,4].

In the literature are presented and analyzed different types of couplers materials [1,4,5,6], used to fabricate braking systems in particular disc brakes. From the literature study resulted that the material with the best properties is gray iron, because they have good tribological performance. It is known that gray cast iron is a material friction with very good quality / price ratio of cost. [7,8,20] The braking system of any road vehicle is a total change mechanism of various types of energy. When any car is moving at a certain speed we say that has a kinetic energy. When any car brakes, pads (or shoes) press on the disc (or drum) convert kinetic energy into thermal energy. Energy balance of the braking

process indicates full conversion of kinetic energy into thermal energy [4]. The thermal stresses in the brake system may have undesirable consequences on:

- Material discs and pads where internal tensions may occur;
- Structural changes on the superheated material;
- Deformation or roundness disk-plate system;
- Premature wear of the disk-plate system.

All this contributes to the deterioration of the vehicle braking qualities. The effects of these changes on the system disk-plate manifests as vibration and noise during braking by reducing the braking coefficient, etc., in other words lead to decrease traffic safety. Due to these undesirable consequences, friction materials used in automotive braking systems, must have wear resistance and high mechanical strength, low thermal conductivity, lubrication components with a role of increasing seizure resistance. Due to the many factors that influence the brake system, the paper proposes a theoretical and experimental approach of this issue.

2. THEORETICAL MODEL TO ESTABLISHING TEMPERATURE OCCURRENCE ON THE FRICTION SURFACE BETWEEN DISK AND PLATE

Interaction method of different parameters in the friction process required to calculate the friction surface temperature of any friction couplings, simplifying assumptions specific to the work analyzed [9-14]:

- For this case subjected to analysis between disk and plate there is no lubricant, and the entire amount of heat generated by the friction between the two elements dissipates;
- The materials constituting the disk and pads are considered isotropic, and a thermal property does not change with temperature;
- Due to the relative movement between the disc and the pads, the temperature at a certain point changes with time;
- Distribution of temperature depends on the force (pressure exerted on the disc), surface topography (processing methods), properties of materials of friction coupling and the environment.

In the transmission process of the flow of strength and in the presence of the sliding movement, the phenomena occurring in the contact real area, so that we can define a temperature "local" (flash) snapshots at local micro areas and an average temperature of nominal surface. [10,11,15,16].

The flow of heat generated in the contact surface roughness peaks are evaluated by relationship:

$$q = \mu p v = \mu \frac{F}{A_n} v \quad (1)$$

- Where: μ - The friction coefficient of the surface;
 p - Pressure exercised on the contact surface;
 v - The relative speed between the surfaces;
 F - The force exercised by the plate;
 A_n - Nominal area of the plate.

In literature, the coefficient of friction between the material of the disc (which is analyzed for cast iron conditions) and pad material (which is ferodo) is estimated at $\alpha = 0,30 \dots 0,45$ [1,17]. In reality, in tribology terms, the coefficient has a constant value. It depends on the speed of movement of the elements, how to process the surface, etc.

Some part (α) of this heat flow diffuses into the disc and the rest ($1 - \alpha$) diffuses into the plate so that the surface heats flux of:

- The disc will be:

$$q_1 = \alpha q \quad (2)$$

- Plate will be:

$$q_2 = (1 - \alpha) q \quad (3)$$

After reaching the state of thermal equilibrium and linearizing first law of heat flow is obtained:

$$\alpha q \cong \lambda_1 \frac{(T_m - T_o)}{l_m} \quad (4)$$

- Where: λ_1 - the thermal conductivity of the disc material;
 T_m - The average temperature of the contact surface:

$$T_m = T_o + \frac{\alpha \mu F v \cdot l_m}{A_n \cdot \lambda_1} \quad (5)$$

- T - The temperature of the disc clamping system ($T_o = 20^\circ C$);
 l_m - Heat diffusion distance towards to the clamping mechanism of the disc.

Evaluation of partition coefficient of heat is based on the Jaeger assumption [16]. This ratio is dependent on the thermal characteristics of the materials and of the sliding speed. The speed is one of the factors that influence the brake, the speed is parameterized so is inserted an invariant Peclet, considered an indicator of operating parameters:

$$Pe = \frac{v \cdot r}{a_1} \quad (6)$$

- Where: v It is the rotation speed of the disc
 r It is the disk radius;
 a_1 Thermal diffusivity of the material disc ($a = \lambda / \rho \cdot c$).

The properties of the material from they are made (the disc and the pads) are shown in Table 1.

Table 1. Materials characteristics of the braking system

Material Property	Measurement units/ symbol	Cast iron	Ferodo
Conductivity	[W/mK] - λ	445	0,08..0,21
Specific heat	[J/kg/K] - c	740	1000..1200
Density	[kg/m ³] - ρ	7640	383

In these conditions, the partition coefficient of heat it is:

$$\alpha = \begin{cases} \frac{\lambda_1}{\lambda_1 + \lambda_2} & Pe \leq 0,1 \\ \frac{1}{1 + 0,795 \frac{\lambda_1}{\lambda_2} \left(\frac{a_1}{a_2}\right)^{1/2} \cdot Pe^{-1/2}} & Pe \geq 5 \end{cases} \quad (7)$$

For intermediate values of parameter Pe ($0,1 < Pe < 5$) it is recommended a linear interpolation.

The average temperature at the friction surface will be: ($0,1 < On < 5$).

$$\bar{T} = \frac{T_m - T_o}{\frac{a_1 H_o}{\lambda_1}} = 4 \alpha \mu \beta \frac{p}{H_o} Pe \quad (8)$$

- Where: β parameter dependent on dimensional characteristics;
 H_o The hardness of the disc material is (100...175HB).

In the figure 1 is represented variation of the average temperature function of working parameter Pe, for the

three areas of the variation ($Pe_1 < 0,1$; $0,1 \leq Pe_2 \leq 5$; $Pe_3 > 5$) at different loads.

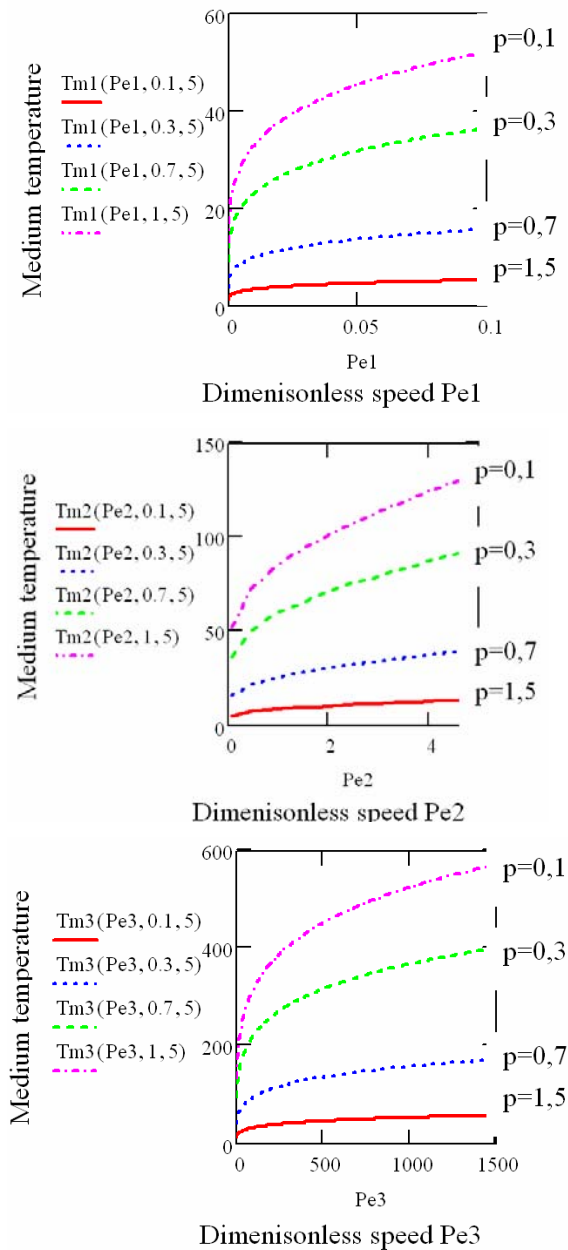


Figure 1. Medium temperature variation depending on the speed dimensionless (Pe_1 , Pe_2 , Pe_3) at different loads

Analyzing evolution of temperature on the friction surface is evident that the temperature increase with its speed and the load (force push the plate on the disc).

3. MATERIALS AND ANALYSIS

Materials used for friction couple in tribological terms are made from cast iron with lamellar graphite Fc150 for the disk and ferodo for the breaking plate. The selected material for structural analysis has the following composition: 3,3-3,5% C, 2,0-2,4% Si, 0,5-0,8% Mn, $<0,2P$ $<0,15P$. Figure 2a, b are given new and worn

brake discs from a Dacia Logan autovehicle, selected for the study.



a) Used discs



b) New disc

Figure 2. Brake discs used for study

3.1. Macrostructural analysis

By macrostructural analysis of old cast iron brake discs recovered, can be seen on the surface defects occurring on the disc. Figure 3 indicates detachment of material and corrosion.



Figure 3. Macrostructural appearance of the used brake disc

In Figure 4 shows a disc irregular worn with blue spots on the lateral surface of the disc, spots appeared after thermal heating. Surface analysis of the used disk was realised at runtime 143 936 Km.

In Figure 5 can be seen bumps on the outer surface that can describe a circle about 204 millimeters. These irregularities occur due to deformation of the material under the pressure it exerts the plate and are visible both on the left and the right disc. These irregularities occur due of material deformations under the pressure it exerts the plate and are visible both on the left and the right of

the disc.



Figure 4. Irregular worn disc with blue spots



Figure 5. Irregular worn-traces on disk left by brake plate

3.2 Temperature monitoring in different sectors on the disk surface during braking

To determine the temperature developed after friction from the disk surface during braking, the car was suspended in the front left and was simulated a braking. This experiment was repeated 4 times under identical conditions. In the Table 2 are presented averages of these measurements. The disk was divided into four diameters with 10mm distances between them and the temperature was measured on the disc surface with a machine called TROTEC - BP25. The device reads the surface temperature of the material using two laser beams, each measuring was announced by an audible alarm and the response time is 150 ms. The measuring range of the device it is between 50°C to 260°C with accuracy between -50°-20°C, measurement error is $\pm 1 / 1,5^\circ\text{C}$, Laser class 11 with a laser power between 630/670 nm.

Table 2. Measured values of the temperature at different diameters on the disc brake

Temp. (oC)	Braking time (min)	D1= 158mm	D2= 178mm	D3= 198mm	D4 = 218mm
T ₀		41,5°C	41,5°C	41,5°C	41,5°C
T ₁	1 min	132°C	146°C	135°C	78,5°C
T ₂	3 min	147°C	154°C	153°C	130°C

This analysis was achieved in the following conditions: air temperature = 38°C, engine speed 2000 rot / min and after braking 1800rot / min, wheel speed = 465rot / min.

From the Table 2 can be seen that with increasing the breaking time grow and surface temperatures of the disk, especially in the contact area with the brake pads

(corresponding to the diameter D2).

3.3. Microstructural analysis

For microscopic examination of a metallographic sample it was necessary previous preparation for the metal surface to be analyzed. Cutting the samples were made by mechanical cutting using a rotating disk-cooled with cooling emulsion based on water and then has been polished, polishing and chemical attack with NITAL (2% nitric acid + ethanol). Microstructural characterization of metallic samples was made with optical microscope MC6. Figure 6 presents the microstructural image of the sample taken from the new brake disc with a 250X magnification and figure 6.b is presented microstructure sample taken from the old disc brake at the same scale of magnification. The used material reveals the presence of a gray cast iron with lamellar graphite, graphite fine slides uniformly distributed in ferrite-pearlite mass base.



a) New brake disk



b) Old break disk

Figure 6. Samples microstructure, 250x

A perlitic basic mass with fine graphite and homogeneous spread shows the 100 time higher wear resistance than a grey iron with ferrite based and graphite heterogeneous spread [18,19,20].

Comparing the two images we can say that no structural changes occurred on used discs therefore temperatures were not so high to cause structural changes in the disk material.

3.4. Rockwell hardness analysis

In order to analyze the hardness of the samples were divided into four diameter with 10 mm distance from each other, and on these diameters was measured the hardness of 6 points. There have been five such measurements and in Table 3 are listed their average values. Hardness tests were made on a Rockwell

hardness tester NAMICON. Indenter was a steel ball, the contact force is 980N (100kg).

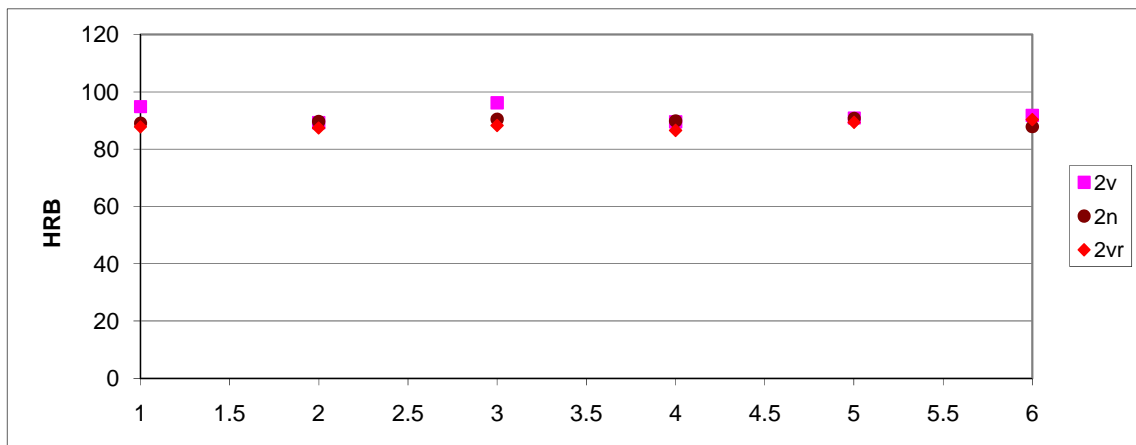
Figures 7.a, b is shown the proper hardness variations for diameters positions 2 and 3 identified as the area of contact between the brake disc and pad. For used disk were performed hardness measurements both sides (2V)

and the reverse (2vr). For the new disc were measured hardness only one- sided (2n).

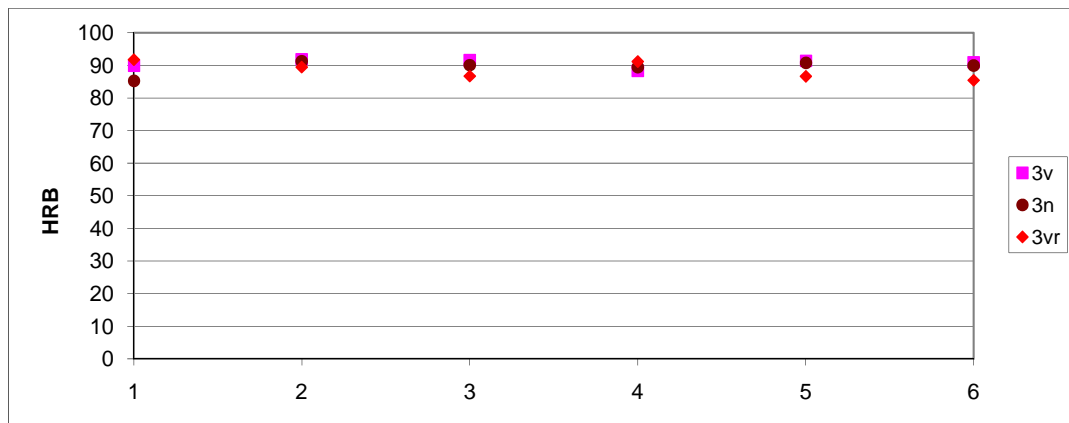
Is found that the harness values not show significant changes. It can be concluded that the temperature during the operation of the braking system does not influence material strength.

Table 3. Rockwell hardness values measured on new and used brake discs

Disk		Diameter	Diameter position					
			a	b	c	d	e	f
Used	Face 1 (2v)	1	81,4	86,8	80,1	88,8	86,3	86,5
		2	94,9	89,2	96,1	89,5	90,9	91,7
		3	89,8	91,9	91,5	88,3	91,4	91
		4	87	86,5	84,1	87	89,5	84,7
	Face 2 (2vr)	1	87	90,2	87,8	88,9	89,8	90,6
		2	87,8	87,4	88,2	86,5	89,3	90,3
		3	91,7	89,4	86,7	91,1	86,6	85,4
		4	91,5	90,6	88,3	85,5	85,7	83,4
New	Face 1 (2n)	1	82,1	88	87,9	89,5	89,1	87,3
		2	89	89,6	90,4	89,8	90,8	87,9
		3	85,2	91,2	90,1	89,4	90,7	89,9
		4	91,9	92,4	90,8	91,9	92,8	93,3



a zone 2 new and old disk



a zone 3 new and old disk

Figure 7. Measured values of hardness

4. CONCLUSIONS

It is noteworthy correlation between the theoretical model for setting the temperature at low and medium speed with experimentally results. Small temperature differences between the theoretical model and experimentally measured values, is because the theoretical model considers that the friction occurs on surfaces in contact with peak asperities. Theoretical temperature under these conditions is greater than the average temperature measured on the surface, bench trial.

In terms of tribological condition, on friction surface because of dimensional differences between nominal and real contact area is considered that:

- For high contact pressures, the real contact area is almost equal with the nominal area and the heat transfer is considered one-dimensional;
- For small contact pressures, the contact is performed on a finite number of rough edge of nominal surface and the heat transfer occurs from the rough edge to the whole body;

The disc brakes has not presented traces of thermal wear demonstrated by corelations of hardness and microscopic analysis. The predominant wear was corrosion accompanied by adhesion and abrasion wear, as confirmed in macro analysis.

By correlating structural analysis (micro and macro) and hardness we can see only changes in surface appearance and not in material hardness. Any differences between the measured temperature and hardness are insignificant, they fall into the error of measurement.

For older car, the wear is more pronounced on the outside diameter of the disk, may be due to plan -parallel misalignment of the plate with the brake disk when is running.

REFERENCES

Journals:

- [1] Maleque MA, Dyuti S, Rahman MM (2010) Material Selection Method in Design of Automotive Brake Disc, Proceedings of the World Congress on Engineering 2010 Vol III, WCE 2010, June 30 - July 2, London, U.K., ISSN: 2078-0958 (Print), ISSN: 2078-0966 (Online),
- [2] Ali Belhocine, Mostefa Bouchetara (2012) Thermal analysis of a solid brake disc, Applied Thermal Engineering 32, DOI: 10.1016/j.applthermaleng.2011.08.029.
- [3] Aleksander Yevtushenko, Michal Kuciej (2010) Temperature and thermal stresses in a pad/disc during braking, Applied Thermal Engineering 30, DOI: 10.1016/j.applthermaleng.2009.09.015.
- [4] Milenković PD, Jovanović S J, Janković AS, Milovanović MD, Vitošević ND, Djordjević MV, Raičević MM (2010) The influence of brake pads thermal conductivity on passenger car brake system efficiency, Thermal Science, Vol. 14, Suppl.: S221-S230.
- [5] Popescu N, Geza E (1999) Contribution to increase of the performance composite materials having friction properties, in Proc. 2-nd National Powder Metallurgy Conference, Metallurgical and Materials Engineering Dept., Ankara: pp. 225-233.
- [6] Omar Maluf, Mauricio Angeloni, Marcelo Tadeu Milan, Dirceu Spinelli, Waldek Wladimir Bose Filho (2007) Development of materials for automotive disc brakes, Minerva, 4(2): 149-158.
- [7] Adam Polak, Janusz Grzybek (2005) The mechanism of changes in the surface layer of grey cast iron automotive brake disc, Materials Research, Vol. 8, No. 4: 475-479.
- [8] Cueva G, Sinatora A, Guesser WL, Tschiptschin AP (2003) Case study, Wear resistance of cast irons used in brake disc rotors, Wear 255: 1256–1260.
- [9] Quinn TFJ, Winer WO (1985) The thermal aspects of oxidational wear, Wear 102: 67-80.
- [10] Tian X, Kennedy FE (1994) Maximum and Average Flash temperatures in sliding contacts, Journal of tribology, 116(1): 167-174.
- [11] Yang J, Winer WO (1991) A comparison between the thermomechanical wear model and some experimental observation, ASME J. Tribol., 113: 262–268.
- [12] Cowann RS, Winer WO (1993) Application of the Thermomechanical wear transition model to layered media, Thin films in tribology, Ed. D.Dowson & al. Elsevier Science Publishers: 631-639.
- [13] Cowan R S, Winer W O (1994) Thermomechanical wear modelling, Tribotest Journal 1: 111-123.
- [14] Archard JF (1958-59) The temperature of rubbing surfaces, Wear 2: 438-455.
- [15] Gecim B, Winer WO (1985) Transient temperatures in the vicinity of an asperity contact, J. Tribol 107(3): 333-341.
- [16] Kennedy jr. FE (1984) Thermal and thermomechanical effects in dry sliding, Wear 100: 453-476.
- [17] Kennedy FE, Balbahadur AC, Lashmore DS (1997) The friction and wear of Cu-based silicon carbide particulate metal matrix composites for brake applications, Wear, vol. 203-204:715-721.
- [18] Collini L, Nicoletto G, Konecna R (2008) Microstructure and mechanical properties of pearlitic grey cast iron, Materials Science and Engineering A 488: 529–539.
- [19] Hecht RL (1999) The Effect of Graphite Flake Morphology on the Thermal Diffusivity of Grey Cast Irons Used for Automotive Brake Discs, Journal of Material Science 34: 4775 – 4781.

Books:

- [20] Ghirsovici I.G. (1952) Turnarea fontei, Editura Tehnică Bucuresti.

THE STABILITY OF LONGITUDINAL MOVEMENT DURING THE TRANSPORTATION OF INDUSTRIAL OVERSIZED EQUIPMENT ON A PLATFORM WITH AN EVEN NUMBER OF AXLES. GENERAL CASE

Radu IATAN¹, Mihai STĂTESCU², Cristina SALCA¹

¹University POLITEHNICA of Bucharest; ²Walter Tosto WTB Bucharest

E-mail: r_iatan@yahoo.com

Abstract. It is known that the transportation of oversized technological equipment raises particular problems, both from the economical and technical point of view. Knowing the loads in the platform-equipment assembly, the intensity and the direction of the wind loads, the condition of roads and the way these act is imperative. The present paper seeks to determine the expression of the loads obtained on a platform with an even number of axles, loaded with a technological equipment and neglecting or not the deformation of the suspensions and tires.

Keywords: Oversized equipment, platform for transportation

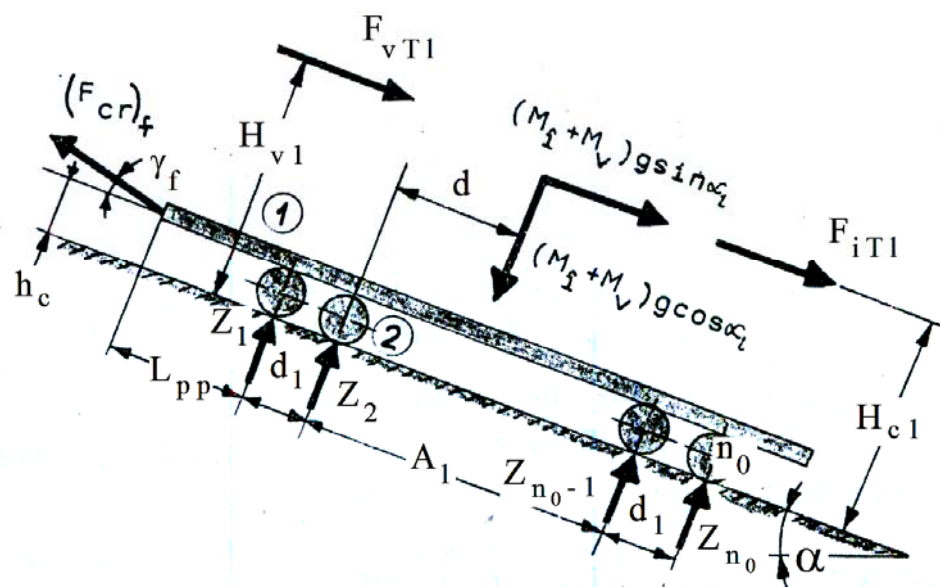


Figure 1. Platform for transportation with even number of axles

1. INTRODUCTION

Concern professionals (designers, manufacturers, transporters and users) in putting into operation and use

of technically safe industrial mechanical equipment in general and those working under pressure in many practical cases with particularly dangerous substances from the chemical point of view and / or mechanical, in particular, it is especially current [1 – 4]. It is known that

a strong influence on the correct operation of industrial equipment is the precision in manufacturing, transportation and installation. Such possible weaknesses, occurred during the route from conception to putting into operation of mechanical structures should be avoided or known and their influence on the state of stress appreciated. It should not be neglected the fact that during transportation might appear the danger of explosion and / or fire with the most dangerous effects [5]. The present paper aims to present some elements concerning the assessment of longitudinal stability when transporting oversize industrial equipment such as to avoid any unexpected damage.

2. HYPOTHESES STUDY

Within the study are taken into consideration some acceptable simplifications, such as [6]:

- The assembly, platform for transportation – load is considered as an one piece system, without showing how to support it and anchorage it;
- The forces occurring during transportation are considered concentrated in their points of application (wind forces are positive if their direction is opposite to the movement of the convoy);
- The road surface is considered without bumps;
- The analyzed assembly is supported on wheels as a static beam with supports (the wheel – suspension assembly) nondeformable or deformable. The platform is supported by constant stiffness along its length.
- The reactions expressions are established at the contact of the tires with the road, using the method of three moments [5 - 9]. In this context, it si taken into consideration both the tracting force and also the resistance force behind the platform (present or not).
- The stability of the movement provides that the overturning bending moment, relative to the center of mass of the system studied, multiplied by a safety factor should be less than the stability calculated on the same point.
- The condition that the lowest normal reaction si positive shall be checked:

$$Z_m = \min \left\{ Z_i \right\}_{i=1, n_0} \geq 0,$$

respectively that the largest to be below the bearing capacity of the axle:

$$Z_M = \max \left\{ Z_i \right\}_{i=1, n_0} \leq Z_{0a},$$

with n_0 is noted the number of the platforms axles.

- Under the conditions specified above it can be calculated the force required to tow the convoy in question.

3. CONDITIONS OF MOVEMENT STABILITY

3. 1. The deformation of the suspension and tires is neglected

The unknown bending moments in the axles (considered as the platform supports) shall be obtained with the equality:

$$\left\{ M_{M(n_0-2)} \right\} = \left[A_{M(n_0-2)} \right]^{-1} \cdot \left\{ T_{TM(n_0-2)} \right\}, \quad (1)$$

where $\left\{ M_{M(n_0-2)} \right\}$ represents the transposed vector of the bending moments M_j ($j = \overline{2, n_0 - 2}$); $\left[A_{M(n_0-2)} \right]$ - the matrix of the influence factors, withc have the expressions:

$$\begin{aligned} a_{11} &= 4 \cdot d_1; \quad a_{12} = d_1; \quad \dots\dots\dots \\ a_{i(j-1)} &= a_{i(j+1)} = d_1; \quad i \neq j; \\ a_{ij} &= 4 \cdot d_1; \quad i \neq j; \quad i = \overline{2, n_0 - 3}; \quad j = \overline{2, n_0 - 3}; \\ &\dots\dots\dots \\ a_{n_0-2, n_0-3} &= d_1; \quad a_{n_0-2, n_0-2} = 4 \cdot d_1; \quad (3) \end{aligned}$$

$\left\{ T_{TM(n_0-2)} \right\}^T = \left\{ b_i \right\}_{i=1, n_0-2}$ is the transposed vector of the free terms, in wherein:

$$\begin{aligned} b_1 &= d_1 \cdot M_f; \quad \dots\dots b_{\frac{n_0}{2}-1} = 6 \cdot A_{\frac{n_0}{2}, \left(\frac{n_0}{2}+1\right) / \left(\frac{n_0}{2}+1\right)}; \\ b_{\frac{n_0}{2}} &= 6 \cdot A_{\frac{n_0}{2}, \left(\frac{n_0}{2}+1\right) / \left(\frac{n_0}{2}\right)}; \quad \dots\dots b_{n_0-2} = d_1 \cdot M_s. \quad (4) \end{aligned}$$

In previous equalities it was considered that the center of mass of the assembly is between the supports $(n_0/2) - 1, n_0/2$, wich is why the sizes are:

$$A_{\frac{n_0}{2}, \left(\frac{n_0}{2}+1\right) / \left(\frac{n_0}{2}\right)} = A_{23/3}^*; \quad A_{\frac{n_0}{2}, \left(\frac{n_0}{2}\right) / \left(\frac{n_0}{2}\right)} = A_{12/3}^*, \quad (5)$$

where it is changed A_1 with d_1 [8].

Takeing into account the expressions of the bending moments of the supports, it results the normal reactions:

$$\begin{aligned} Z_1 &= -k_{crf} \cdot (F_{cr})_f \cdot \sin \gamma_f + (M_2 - M_f) / d_1; \\ Z_2 &= (M_f - 2 \cdot M_2 + M_3) / d_1; \quad \dots\dots\dots \end{aligned}$$

$$Z_i = (M_{i-1} - 2 \cdot M_i + M_{i+1}) / d_1; \quad i = \overline{3, (n_0/2)-1};$$

.....

$$Z_{n_0/2} = (1 - d/d_1) \cdot (M_i + M_v) \cdot g \cdot \cos \alpha_i +$$

$$\begin{aligned}
 &+ \left(M_{n_0/2-1} - 2 \cdot M_{n_0/2} + M_{n_0/2+1} \right) / d_1; \\
 Z_{n_0/2+1} &= (d/d_1) \cdot (M_i + M_v) \cdot g \cdot \cos \alpha_i + \\
 &+ \left(M_{n_0/2} - 2 \cdot M_{n_0/2+1} + M_{n_0/2+2} \right) / d_1; \\
 &\dots\dots\dots \\
 Z_{n_0-1} &= \left(M_{n_0-2} - 2 \cdot M_{n_0-1} + M_s \right) / d_1; \\
 Z_{n_0} &= -k_{crs} \cdot (F_{cr})_s \cdot \sin \gamma_s - (M_s - M_{n_0-1}) / d_1.
 \end{aligned} \tag{6}$$

The condition for the stability of the moving assembly is presented in this case under the form:

$$\begin{aligned}
 c_s \cdot \left[F_{vIT} \cdot (H_{v1} - H_{c1}) + (F_{cr})_f \cdot \left\{ k_{crf} \cdot [L_{pp} + \right. \right. \\
 \left. \left. + \left(\frac{n_0}{2} - 1 \right) \cdot d_1 + d \right] \cdot \sin \gamma_f + (H_{c1} - h_c) \cdot \cos \gamma_f \right\} + \\
 \left. + \sum_{i=1}^{n_0/2} Z_i \cdot [d + (n_0/2 - 1) \cdot d_1] \right] \leq \\
 \leq f \cdot \left[(M_i + M_v) \cdot g \cdot \cos \alpha_i - k_{crf} \cdot (F_{cr})_f \cdot \sin \gamma_f - \right. \\
 \left. - k_{crs} \cdot (F_{cr})_s \cdot \sin \gamma_s \right] + (F_{cr})_s \cdot \left[k_{crs} \cdot (L_{pp} + \right. \\
 \left. + \frac{n_0}{2} \cdot d_1 + d) \cdot \sin \gamma_s + (H_{c1} - h_c) \cdot \cos \gamma_s \right] + \\
 \left. + \sum_{i=(n_0/2)+1}^{n_0} Z_i \cdot [(i - n_0/2) \cdot d_1 - d]. \tag{7}
 \end{aligned}$$

3. 2. The deformation of the suspension and tires is not neglected

The first unknowns of the problem at hand – the bending moments of the supports considered, it is determined also by the equality of the form (1). The non zero expressions of the items of the matrix $[A_{M(n_0-2)}]$ are:

$$\begin{aligned}
 a_{11} &= 4 \cdot d_1 + \frac{6 \cdot E \cdot I}{d_1^2 \cdot k_{ap}^*} \cdot \left(\frac{1}{n_{p1}} + \frac{4}{n_{p2}} + \frac{1}{n_{p3}} \right); \\
 a_{12} &= d_1 - \frac{12 \cdot E \cdot I}{d_1^2 \cdot k_{ap}^*} \cdot \left(\frac{1}{n_{p2}} + \frac{1}{n_{p3}} \right); \\
 a_{13} &= d_1 - \frac{6 \cdot E \cdot I}{n_{p3} \cdot d_1^2 \cdot k_{ap}^*}; \\
 &\dots\dots\dots \\
 a_{i(j-2)} &= \frac{6 \cdot E \cdot I}{n_{pi} \cdot d_1^2 \cdot k_{ap}^*}; \quad i \neq j;
 \end{aligned}$$

$$\begin{aligned}
 a_{i(j-1)} &= d_1 - \frac{12 \cdot E \cdot I}{d_1^2 \cdot k_{ap}^*} \cdot \left(\frac{1}{n_{pi}} + \frac{1}{n_{p(i+1)}} \right); \quad i \neq j; \\
 a_{ij} &= 4 \cdot d_1 + \frac{6 \cdot E \cdot I}{d_1^2 \cdot k_{ap}^*} \cdot \left(\frac{1}{n_{pi}} + \frac{4}{n_{p(i+1)}} + \right. \\
 &\quad \left. + \frac{1}{n_{p(i+2)}} \right); \quad i = j; \\
 a_{i(j+1)} &= d_1 - \frac{12 \cdot E \cdot I}{d_1^2 \cdot k_{ap}^*} \cdot \left(\frac{1}{n_{p(i+1)}} + \right. \\
 &\quad \left. + \frac{1}{n_{p(i+2)}} \right); \quad i \neq j; \\
 a_{i(j+2)} &= \frac{6 \cdot E \cdot I}{n_{p(i+2)} \cdot d_1^2 \cdot k_{ap}^*}; \quad i \neq j; \\
 &\quad i = \overline{2, n_0 - 4}; \quad j = \overline{2, n_0 - 4}; \\
 &\dots\dots\dots \\
 a_{(n_0-3)(n_0-5)} &= \frac{6 \cdot E \cdot I}{n_{p(n_0-3)} \cdot d_1^2 \cdot k_{ap}^*}; \\
 a_{(n_0-3)(n_0-4)} &= d_1 - \frac{12 \cdot E \cdot I}{d_1^2 \cdot k_{ap}^*} \cdot \left(\frac{1}{n_{p(n_0-3)}} + \right. \\
 &\quad \left. + \frac{1}{n_{p(n_0-2)}} \right); \\
 a_{(n_0-3)(n_0-3)} &= 4 \cdot d_1 + \frac{6 \cdot E \cdot I}{d_1^2 \cdot k_{ap}^*} \cdot \left(\frac{1}{n_{p(n_0-3)}} + \right. \\
 &\quad \left. + \frac{4}{n_{p(n_0-2)}} + \frac{1}{n_{p(n_0-1)}} \right); \\
 a_{(n_0-3)(n_0-2)} &= d_1 - \frac{12 \cdot E \cdot I}{d_1^2 \cdot k_{ap}^*} \cdot \left(\frac{1}{n_{p(n_0-2)}} + \right. \\
 &\quad \left. + \frac{1}{n_{p(n_0-1)}} \right); \\
 a_{(n_0-2)(n_0-4)} &= \frac{6 \cdot E \cdot I}{n_{p(n_0-2)} \cdot d_1^2 \cdot k_{ap}^*};
 \end{aligned}$$

$$a_{(n_0-2)(n_0-3)} = d_1 - \frac{12 \cdot E \cdot I}{d_1^2 \cdot k_{ap}^*} \cdot \left(\frac{1}{n_p(n_0-2)} + \frac{1}{n_p(n_0-1)} \right);$$

$$a_{(n_0-2)(n_0-2)} = 4 \cdot d_1 + \frac{6 \cdot E \cdot I}{d_1^2 \cdot k_{ap}^*} \cdot \left(\frac{1}{n_p(n_0-2)} + \frac{4}{n_p(n_0-1)} + \frac{1}{n_p n_0} \right); \quad (8)$$

while the free terms have the equations:

$$b_1 = d_1 \cdot M_f + \frac{6 \cdot E \cdot I}{d_1} \cdot (f_{1,0} + 2 \cdot f_{2,0});$$

$$b_2 = (6 \cdot E \cdot I / d_1) \cdot f_{2,0}; \dots\dots\dots$$

$$b_i = 0; \quad i = \overline{3, n_0/2 - 2}; \dots\dots\dots$$

$$b_{\frac{n_0}{2}-1} = 6 \cdot A_{\frac{n_0}{2}, (\frac{n_0}{2}+1)} / (\frac{n_0}{2}+1) - \frac{6 \cdot E \cdot I}{d_1} \cdot (2 \cdot f_{\frac{n_0}{2}, 0} - f_{\frac{n_0}{2}+1, 0});$$

$$b_{\frac{n_0}{2}} = 6 \cdot A_{\frac{n_0}{2}, (\frac{n_0}{2}+1)} / (\frac{n_0}{2}) - \frac{6 \cdot E \cdot I}{d_1} \cdot (f_{\frac{n_0}{2}, 0} - 2 \cdot f_{\frac{n_0}{2}+1, 0}); \dots\dots\dots$$

$$b_{\frac{n_0}{2}+1} = \frac{6 \cdot E \cdot I}{d_1} \cdot f_{\frac{n_0}{2}+1, 0}; \dots\dots\dots$$

$$b_i = 0; \quad i = \overline{n_0/2 + 1, n_0 - 3}; \dots\dots\dots$$

$$b_{n_0-3} = \frac{6 \cdot E \cdot I}{d_1} \cdot f_{n_0-1, 0};$$

$$b_{n_0-1} = d_1 \cdot M_s - \frac{6 \cdot E \cdot I}{d_1} \cdot (2 \cdot f_{n_0-1, 0} - f_{n_0, 0}); \quad (9)$$

where

$$f_{1,0}, f_{2,0}, f_{n_0/2,0} = f_{4,0}, f_{n_0/2+1,0} = f_{5,0}, \quad (10)$$

$$f_{n_0-1,0} = f_{7,0}, f_{n_0,0} = f_{8,0},$$

($f_{i,0}$, $i = 1, 2, 4, 5, 7, 8$) are given by the equalities:

$$f_{1,0} = - \frac{1}{n_{p1} \cdot k_{ap}^*} \cdot \left[k_{crrf} \cdot (F_{crr})_f \cdot \sin \gamma_f + \frac{M_f}{d_1} \right];$$

$$f_{2,0} = M_f / (n_{p2} \cdot d_1 \cdot k_{ap}^*);$$

$$f_{4,0} = \frac{1}{n_{p4} \cdot k_{ap}^*} \cdot \left(1 - \frac{d}{A_1} \right) \cdot (M_i + M_v) \cdot g \cdot \cos \alpha_i;$$

$$f_{5,0} = \frac{1}{n_{p5} \cdot k_{ap}^*} \cdot \frac{d}{A_1} \cdot (M_i + M_v) \cdot g \cdot \cos \alpha_i;$$

$$f_{7,0} = M_s / (n_{p7} \cdot d_1 \cdot k_{ap}^*);$$

$$f_{8,0} = - \frac{1}{n_{p8} \cdot k_{ap}^*} \cdot \left[k_{crrs} \cdot (F_{crr})_s \cdot \sin \gamma_f + \frac{M_s}{d_1} \right]. \quad (11)$$

The reactions between the tires and the ground, in this case, are established by the expressions (6), where there are introduced the bending moments inferred from the above. At the same time, the condition of stability is maintained (7), in which the required adjustments will be made on the case.

In the previous expressions it shall be taken into account relations like:

$$(F_{crr})_f = K_T \cdot \left[\begin{array}{l} (M_i + M_v) \cdot g \cdot \\ (\sin \alpha_i + f \cdot \cos \alpha_i) + \\ + F_{vTl} + F_{iTl} \end{array} \right], \quad (12)$$

where:

$$K_T = 1 / (\cos \gamma_f + f \cdot \sin \gamma_f). \quad (13)$$

Other notations: $(F_{crr})_f$ – tractive force of the loaded platform; $(F_{crr})_s$ – braking force behind the platform; F_{vTl} – the total wind force developed along the platform (as a resistance force if it is opposed to the movement of the assembly); F_{iTl} – total inertia force in the case of accelerated or braked movement; E – the equivalent leasticity module of the platform, considered with an uniform geometry; I – moment of inertia of the cross section of the transport platform; M_i , M_v – mass of the load respectively the vehicle mass; M_f – bending moment developed by the normal component of the tractive force on the road (front) [8]; M_s – ; M_f – bending moment developed by the normal component of the braking force or pushing force on the road [8]; d – the distance from the front end of the platform to the center of mass of the assembly; d_1 – the distance between two consecutive axles; f – coefficient of rolling resistance of tires (considered the same for all

tires); $k_{c r f} = 1$, for angle γ_f positive (up direction), respectively $k_{c r f} = -1$, for the angle γ_f negative; g – gravity acceleration; α_l – the angle of inclination from the horizontal road; n_p – the number of tires belonging to an axle; γ_f – the angle between the drawbar towing and horizontal; $k_{c r s} = 1$, for the angle γ_s positive (situated up), respectively $k_{c r s} = -1$, for the angle γ_s negative; γ_s – the angle between the drawbar of binding of the platform to the means of braking or pushing from behind.

4. CONCLUSIONS

The paper addresses the stability of the the movement of convoys for transporting oversized industrial equipment, often in existing installations of process industries. The study is carried out for the case where the deformation of the suspension and tires is neglected, respectively opposite case. The platform for transportation is equivalent to a beam with constant stiffness over its entire length. It is inserted the effects of inertia forces, of wind forces and obviously the masses of the platform and transport equipment. In each case the user can make adjustments convenient in the case for downhill slope or hill.

REFERENCES

- [1] * * * Transports exceptionnels (definition des convois – types et regles pour la verification des ouvrages d'art) SETRA Octobre 1982 (<http://dtrf.setra.fr/pdf/pj/Dtrf/0002/Dtrf-0002509/DT2509.pdf> - accesat la 20.03.17)
- [2] * * * Convoi exceptionnel (https://fr.wikipedia.org/wiki/Convoi_exceptionnel (accesat la 20.03.17)
- [3] * * * <http://holleman.ro/services/transporturi-agabaritice/> - accesat la 20.03.17); <http://movers-auto.md/ro/shop/treyler-transport-perevozki-tyazhyolyih-negabaritnyih-gruzov.html> (accesat la 20.03.17)
- [4] * * * Regulament specific de acreditare în domeniul reglementat “Echipamente sub presiune transportabile” / RENAR, 2014
- [5] Felegeanu Daniel – Cătălin, Managementul riscurilor și securității industriale pentru prevenire, protecția și intervenție în caz de accidente majore la un obiectiv tip SEVESO, teză de doctorat, Universitatea “Vasile Alecsandri” din Bacău, 2016.
- [6] Iatan I. R., Salca Cristina, Stătescu M., Stabilitatea mișcării longitudinale a platformelor tip 4 x 4 pentru transportarea echipamentelor tehnologice agabaritice, Sinteze de Mecanică Teoretică și Aplicată, vol. 7, nr. 1, 2016, p. 51 – 62 (<http://search.proquest.com/openview/5218606c8647d4ed1c282ef0543690d9/1?pq-origsite=gscholar&cbl=2029206> (accesat la 20.03.17)
- [7] Buzdugan Gh., Rezistența materialelor, Editura Tehnică, București, 1980.
- [8] Iatan I. R., Vasilescu I., Transportarea utilajelor tehnologice agabaritice, Editura MatrixRom, București, 2002.
- [9] Marin C., Rezistența materialelor (partea I – solicitări simple), Editura Bibliotheca, Târgoviște, 2013.

MECHANICAL CHARACTERIZATION OF NANOSTRUCTURED THIN FILMS USED TO IMPROVE MECHATRONIC COMPONENTS

Liliana-Laura BADITA¹, Gheorghe GHEORGHE¹, Vasile BRATU², Valentin GORNOAVA¹, Marian VOCUREK¹, Aurel ZAPCIU¹, Iulian Sorin MUNTEANU¹

¹National Institute of Research and Development in Mechatronics and Measurement Technique, Pantelimon Road, No.6-8, Bucharest, Romania

²Valahia University of Targoviste, Faculty of Materials Engineering and Mechanics, 13 Aleea Sinaia Street, Targoviste, Romania

E-mail: badita_l@yahoo.com

Abstract. Taking into account the importance of mechatronic applications, researches regarding the possibility to improve the lifetime of mechatronic components were made. Nanostructured metallic thin films (Ti, Cr, Al and Ti/Al multilayer) were deposited on different types of steel substrates, because nanomaterials have exceptional properties in relation to the common materials. In this paper a part of the results obtained after mechanical and topographic characterization of the thin films are presented. Cr is the deposited thin film showing the highest hardness on the surface of steel substrate type OSC. After the scratch tests realized, Ti layer presented the best adhesion on all types of steel substrates used in experiments. The results of these researches could be extremely useful for engineers in the mechatronic field.

Keywords: thin films, nanomaterials, wear, topographic characterization, mechatronics

1. INTRODUCTION

Mechatronics, as science of mechanical-electronical-computer systems is the result of technological development of the recent decades. All high-tech products made today are mechatronic products: modern cars, industrial robots, microrobots used in military industry, nanorobots used in medical investigations, computers, printers, office equipment, equipment for medical investigations, prostheses and artificial organs, audio, video recording systems, etc [1].

The surfaces of these systems, made of the most suitable materials are subjected, in time, to some tribological processes. As a result, friction and wear appear – processes that manifest at micro- or nano-scale and are heavily dependent on surface interactions.

From tribological point of view, the wear is a process of progressive loss of material arising from the interaction of friction couplings surfaces. Between the wear and friction processes there is a close interdependence, meaning that the wear is a result of friction, and the state of surfaces resulting from friction influences the wear.

Wear is a mechanical process in that the strains associated with the destruction process of the surface may exceed the material strength and, thus, wear particles occur.

There are several wear mechanisms [2], which in some systems can be combined. These are: adhesive wear, abrasive wear [3], abrasive wear with the third body [4],

superficial fatigue wear, corrosion wear and fretting wear.

Taking into account these processes that have important effects on mechatronic systems, and the importance of the lifetime of components and systems in this area, the project researches presented in this paper focuses on the use of materials for tribological improvement of mechatronic components (high precision gears in miniature constructions, high precision bearings, components of mechatronic equipment for measuring, positioning and adjustment: bearers, guides, grippers, etc.).

The materials commonly used in the mechatronic field must have certain properties: excellent resistance to degradation for minimizing the particles generation which can adversely influence the systems. The surfaces must be hard to keep the wear to a minimum value.

Currently pure metals, stainless steels, and metal alloys are used.

The need to have resistant components, with anticorrosive composition and improved mechanical properties have led to the application of thin films of materials with superior properties on different surfaces used in mechatronic applications. Nanomaterials have exceptional properties in relation to the common materials, for example: the tensile strength is 20-50 times greater than the stainless steel; Young's modulus is 5 times higher than the stainless steel [5].

The main objective of this project was the characterization of thin films surfaces with micro and

nanometric structures deposited by physical methods. Researches on materials were directed mainly to study the mechanical properties of their surface. Studies and progress have been done by the use of very hard alloys and materials to keep the wear to a minimum value.

2. MATERIALS AND EXPERIMENTAL METHODS

2.1. Materials deposition

Thin films are deposited on mechatronic systems using different techniques.

Deposition methods must take into account the nature of phenomena that take place in the deposition process, diversity of thin films forming parameters (composition, structure, thickness, components spread in volume) and their application parameters (adhesion, wear resistance, corrosion resistance, porosity).

Therefore, under this project, studies have been conducted on thin films deposited by electrons beam evaporation.

Electrons beam evaporation is a technique that deposits metallic thin layers for the transposition of geometries from the mask in the substrate followed by lift-off.

Using the deposition process by electrons beam evaporation, nanostructured thin layers of Ti, Cr, Al and Ti/Al multilayer were deposited on four types of steel: OLC45, Ru11, C120 and OSC. OLC45 and Ru11 are used in mechatronics for the production of gauges, bushes, actuators, measuring dowels, opposite dowels, positioning stands, body of gauge. C120 and OSC are used in mechatronics for the production of screwed calibre and ledges, sensing heads, standards, punches. All these mechatronic components are subjected, over time, to wear [6].

Depositions were made with a Temescal FC-2000 system (Figure 1), a versatile evaporation system that supports a variety of accessories to meet almost any requirement. FC-2000 is a system with rapid cycle, blocked charging, which allows the source to remain in vacuum during recharging of the substrate.



Figure 1. System of deposition by electrons beam evaporation Temescal FC-2000 [7]

Standard components of this system are: control system, electrons beam source, power supply, vacuum pump and control, air system, water system, vacuum chamber.

Careful control of the electrons beam of Temescal offers completely digital operation, internal storage of up to 64 user-defined patterns and compatibility with almost any electrons beam gun commercially available.

2.2. Mechanical characterization of deposited thin films

Nanostructured thin films deposited for improving the resistance of mechatronic components in this project were physico-mechanically, structurally and topographically characterized.

Following these characterizations, information about the degree of influence of the material used were obtained, for a future enhancement of substrates resistance. Mechanical characterizations are important, highlighting important properties of deposited thin films, such as hardness and adhesion [8].

Determination of deposited thin films hardness

To determine the hardness of deposited thin films, the system for micro-hardness measurement HMV-2 was used, a system used within metallographic researches.

The automatic reading system for Vickers hardness tests (Figure 2) is designed to automatically measure the distance between opposite corners of the fingerprint to find the Vickers hardness based on the fingerprint image realized on the testing surface and captured by the CCD camera.



Figure 2. Automatic reading system for Vickers hardness tests

In the project, this system has been used to make measurements under the following conditions $T = 24^{\circ}\text{C}$; $H = 50\%$, $F = 98.07\text{mN}$, $HV_{0.01}$, 10 sec.

Determination of deposited thin films adhesion

By using the scratch tests it is possible to detect premature failure of the coatings adhesion in real applications. Scratching test method is a very reproducible quantitative technique, where the critical

loads at which errors occur are used to compare the cohesion or adhesion properties of the coatings or of the substrate material.

A CETR-UMT 2 system (Figure 3) was used to perform measurements and tests in order to determine the adhesion of thin films. The device allows two ways of sliding contacts: with alternative reciprocating or unidirectional sliding. It also allows to control the ambient temperature and humidity of air.



Figure 3. CETR-UMT 2 system

The device performs various types of tribological tests (pin-on-disk, ball-on-disc, block-on-ring, pin-on-ring and micro-indentation) having an interchangeable module, which can be mounted on a base structure.

This device has a modular design, with a basic module that contains the positioning system, the charging system, the driving system, the measurement system, the electronic system of control and data acquisition-processing. The device provides protection against vibrations.

The tests involved the execution of a measuring cycle in three steps, with a normal force of 5 N, a length of 5 mm, speed of 0.2 mm/s, having duration of 25 s.

2.3 Topographic characterization of thin films surfaces deposited and subjected to the scratch-tests

Topographic characterization of thin films deposited and subjected to scratch tests was carried out using atomic force microscopy (AFM). The working principle of the atomic force microscopy is the measurement of interaction force between a tip and the sample surface using special probes, made of a cantilever with a sharp tip at the end. The force applied on the tip by the surface leads to bending of the cantilever. Measuring the deflection of cantilever, it is possible to evaluate the interaction force tip – surface. Acquisition of AFM surface topography can be made by registering the small deviations of the elastic cantilever [9].

AFM measurements were performed using a microscope type NT-MDT NTEGRA Probe NanoLaboratory (Figure

4) [10]. This type of microscope has the following basic systems and modules: base unit, base modules (probes, exchange support, scanner, heating platform, fluid cells, etc.), protective hood, optic viewing system, vibration isolation system and control system (SPM controller, thermocontroller, computer with interface panel).

Surfaces of 50/50 μm situated in different locations of samples were scanned and topographic parameters were determined using NOVA SPM Software – the software of NT-MDT NTEGRA Probe NanoLaboratory microscope.



Figure 4. AFM microscope, NT-MDT NTEGRA Probe NanoLaboratory. 1 – base unit; 2 – probe; 3 – vibrations isolation system; 4 – optical viewing system

Following this investigation, it was possible to identify more clearly the nature of the damage and to determine the roughness parameters of all characterized surfaces.

3. RESULTS

Ti, Cr, Al thin layers and Ti/Al multilayer were obtained following the deposition by electrons beam evaporation on four kinds of steel: OLC45, Ru11, C120 and OSC. These layers had thickness of 50 nm (Cr and Al), 100 nm (Ti), and Ti/Al multilayer with a thickness of 50 nm each layer (total multilayer thickness is 100 nm).

After scanning $50 \times 50 \mu\text{m}$ areas of the different films deposited on all the substrates, different topographic parameters have been analyzed (surface roughness R_a , surface asymmetry R_{sk} , coefficient of kurtosis R_{ka}) which provide information on distribution and damage of the deposited layers.

The roughness was used as a deterioration indicator of the deposited layer to obtain information regarding the variation in height from one point to another. This is quantified by deviations of the real surface from its ideal form. If these deviations are large, the surface is rough; if the deviations are small, the surface is smooth.

Asymmetry index R_{sk} assesses the asymmetry degree of a distribution and characterizes, together with the coefficient of kurtosis R_{ka} , the shape of the distribution. The asymmetry index R_{sk} is negative or positive as the survey distribution is asymmetrical to the left or,

respectively, to the right. A symmetrical distribution, such as the normal distribution, has the zero asymmetry.

The coefficient of kurtosis R_{ka} is part of indices that assess the form of a distribution. A high coefficient of kurtosis shows a distribution with great "tails" (categories far from average are presented), while a small coefficient of kurtosis shows an assignment where are presented less categories far from average. In the case of a distribution close to the normal distribution, the coefficient of kurtosis is around 3. Based on this result, the excess E is defined as the difference between the coefficient of kurtosis and 3. For $E > 0$, the distribution is called leptokurtic (the height of the curve is higher compared to the normal), and for $E < 0$, it is called platykurtic (the curve is flattened). If $E = 0$, the division is mesokurtic.

After analysing the roughness average values of deposited films it was seen that on the OSC steel substrate, films with the highest uniform surface are deposited. Titanium has the most uniform surface, and from the thin films deposited with thickness of 50 nm, aluminium is more uniformly deposited on this type of steel substrate. It can be concluded that layers more uniformly were obtained starting from chromium, aluminium and titanium. In the case of Ti/Al multilayer that has a more uniform arrangement on the C120 type substrate.

Taking into account that the average values of the asymmetry index, in the case of all three types of deposited layers, were very close to zero, it can be concluded that they have a symmetrical distribution. The only exception is the Ti/Al multilayer, which has a positive asymmetry index, bigger than 1, so it is a deposition with survey distribution asymmetrical to the left right.

For samples in this project, the excess values obtained after the analysis of coefficient of kurtosis indicate a platykurtic distribution of all thin films deposited on all four substrates types. The exception is in the case of Ti film of 100 nm thickness, the excess of which has a positive value, therefore a leptokurtic distribution.

3.1. Determination of deposited thin layers hardness

As a result of the hardness measurements made at a temperature of 24°C, humidity of 50%, with a force $F = 98.07\text{mN}$, $HV_{0,01}$ in 10 seconds were obtained the results shown in Table 1.

Table 1. Results obtained from measuring the hardness of nanostructured layers deposited on different types of steel

Layer	Substrate	M (The average value of hardness)
Ti	OLC45	91.5
	Rul1	79.0
	C120	86.9
	OSC	91.0
Cr	OLC45	94.8
	Rul1	94.3

Al	C120	94.4
	OSC	96.6
	OLC45	81.4
	Rul1	84.9
	C120	84.8
Ti/Al	OLC45	83.9
	Rul1	81.3
	C120	84.3
	OSC	86.3

These values were analysed and hardness variations of the thin films deposited on a particular substrate type were obtained, variations which can be seen in the following figures.

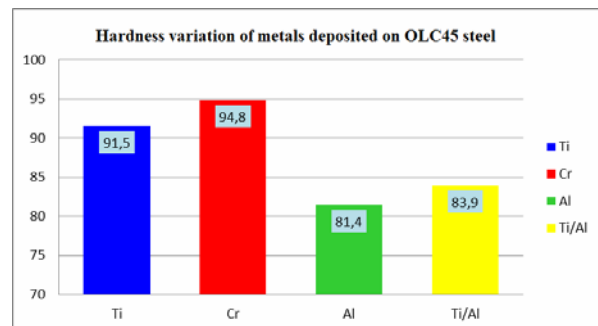


Figure 5. Variation of metallic layers hardness deposited on OLC45 steel

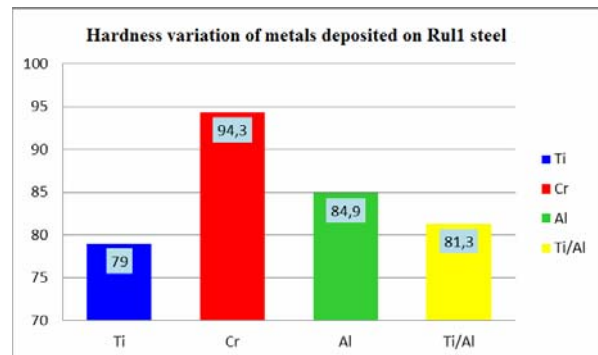


Figure 6. Variation of metallic layers hardness deposited on Rul1 steel

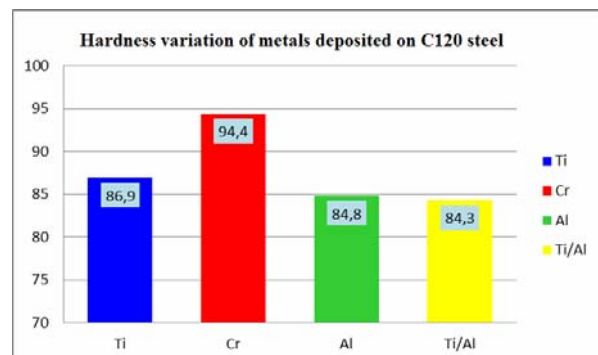


Figure 7. Variation of metallic layers hardness deposited on C120 steel

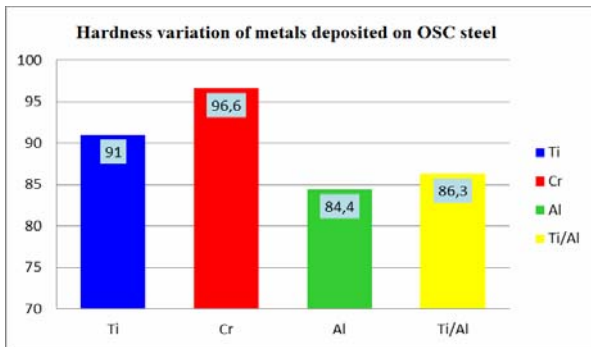


Figure 8. Variation of metallic layers hardness deposited on OSC steel

It is observed that on all the four types of substrate, Cr is the deposited thin film that has the highest hardness, having an average value greater than 90, in all four cases. Ti also has a high hardness, but when it is combined with Al, its hardness decreases given the fact that the top layer is Al, a metal with a lower hardness.

3.2. Determination of deposited thin films adherence by scratch tests

Adhesion of metal layers deposited on various steel substrates was determined by the scratch tests using CETR-UMT 2 system shown in Figure 3.

Tangential force F_x , the normal force F_z , movement in the normal direction Z, movement in the tangential direction Y, time T, friction force F_f (value in module of F_x), friction coefficient COF (ratio F_x/F_z in module) were used and determined.

The average values obtained from these tests are presented in table 2.

Table 2. The average values obtained from tests and measurements of adhesion.

Layer	Substrate	Time [s]	Depth [mm]	Force F_f [N]	COF
Al 50nm	OLC45	3.729	0.016	3.497	0.727
	Rul1	3.933	0.01	3.229	0.664
	C120	2.5	0.009	2.972	0.605
	OSC	4.430	0.02	6.272	1.267
Cr 50nm	OLC45	2.612	0.018	4.876	0.991
	Rul1	1.606	0.01	3.891	0.802
	C120	2.012	0.013	3.557	0.719
Ti 100nm	OLC45	1.931	0.01	3.915	0.81
	Rul1	1.960	0.01	3.139	0.639
	C120	2.052	0.012	4.16	0.846
Ti 50nm + Al 50nm	OLC45	1.656	0.01	4.482	0.91
	Rul1	2.053	0.013	3.658	0.739
	C120	2.012	0.012	3.199	0.647
	OSC	1.859	0.01	3.503	0.702
	OSC	2.082	0.017	3.354	0.701

Analysis of these results leads to the following conclusions:

- The time shown in the third column indicates the moment of separation of the deposited superficial layer.
- At this point there is a significant increase in the depth of penetration of the testing device.
- The values of the friction force F_f and the sliding friction coefficient COF are appropriate to the produced phenomenon.

Friction coefficient COF values are decreasing in the order of Al, Cr, Ti, Ti/Al. These values are generated and by adherent structure of the deposited material, and by the peeling strength of the hardened surface layer.

Regarding the moment of separation of the deposited surface layer, Al detaches the fastest from the C120 substrate, Cr from the Rul1 substrate, Ti from OSC substrate, and the Ti/Al multilayer detaches the fastest from C120 substrate.

If are taken into account, mainly, the values of detaching times on the four substrates types it can be see that Al shows the latest moment of separation on all four steels, which may indicate a good adhesion between it and variants of steel.

3.3. Topographic characterization of thin films surfaces deposited and submitted to the scratch tests

After the scratch tests on each sample and examining the scratch traces with the optical microscope, several types of surfaces damages resulted from critical loads were detected: deformations and detachments of material, detached fragments of deposited layers, semicircular cracks of the coating, raising of the material on the edges, cutting of the base material and oxidation.

There are also areas with uniform surfaces, almost without defects.

Identifying more clearly the nature of damages and topographic parameters setting of all the investigated surfaces was performed by atomic force microscopy.

2D images, 3D images, calculated topographic parameters (Figures 9 – 12) and profiles on X and Y axes of these surfaces were obtained.

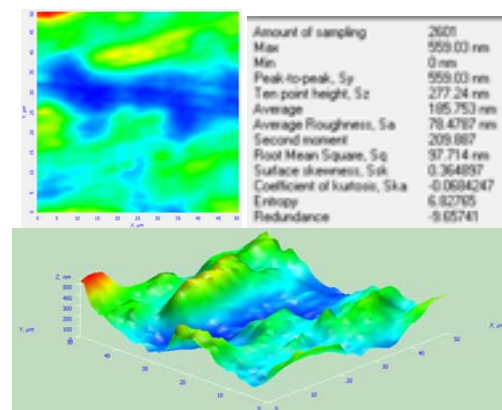


Figure 9. AFM surface characterization of Cr thin films deposited on substrate type OLC45 and submitted to scratch tests

Following these measurements, the values of roughness obtained indicates a damage of the deposited films surfaces. It is about the surfaces where scratches, particles that came out of the surface or cracks were observed. However, taking into account that the averages values of roughness are of the nm order it can be considered that there was not a very high destruction of those surfaces. This allows considering it almost smooth surfaces. Ti layer deposited on the all four types of steel shows the lowest value of the roughness among all the layers deposited. The fact that the scratch tests had not greatly damaged the surface can be interpreted as good adhesion of Ti layer on all types of steel substrates used in experiments.

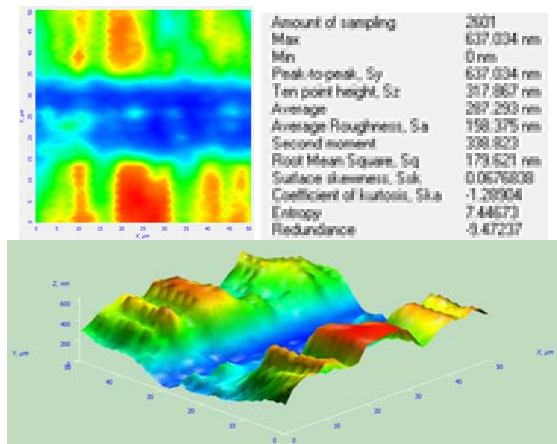


Figure 10. AFM surface characterization of Ti thin films deposited on substrate type Ru11 and submitted to scratch tests

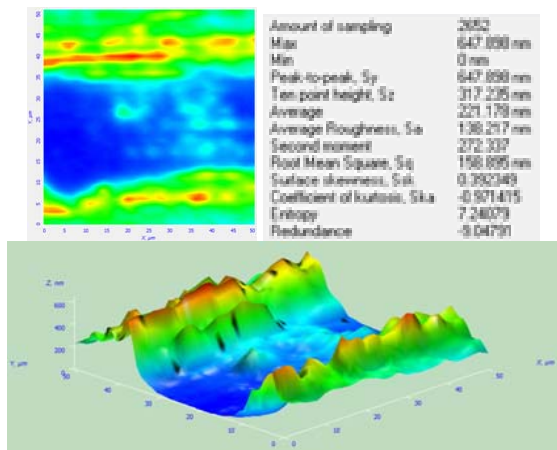


Fig.11. AFM surface characterization of Al thin films deposited on substrate type C120 and submitted to scratch tests

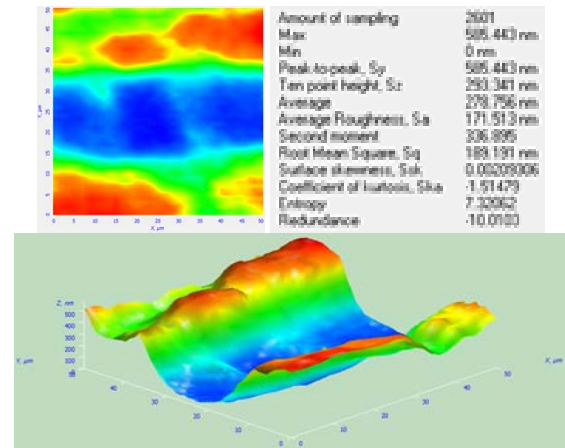


Figure 12. AFM surface characterization of Ti+Al thin films deposited on substrate type OSC and submitted to scratch tests

Asymmetry index R_{sk} , for all the layers deposited, has a positive average value indicating a survey asymmetric distribution to the right. If one takes into account that for some layers the values of this index are close to zero (Al deposited on Ru1=0.3 and Cr deposited on C120=0.25), these could be considered normal distributions.

Coefficient of kurtosis R_{ka} shows for all deposited layers values that lead to a negative excess, indicating a platykurtic distribution. For Ti layer deposited on the OSC substrate, the excess has a value close to zero (0.56), giving the opportunity to be considered as mesokurtic distribution. Also, the Ti layer deposited on the OSC type substrate has a value close to 3 (ie 2.44), which indicates the possibility of considering a normal distribution.

4. CONCLUSIONS

After the study performed the importance of such deposited materials was highlighted for the mechatronic domain:

- tests and measurements have been made for physico-mechanical and topographic characterizations of nanostructured Al, Cr, Ti thin films and of Ti/Al multilayer deposited by the method of electrons beam evaporation on steel substrates type OLC54, Ru11, C120, OSC;
- it was observed that on the all four substrates, Cr is the deposited thin film showing the highest hardness. Ti also has a high hardness, but when it is combined with Al, its hardness decreases, given that the top layer is Al, a metal with lower hardness.
- the highest average hardness for all four types of nanometric layers was obtained on the surface of OSC substrate;
- Al detaches the fastest from the C120 substrate, Cr from the Ru11 substrate, Ti from OSC substrate, and the Ti/Al multilayer detaches the fastest from C120 substrate;
- for the topographic characterization, the values of some tribological parameters, such as roughness,

asymmetry index and coefficient of kurtosis, were analysed;

- taking into account that the average values of roughness are of the nm order it was considered that there was not a very high destruction of deposited layers.
- the fact that the scratch tests had not greatly damaged the surface can be interpreted as good adhesion of Ti layer on all types of steel substrates used in experiments;
- the positive value of the asymmetry index for all layers deposited indicates a survey distribution asymmetric to the right;
- coefficient of kurtosis shows for all layers deposited values that lead to a negative excess, indicating a platykurtic distribution.

The results of these researches could be useful for engineers in the mechatronic field, who are studying the functioning conditions of mechanical parts components and not only, establishing the functional role of each component in the whole assembly and choosing materials that correspond to their proper operation.

REFERENCES

- [1] Bolton W. *Mechatronics – electronic control systems in mechanical and electrical engineering*. Harlow: Pearson Education Ltd., 2008
- [2] Bergmann G., Graichen F., Rohlmann A., Verdonschot N., van Lenthe G. H. Frictional heating of total hip implants, Part 1: measurements in patients; *Journal of Biomechanics* 2001; 34: 421-428.
- [3] Dong Z. L., Khor K. A., Quek C. H., White T. J., Cheang P. *Biomaterials* 2003; 24: 97–105.
- [4] Gheorghe Gh.I., Badita L.L. *Advanced micro and nanotechnologies in mechatronics*. Bucharest: Ed. CEFIN, 2009.
- [5] Buschan B. *Springer Handbook of Nanotechnology*, New York: Springer, 2007.
- [6] Gornoava V., Gheorghe Gh.I., Badita L.L. Tribological characterization of the nanostructured thin films deposited by intelligent methods, for mechatronic and biomedical applications. *The Scientific Bulletin of Valahia University – Materials and Mechanics* 2016; 14(11): 69-74.
- [7] <https://temescal.ferrotec.com/systems/fcbjd-2000/>
- [8] Bhushan B. *Handbook of Micro/nanotribology*, Boca Raton: CRC Press, 1999.
- [9] Binnig G., Quate C.F., Gerber Ch. Atomic Force Microscope, *Physical Review Letters* 1986; 56(9): 930-933.
- [10] <http://www.ntmdt-si.com/modular-afm/prima>
- [11] Despa V., Gheorghe Gh.I., Badita L.L., Aspects regarding the quality of surfaces obtained by using the Selective Laser Sintering Technology, *The Scientific Bulletin of Valahia University - Materials and Mechanics* 2015, 13(10): 133-137.

THEORETICAL MODEL USED IN MONITORING THE LOSSES FROM WATER NETWORKS DUE TO WATER CONTROL MEASUREMENT BATTERIES

Vasile ANDREI¹, Cornel MARIN², Alexis NEGREA²

¹Targoviste Company Water

²Valahia University of Targoviste, Faculty of Materials Engineering and Mechanics,
Department of Materials Engineering, Mechatronics and Robotics,
13 Aleea Sinaia Street, Targoviste, Romania

E-mail: marin_cor@yahoo.com

Abstract: According to the IWA norms, the water loss category includes also the apparent loss water due to measurement errors of the water meters used at the connections. This paper presents the experimental results obtained during two years of registrations in TARGOVISTE's Water Company network. A program for verifying the water meters used for connections has been implemented according to a statistical distribution, depending on the number of appliances and their dimensions. Using a theoretical simulation model, calibrated on the basis of the actual reference flows measured on the metrology approved measuring stand, a procedure was developed to assess the level of deviations in the fully metered water distribution network. Depending on the values of deviations and flows actually recorded by the meters in the distribution network, it was possible to estimate the percentage of the losses from the actually used water meters.

Keywords: Water meter, loss water measurement stand, theoretical simulation model.

1. INTRODUCTION

Knowing the errors in measuring water flow rates in city water networks is a major requirement for accurately compiling balance sheets for specific consumption and consumption forecasts in the short and medium term.

In order to correctly evaluate these errors, flow measurements will be made on an approved stand for water meters as they are brought out of the field, following the following national rules: [10, 11, 12, 13]
- the batch water meters with the nominal diameters Dn 15, Dn 25 and Dn 32 will be checked on stand of CAT - TÂRGOVISTE water company - authorized by BRML - Romanian Office for Metrology and Lengths by 1 / 3 pieces survey (33%);

- batch water meters with nominal diameters smaller than Dn 15 will be checked by 1 / 2 pieces survey (50%);
- batch water meters with nominal diameters larger than Dn 32 will be 1/1 (100%) checked.

During these checks, the flow rate at which the water meter starts to record is measured: Q_{start} .

Most water meters currently approved and marketed on the market are with turbine, single or multiple, dry, wet or semi-dry screen, with constant or volumetric cross section, moving parts (kinetic transducers). Electronic water meters using the COANDA effect are less commonly used (less than 5% of bundles).

Kinetic water meters used in meters are meters that are based on the principle of proportionality between the turbine rotation speed and the speed of water passing through the meter (Figure 1) [6, 7, 8, 9]

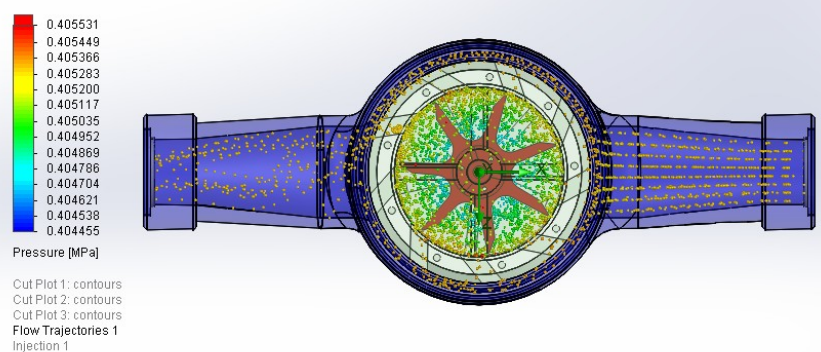


Figure 1

The turbine movement is transmitted via a wheel drive or magnetic induction to an integrator that measures and displays the volume of water consumed by each time by integrating the speed with time according to the passage section. The main metrological characteristics of a water meter are:

- $Q_{nominal}$ is the nominal flow;
- D_n nominal diameter;
- A, B, C, D precision class.

An important feature of all measuring devices is measuring accuracy.

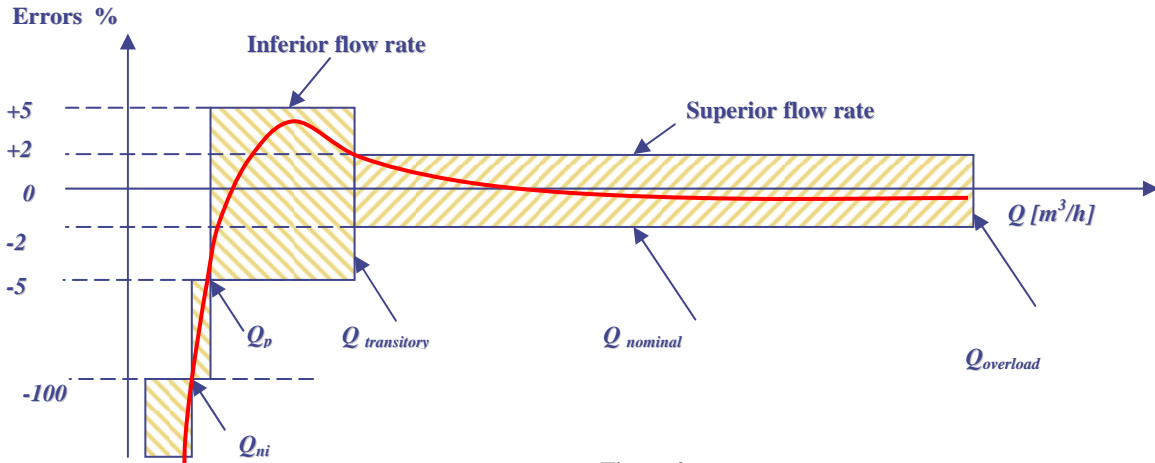


Figure 2

An essential and important element from a practical point of view, but not specified by the manufacturers in the prospectus of these devices, is the sensitivity of the water meter [1,2,3].

This is a feature of all measuring devices related to measurement accuracy, type-dimension and operating principle (manufacturing technology) The sensitivity of the meter is expressed by the sensitivity threshold that is defined by two flows:

- Q_p starting flow rate - representing the flow at which the rotor is moving, recording the flow passing through the counter. Typically, this flow is characterized by large negative errors, which begin to decrease with its increase [6,7,8,9] (Figure 2). We defines the percent flow rate error as follows:

$$\varepsilon_p = \frac{Q_p - Q_{real}}{Q_{real}} \cdot 100 \% \quad (1)$$

- Q_{ni} unregistered maximum flow rate through the water meter without producing the turbine motion, no consumption being recorded. Practically the maximum unregistered Q_{ni} rate is considered:

$$Q_{ni} = 0,99 \cdot Q_p \quad (2)$$

The measurement error in this case is -100%. (Fig. 2). In order to highlight the influence of starting flow rate Q_p on actual consumption in meter counting, the special metrological test bench was experimentally determined by errors and the error curve for different

Depending on the accuracy of the water volume measurements, the water meters are framed in the precision classes: A, B, C, D ; the best being the precision class D and the lowest, the precision class A . Classification in a class by the BRML metrological norms in Romania, is made according to the errors recorded by the apparatus at four standardized flows: Q_{minim} , $Q_{transitory}$, $Q_{nominal}$, $Q_{overload}$, having different values depending on the diameter of the water meter (flow rate) [12,13] (Figure 2).

drinking water meters with different nominal diameters was constructed.

Figure 2 shows the form of the standard curve, making clear both the value of the starting Q_p flow rate and the variance of the measurement error.

2. PROCESSING OF EXPERIMENTAL DATA

For the processing of the experimental data obtained by measuring on the approved stand for water meter verification CAT, the calculation relations used for:

- Deviation flow rates measured for the follows flow rates: Q_{min} the minimum flow rate, Q_{tr} - transitory flow rate ; Q_n - nominal flow rate (in liters / min):

$$\begin{aligned} \Delta_{mini} &= Q_{min Mi} - Q_{min R} \\ \Delta_{tri} &= Q_{tr Mi} - Q_{tr R} \\ \Delta_{ni} &= Q_{n Mi} - Q_{n R} \end{aligned} \quad (3)$$

The index i corresponds to the measured measurements ($i = 1, \dots, n$), and the index R and M indices have the meanings: R corresponds to the regulated flow ; M corresponds to the measured flow.

- Average deviations of the minimum and transient minimum flow rates:

$$\begin{aligned} \bar{\Delta}_{min} &= \frac{1}{n} \sum_{i=1}^n \Delta_{mini}; \quad \bar{\Delta}_{tr} = \frac{1}{n} \sum_{i=1}^n \Delta_{tri} \\ \bar{\Delta}_n &= \frac{1}{n} \sum_{i=1}^n \Delta_{ni} \end{aligned} \quad (4)$$

- Minimum, transient and nominal flow rate errors (in percent %):

$$\varepsilon_{min} = \frac{\overline{\Delta_{min}}}{Q_{minR}} \cdot 100 \% ;$$

$$\varepsilon_{tr} = \frac{\overline{\Delta_{tr}}}{Q_{trR}} \cdot 100 \% \quad (5)$$

$$\varepsilon_n = \frac{\overline{\Delta_n}}{Q_{nR}} \cdot 100 \%$$

Figure 3 shows the two curves of flow rates / deviations Δ according to the flow passing through a water meter:

- the regulated standard flow deviation Δ - R;
- the measured flow deviations Δ - M

a. For the regulated standard curve (R), it can be seen from Figure 3 that:

- for the minimum Q_{min} flow rate and the transient deceleration Q_{tr} the related deviations Δ_{min} and Δ_{tr} are between + 5% and -5%.

- for the nominal flow Q_n and the overload Q , the measurement deviations Δ_n and Δ are between + 2% and -2%.

b. For the curve determined by measurements on the stand (M), it can be seen from Figure 3 that:

- for the start-up flow rate (Q_p) the Δ_p deviation is greater than 5%, this aspect must be considered much more rigorously, in the present paper we only summarize the minimum, nominal and transient flows.

- for the minimum Q_{min} flow the deviation Δ_{min} is greater than 5%

- for nominal Q_n and overload Q_s , the measurement deviations Δ_n and Δ are between + 2% and -2%

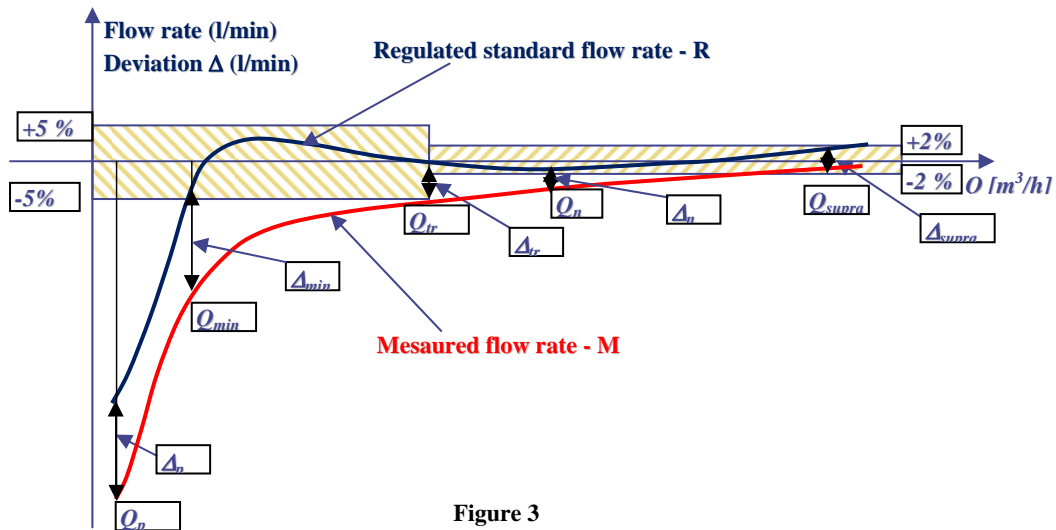


Figure 3

4. EXPERIMENTAL SITE DATA COLLECTON

The experimental measurements were carried out on a district in DAMBOVITA county comprising 146 fully metered water meters of the same type Dn 20 C class

for a continuous 4-year operation through which water was delivered with an average hardness of 12⁰ Germans degree.



Figure 4

The analyzed district was divided into 10 zones (Figure 4) having approximately the same number of branches, where a counter was assigned to which a data logger was attached. At the entrance to the water network a Dn 80 class C meter with double wrinkle dial was installed to record the total flow delivered. The statistical analysis of the measurements made on 10 water connections to connected households and to the sewerage network,

where the evolution of debits was recorded using data logging for a period of one month, the data being downloaded every two days, led to the elaboration of a Work procedures and processing of the experimental data presented below. Graphical recording of a sample with data on water volumes from datalogging is described in Figure 5.

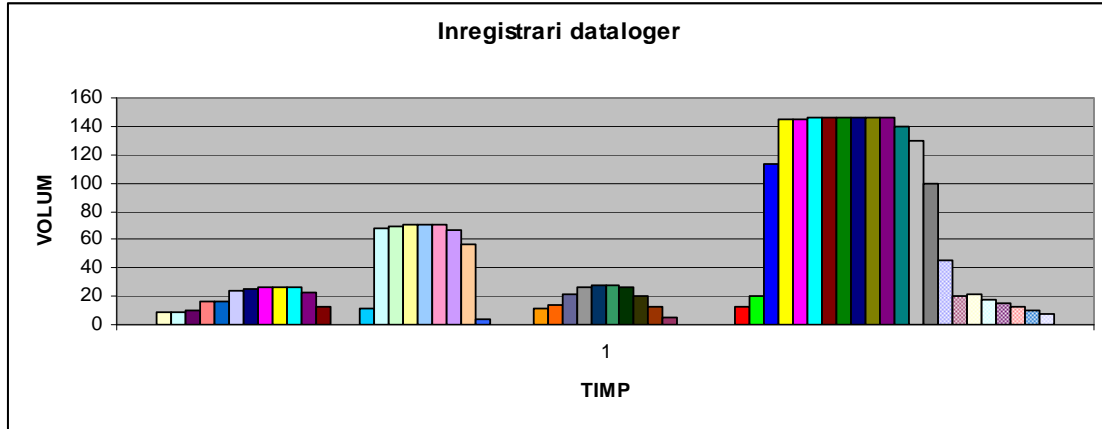


Figure 5

With the data records above, a database was created which generated a monthly average flow curve actually measured by the ten water meters ($q_1 \dots q_{10}$) from the studied connections, according to time, during the a one month:

$$Q_{monthly\ average} = q_1 + q_2 + \dots + q_{10} \quad (6)$$

The data recorded by the 10 data logger connections were processed using the MATLAB equivalent method and led to a monthly average flow distribution law based on the three Q_{min} , Q_{tr} , Q_n flow rates having a specific evolution shown in Figure 6.

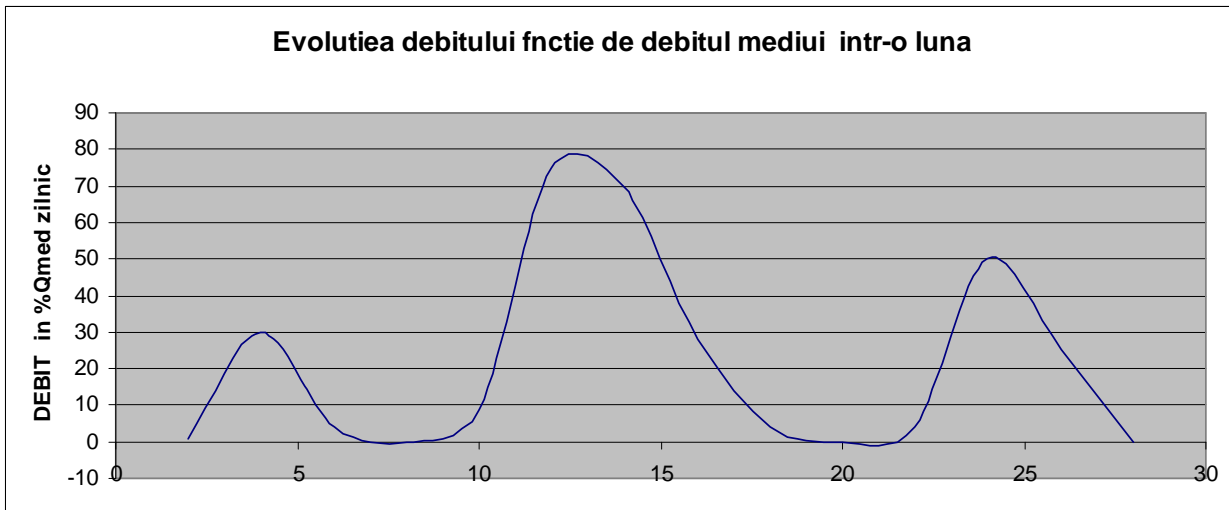


Figure 6

Distribution ratio of average monthly flow rate monthly $Q_{average\ monthly}$, in connections with Q_{min} , Q_{tr} , Q_n flow rates can be approximated by the equivalent surface method using the following simplified relations:

$$Q_{min} = 20\% Q_{average\ monthly} \quad (7)$$

$$Q_{tr} = 50\% Q_{average\ monthly} \quad (8)$$

$$Q_n = 30\% Q_{average\ monthly} \quad (9)$$

The starting flow rate Q_p can be appreciated as representing a quantity of water that flows continuously but is not recorded by the counters.

This flow rate can be approximated in the first step as a percentage of 1% of the meters in the analyzed area, related to the average starting rate measured on the stand.

Annexes A, A2 present the results obtained on the assessment of the measurement deviation in the analyzed district area.

We calculated the unregistered flow rates for the minimum flow rate (Q_{mi-NI}), the transient flow (Q_{tr-NI}), the nominal flow (Q_{n-NI}) for relations:

$$Q_{min\ NI} = e_{min} \times Q_{min} \quad (10)$$

$$Q_{tr\ NI} = e_{tr} \times Q_{tr} \quad (11)$$

$$Q_{n\ NI} = e_n \times Q_n \quad (12)$$

The unregistered monthly average flow is the sum of the three debits above:

$$Q_{NI} = Q_{min\ NI} + Q_{tr\ NI} + Q_{n\ NI} \quad (13)$$

Unregistered startup flow is determined according to the relationship:

$$Q_p = 1\% \times Nr.cont. \times Q_{paverage} \quad (14)$$

The total unregistered flow is determined according to the relationship:

$$Q_{total} = Q_{average\ monthly} + Q_p \quad (15)$$

The total measurement error is calculated as the ratio between the total unregistered flow rate and the total measured rate, expressed as a percentage:

$$\varepsilon_{tot} = \frac{Q_{mediu\ lunar\ NI} + Q_p}{Q_{mediu\ lunar}} \cdot 100 \quad \% \quad (16)$$

The calculations for these debits and measurement errors are given in Annexes A1, A2.

The green values are within the limits of the IWA norms and the values that do not fall within these limits are red.

4. THEORETICAL SIMULATION MODEL

The theoretical simulation model, calibrated on the basis of the actual reference flows measured are achieved with professional software SOLID WORKS- FLOW SIMULATION. The simulation model is shown in Figure 7. The input data are presented in Table 1.

The simulation achieved with FLOW SIMULATION lead to the results presented as follows:

Figure 8 - Simulating the water velocity in the outlet

Figure 9 - Simulation of water pressure in the outlet

Figure 10 - Simulation of the pressure inside the turbine.

Table 1

Goal Name	Unit	Value	Averaged Value	Minimum Value	Maximum Value	Progress [%]
GG Max Velocity 1	[mm/s]	1246.842008	1246.973223	1229.134108	1265.088691	100
GG Torque (Y) 1	[N*mm]	-0.337095557	-0.366292725	-0.457597104	-0.274885938	100

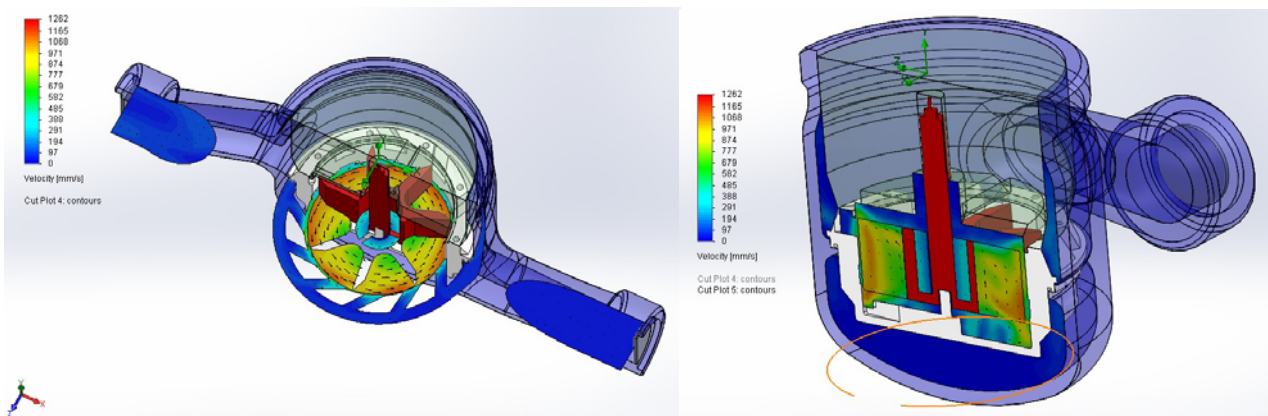


Figure 7

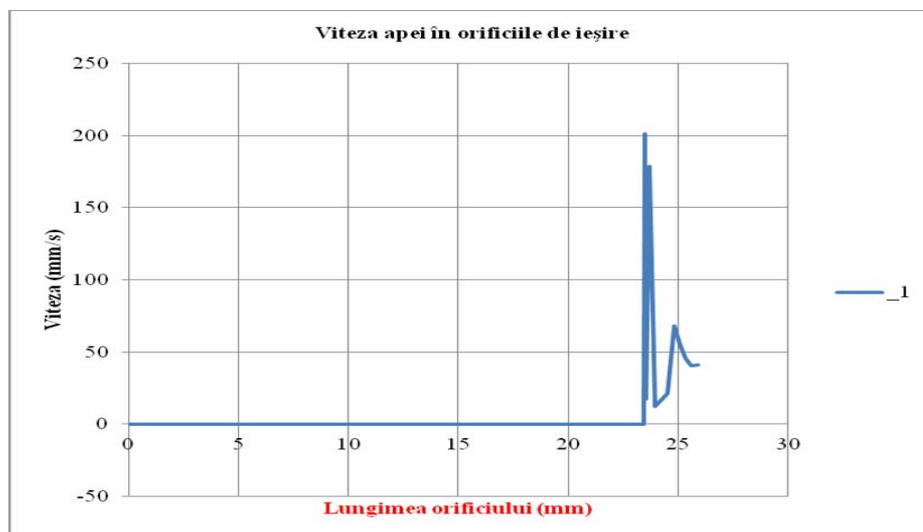


Figure 8

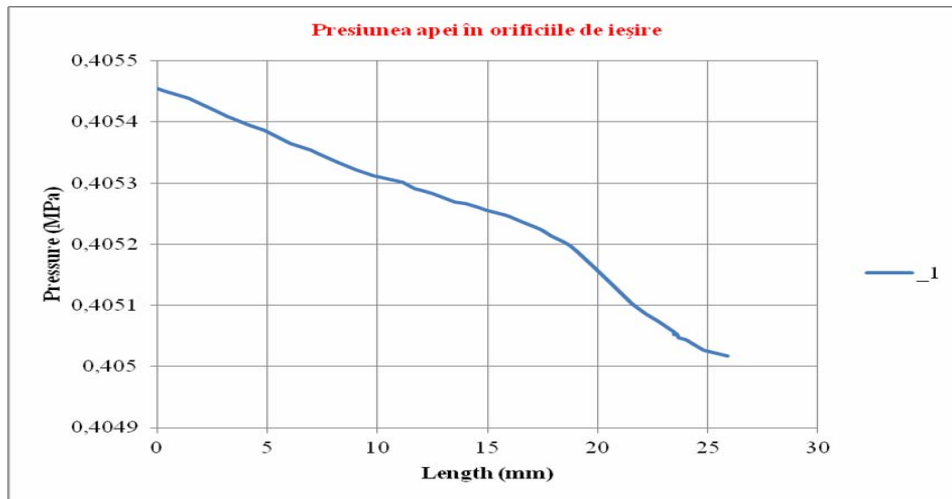


Figure 9

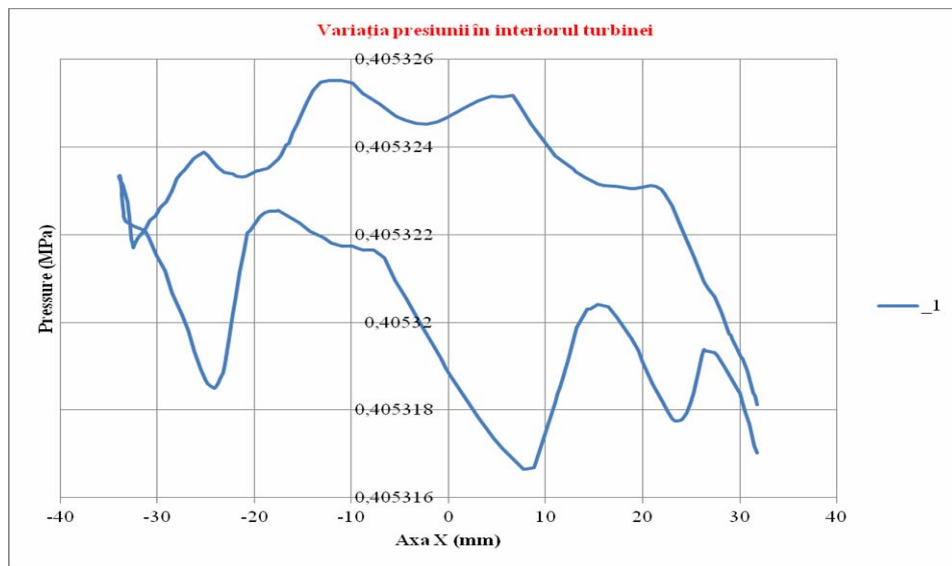


Figure 10

5. CONCLUSIONS

- the measured values of the meters under test lead to an error:

$$\varepsilon_{tot} = -11.262\% \quad (17)$$

- since the 10 counters were chosen randomly from the 146 connections, it results that on the analyzed area, the operator has a commercial loss of 25.26% due to the counters used.

- in practice it was found that on the analyzed network, the delivery flow rate ($Q_{delivery}$) was in the analyzed period (one month):

$$Q_{delivery} = 2117,1 \text{ mc / month} \quad (18)$$

The average monthly total flow rate measured from the readings of the 146 counters was:

$$Q_{Taverage\ monthly} = q_1 + q_2 + \dots + q_{146}$$

$$Q_{Taverage\ monthly} = 1473.43 \text{ mc / month} \quad (19)$$

The difference between the delivery and the total monthly average flow rate measured ($Q_{Taverage\ monthly}$) is:

$$Q_{delivery} - Q_{Taverage\ monthly} = 634,668 \text{ mc / month} \quad (20)$$

This difference flow rate represents a loss of 30.4%, although no damage to the network was recorded during the analyzed period.

The difference between the loss determined by the theoretical method presented above of 11.262% and the experimentally measured in situ of 12.1% may have the following causes:

- The existence of meters with deviations higher than the average resulting from the developed model.
- Unpunished small spikes or start-up flows higher than the approximate one in the model shown.
- the exposed method uses only deviations measured in three points, namely the deviations in Q_{min} , Q_{tr} and Q_n .

6. SOLUTIONS PROPOSED

It is possible to increase the number of points for determining the deviations measured, for example by dividing the analysis interval between the minimum

flow rate Q_{min} and the maximum flow rate Q_{max} in the "m-1" subintervals to which the flow points correspond (q_1, q_2, \dots, q_m) with the measurement deviations ($\Delta_1, \Delta_2, \dots, \Delta_m$) between the regulated standard curve and the measured curve on the stand for the verified water meter.

REFERENCES:

[1] Ionescu Fl., Catrina D., *Mecanica fluidelor și acționări hidraulice și pneumatice*, E.D.P., București, 1980
 [2] C. Mateescu – *Hidraulica*, Editura Didactica si Pedagogica Bucuresti, 1963.,
 [3] C. Iamandi si V. Petrescu *Mecanica fluidelor*, – Editura Didactica si Pedagogica, Bucuresti, 1978.
 [4] J.Florea, V. Panaiteescu – *Mecanica fluidelor*, Editura Didactica si Pedagogica, Buresti, 1979.
 [5] Marin V. s.a, *Sisteme hidraulice de acționare și reglare automată*, Editura Tehnică, București, 1981

[6] Ștefan Vintila, coordonator - Manualul de instalații .Editura ARTECON –București , 2002
 [7] Sergiu Calos, s.a. - Rețele de distribuția apei - Editura Chișinau, 2004
 [8] L. Dumitrescu - Instalatii sanitare pentru ansambluri de clădiri - Editura Tehnica, București, 1980
 [9] Ștefan Vintilă, s.a. - MANUAL DE INSTALAȚII ÎN CONSTRUCȚII Vol. 4 – Instalații sanitare. Editura ARTENCO București, AGIR 2002
 [10] *** HG nr. 264/2006 - Stabilirea condițiilor de introducere pe piata si de punere in functiune a mijloacelor de masurare
 [11] *** HG nr. 711/2015 - Stabilirea condițiilor pentru punerea la dispoziție pe piață a mijloacelor de măsurare
 [12] *** Ordin BRML nr. 148/2012 - Aprobarea Listei oficiale a mijloacelor de măsurare supuse controlului metrologic legal L.O.-2012
 [13] *** HG nr. 384/1998 Recunoasterea etaloanelor nationale

ANEXE A1

Anexa A1
TABEL A1
Tip contor WE Dn 15 Cp C

nr.crt	serii contoare	UM	1	2	3	4	5	6	7	8	9	10	TOTAL	valori medii
1	Q_p	Vh	2,8	3,3	15,5	9,6	10,2	14,8	12,7	15,2	9,5	10,4	104	10,4
2	$Q_{min} Mi$	Vh	9,98	10,02	0	0	10,2	0	0	0	9,8	10,4	50,4	5,04
3	$Q_{min} R$	Vh	10,48	10,48	10,48	10,48	10,48	10,48	10,48	10,48	10,48	10,48	104,8	10,48
4	$\Delta_{min} i$	Vh	-0,5	-0,46	-10,48	-10,48	-0,28	-10,48	-10,48	-10,48	-0,68	-0,08	-54,4	-5,44
5	Δ_{min}	Vh												-5,44
6	ε_{min}	%	-4,77	-4,39	-100,00	-100,00	-2,67	-100,00	-100,00	-100,00	-6,49	-0,76	-51,91	-51,91
7	$Q_{tr} Mi$	Vh	23,6	21,8	16,2	16,1	18,1	16,4	15,2	16,1	18,5	16,5	178,5	17,85
8	$Q_{tr} R$	Vh	23,79	23,79	23,79	23,79	23,79	23,79	23,79	23,79	23,79	23,79	237,9	23,79
9	$\Delta_{tr} i$	Vh	-0,19	-1,99	-7,59	-7,69	-5,69	-7,39	-8,59	-7,69	-5,29	-7,29	-59,4	-5,94
10	Δ_{tr}	Vh												-5,94
10	ε_{tr}	%	-0,8	-8,4	-31,9	-32,3	-23,9	-31,1	-36,1	-32,3	-22,2	-30,6	-25,0	-24,97
11	$Q_n Mi$	Vh	1360	1380	1288	1340	1401	1288	1396	1361	1344	1410	13568	1356,8
12	$Q_n R$	Vh	1442	1442	1442	1442	1442	1442	1442	1442	1442	1442	14420	1442
13	$\Delta_n i$	Vh	-82	-62	-154	-102	-41	-154	-46	-81	-98	-32	-852	-85,2
14	Δ_n	Vh												-85,2
15	ε_n	%	-5,69	-4,30	-10,68	-7,07	-2,84	-10,68	-3,19	-5,62	-6,80	-2,22	-5,91	-5,91

7,6 mc/luna

ANEXE A2

Anexa 2
TABEL A2

serii contoare	parametri	UM	1120	1121	1122	1123	1124	1125	1126	1127	1128	1129	TOTAL	media
Q mediu lunar	mcluna		12,5	11,8	14,5	12,2	11,5	12,4	14,6	12	10,8	9,6	121,9	12,19
Q_{min} 20% Q mediu lunar	mcluna		2,5	2,36	2,9	2,44	2,3	2,48	2,92	2,4	2,16	1,92	24,38	2,438
Q_r 50% Q mediu lunar	mcluna		6,25	5,9	7,25	6,1	5,75	6,2	7,3	6	5,4	4,8	60,95	6,095
Q_n 30% Q mediu lunar	mcluna		3,75	3,54	4,35	3,66	3,45	3,72	4,38	3,6	3,24	2,88	36,57	3,66
ε_{min}	%		-4,77	-4,39	-100,00	-100,00	-2,67	-100,00	-100,00	-100,00	-6,49	-0,76	-51,91	-5,19
ε_{tr}	%		-0,80	-8,36	-31,90	-32,32	-23,92	-31,06	-36,11	-32,32	-22,24	-30,64	-24,97	-2,50
ε_n	%		-5,69	-4,30	-10,68	-7,07	-2,84	-10,68	-3,19	-5,62	-6,80	-2,22	-5,91	-0,59
$Q_{min} NI$	mcluna		-0,1193	-0,1036	-2,9	-2,44	-0,06145	-2,48	-2,92	-2,4	-0,14	-0,015	-12,66	-1,27
$Q_{tr} NI$	mcluna		-0,0499	-0,4935	-2,313	-1,9718	-1,37526	-1,9259	-2,6359	-1,9395	-1,2	-1,471	-15,22	-1,52
$Q_n NI$	mcluna		-0,2132	-0,1522	-0,465	-0,2589	-0,09809	-0,3973	-0,1997	-0,2022	-0,22	-0,064	-2,161	-0,22
Q mediu lunar NI	mcluna		-0,38	-0,75	-5,68	-4,67	-1,53	-4,80	-5,70	-4,54	-1,56	-1,55	-30,03	-3,00